

OPTICAL SPECTROSCOPIC STUDIES OF SQUARE PLANAR  $d^8$  DIMERS

Thesis by  
Steven Frederick Rice

In Partial Fulfillment of the Requirements  
for the Degree of  
Doctor of Philosophy

California Institute of Technology  
Pasadena, California

1982

(Submitted February 3, 1982)

## ACKNOWLEDGEMENTS

I would like to thank all those who have helped me accomplish the goal of obtaining my Ph.D.

My mentors at M.I.T. during my undergraduate study have continued to aid me greatly while at Caltech. I thank Dr. Randall Wilson and Dr. Robert Gay for teaching me many of my scientific skills. I am especially pleased with this opportunity to thank Professor Edward Solomon for my initial research experience and for showing me where to find the "trip".

At Caltech many people have aided my research efforts. I appreciate the help from members of the Gray Group: Terry Smith, Jay Winkler, and Dr. Vince Miskowski for many useful discussions, Dr. Steven Milder and the "Santa Cruz Connection" for some of the experimental results in Chapter 3, and C.M. Che for some of the samples used in Chapter 4. Other members of the Chemistry Department have helped me in various ways. Bill Lambert and Dave Millar have contributed to my education in instrument design. The entire staff of the department, particularly Charlie Beebe with 5,000 cups of coffee, has always been most helpful. In addition, this thesis was made physically possible by the outstanding typing skills of Mary Arguijo, and the illustrations drawn by Valerie Purvis. Professor Harry Gray has been very supportive and I thank him for his active interest and wise contributions toward my scientific training. I would also like to thank the

Fannie and John Hertz Foundation for the generous financial support I received during my graduate education.

Finally, I wish to express thankfulness for my loved ones: my parents, Roy and Sue, my brother and sisters, Peter, Elizabeth, and Laura, and my wonderful wife, Leslie. Their encouragement has aided me untold times in the accomplishment of this research.

To my wife, Leslie

## ABSTRACT

The single crystal polarized absorption spectra of rhodium(I) diisocyanide dimers presented confirm the assignment of Mann and Gray for the intense visible absorption band as  ${}^1A_{1g} \rightarrow {}^1A_{2u}$ . The structured  ${}^1A_{1g} \rightarrow {}^3A_{2u}$  absorption band in  $Rh_2(b)_4(Bph_4)_2$  shows the  ${}^3A_{2u}$  excited state to have a metal-metal vibrational frequency of  $149\text{ cm}^{-1}$ . This is compared to the  $85\text{ cm}^{-1}$  ground state frequency which results in the orbital assignment of this transition as  $d_{z^2}\sigma^* \rightarrow p_z\sigma$ . The excited state has an internuclear bond distance  $.31\text{ \AA}$  shorter than that of the ground state. The bonding description obtained through the analysis of the spectra depicts a ground state that is formally nonbonding stabilized through configurational interaction with a low lying, strongly bonded excited state.

The  ${}^3A_{2u}$  state in these dimers has a pronounced phosphorescence with a 77K lifetime of  $20\text{ }\mu\text{sec}$ . The quantum yields and lifetimes are very temperature sensitive with several 300K lifetimes of about  $10\text{ nsec}$ . This temperature dependence, characteristic of a strong coupling limit, is interpreted in terms of a nonradiative pathway depopulating the  ${}^3A_{2u}$  through another excited state associated with a  $d_{z^2} \rightarrow d_{x^2-y^2}$  transition.

A compound isoelectronic with these rhodium diisocyanides,  $\text{Pt}_2(\text{H}_2\text{P}_2\text{O}_5)_4^{4-}$ , is shown to have a similar metal-metal interaction in both the ground and lowest excited states. Recent results regarding the low temperature photophysics of this compound have been verified and extended through an analysis of the vibronically structured  ${}^3\text{A}_{2u} \rightarrow {}^1\text{A}_{1g}$  luminescence. The  ${}^3\text{A}_{2u}$  excited state is demonstrated to have an internuclear distance of  $2.71 \text{ \AA}$ ,  $.21 \text{ \AA}$  shorter than that of the ground state. The metal-metal vibrational frequency in the  ${}^3\text{A}_{2u}$  is  $155 \text{ cm}^{-1}$ , distinctly higher than the  $110 \text{ cm}^{-1}$  of the ground state.

## TABLE OF CONTENTS

	<u>Page</u>
<u>Chapter 1 - Introduction</u>	
Section 1 - Introduction to Optical Techniques and Bonding Analysis . . . . .	2
Section 2 - Introduction to $d^8$ Monomer and Dimer Spectra . . . . .	6
<u>Chapter 2 - Absorption Spectroscopy and Bonding of Rhodium(I) Diisocyanides</u>	
Section 1 - Introduction and Experimental . . . . .	25
Section 2 - Results and Assignments of the Polarized Absorption Spectra of $Rh_2(TMB)_4^{3+}$ and $Rh_2(b)_4^{2+}$ . . . . .	29
Section 3 - Assignment of the Absorption Spectra of $Rh_2(DMB)_4^{2+}$ . . . . .	59
Section 4 - The Theory and Experimental Appli- cations of the Analysis of a Structured Optical Transition . . . . .	63
Section 5 - Results of the $^1A_{1g} \rightarrow ^3A_{2u}$ Structured Absorption Band in $Rh_2(b)_4(Bph_4)_2$ . . . . .	72
Section 6 - Analysis of the Details of the Bonding in $Rh_2(b)_4^{2+}$ . . . . .	82
Section 7 - Conclusions . . . . .	100
<u>Chapter 3 - Luminescence and Photophysics of Rhodium(I) Diisocyanides</u>	
Section 1 - Introduction and Results of the $^3A_{2u}$ Lifetime . . . . .	105

	<u>Page</u>
Section 2 - Analysis of the Strong Coupling Limit in Nonradiative Transitions . . . . .	113
Section 3 - Discussion of the $^3A_{2u}$ Nonradiative Decay Rates . . . . .	124
Section 4 - Results and Discussion of the Excitation Spectra for $^1A_{2u} \rightarrow ^1A_{1g}$ and $^3A_{2u} \rightarrow ^1A_{1g}$ . . . . .	132
Section 5 - Conclusions . . . . .	135
<u>Chapter 4</u> - Optical Spectra of $Pt_2(H_2P_2O_5)_4^{4-}$	
Section 1 - Introduction . . . . .	142
Section 2 - Experimental and Sample Characteristics	145
Section 3 - Absorption and Emission Spectra of $K_4Pt_2(H_2P_2O_5)_4$ and $Ba_2Pt_2(H_2P_2O_5)_4$ . .	148
Section 4 - Conclusions . . . . .	188
References . . . . .	194
Appendix . . . . .	200

CHAPTER 1

Introduction

## SECTION 1

Optical spectroscopy has been used for years to solve hundreds of problems regarding molecular electronic structure.<sup>1</sup> Often subtle questions of bonding in molecular systems can best be solved through spectroscopic studies of electronic excited states. With the development of numerous pulsed laser techniques significantly augmenting conventional flash photolysis,<sup>2</sup> many aspects of radiationless transitions have come under close experimental scrutiny. In the field of transition metal inorganic chemistry, optical spectroscopy combined with theoretical advances led to the development of Ligand Field Theory,<sup>3</sup> a bonding model capable of explaining not only the spectroscopic properties of a large class of coordination complexes, but also a great deal of the ligand substitution and electron transfer chemistry observed in these compounds.<sup>4</sup>

Inorganic spectroscopy has now turned its attention toward more difficult bonding problems involving multinuclear compounds with metal-metal interactions. A variety of spectroscopic techniques have been used to analyze the bonding interaction in multinuclear metal clusters. In many cases the complex electronic structures associated with polynuclear clusters, dimers in particular, have been shown to be interpretable in terms of molecular orbitals.<sup>5</sup> Specifically, the monomer moieties of a dimer or cluster can be treated in a ligand field context and then through an analysis of

the spectral changes associated with oligomerization, the salient features attributable to the metal-metal interactions can be extracted. Orbital overlap, valence electron count, and ligand characteristics all play an important role in determining net internuclear bonding characteristics. The development of an orbital description that displays the energy of the metal one electron orbitals as a function of internuclear distance can give a remarkably detailed explanation for the origins and composition of a metal-metal bond.

Unfortunately, obtaining data that allow for such a complete description is virtually impossible. This is in part due to the inherent approximations present in the use of one electron orbitals because even in situations where a one electron picture is likely to be appropriate, the experimenter is forced to measure energies of electronic states, not orbitals. This limitation is combined with the usual inability to measure and assign a sufficiently large number of states to extract relative energies of all the orbitals. If this were possible, a complete description of a metal metal interaction would still remain elusive because simple optical absorption and emission spectroscopy can only report state energies near the equilibrium geometry of the ground and excited states.

In spite of the difficulties that are so apparent, in favorable cases spectroscopic data can enable the

experimenter to determine the potential surface of a particular state as a function of metal-metal coordinate over a small region. This can be done by an analysis of the shape of an absorption or emission spectrum that exhibits vibrational fine structure in the vibrational frequency characteristic of the internuclear bond.<sup>6</sup> An accurate restricted potential surface does not necessarily yield all the information desired regarding a complete molecular orbital description of bonding, but it does contain the information required to extract reasonable values for relative electronic state geometries and, in favorable cases, bond energies. Frequently an experimentally determined excited state potential surface can be used to aid a spectroscopist in ascertaining the molecular orbitals involved in an electronic transition. By doing so, a potential surface yields valuable information needed to qualify the relative contribution of a particular molecular orbital to a bonding scheme.

Ground state bonding is not the only facet of chemical physics which can be probed by optical spectroscopy. An accurate description of any photochemical process requires an understanding of the excited state characteristics of the photoactive molecule.<sup>7</sup> Although most molecular systems absorb light in the optical region of the spectrum, few participate in photochemical reactions. This is largely due to intramolecular nonradiative processes which serve to

deactivate the system by emptying the localized electronic excited state energy into a surrounding heat bath before it can be used in a more specific way as in a photochemical reaction. An immense amount of theoretical work has gone into developing a quantum mechanical description for a variety of these nonradiative processes.<sup>8</sup> Many of the predictions of the current theory have been borne out in experiments on organic molecules.<sup>9</sup> Inorganic tests to this theory are few and have not begun to address much of the photophysical behavior peculiar to transition metal compounds. Unlike most organic systems, inorganic complexes may have low lying excited states possessing equilibrium geometries greatly distorted from that of the ground state. The consequences of such distortions with intramolecular nonradiative transitions and photochemical reactivity are not well known. Optical probes coupled with appropriate chemical perturbations can illuminate the significance of excited state distortions regarding inorganic photochemical reactivity.

Primarily through the use of optical spectroscopy, this thesis will address the points raised above in a particular inorganic system: square planar  $d^8$  dimers. There has been an extensive amount of research focused on the thermal chemistry, bonding, and optical spectra of monomeric  $d^8$  transition metal compounds. The existence of oligomeric solution species of these monomers has been suspected for quite some time,<sup>10</sup> but only recently have

discrete dimers with bridging ligands been synthesized.<sup>11</sup> These dimers and oligomers have been shown to have rich photochemistry, unique solid state properties, and dramatically different spectroscopic characteristics not present in their parent monomers.

The origins of this tendency to oligomerize will be addressed in detail for this general class of molecules. A fairly complete bonding description for these dimers will be presented for the ground state and several low lying excited states. An analysis of the radiative and nonradiative processes determining the lifetimes of the lowest excited states will be presented. The pronounced temperature dependence of the intramolecular nonradiative decay will be examined in terms of a current theoretical description generating a direct relationship between excited state geometry, bonding, photochemical reactivity, and photophysical intramolecular transition rates.

## Section 2

The chemistry of  $d^8$  transition metal complexes has been extensively developed over the years. In fact, Zeise made the first "organometallic" compounds with platinum(II) in about 1830. More recently, Vaska and DiLuzio<sup>13</sup> synthesized an organometallic iridium(I) species exhibiting extensive oxidative addition chemistry. Catalytic cycles

involving rhodium(I) square planar intermediates have been shown to have true industrial applicability.<sup>12,14</sup> Zeise's salt,  $\text{KPt}(\text{C}_2\text{H}_4)\text{Cl}_3$ , and Vaska's compound,  $\text{trans IrCl}(\text{CO})-(\text{PPh}_3)_2$ , are known to exhibit modest luminescence.<sup>15</sup> The presence of luminescence in inorganic or organometallic complexes is a somewhat rare occurrence. Recently, inorganic photochemists have begun to exploit the long excited state lifetimes frequently associated with luminescence to facilitate bimolecular photochemical oxidations and reductions. Square planar  $d^8$  complexes offer a particularly inviting photochemical arena combining long lived excited states with facile redox chemistry involving changes in geometry and coordination number.

Some of the more common ligands used on these  $d^8$  second and third row elements are phosphines, isocyanides, and carbon monoxide. The photophysical properties of square planar rhodium and iridium phosphines have been studied in some detail;<sup>16</sup> the other complexes are not well documented in this respect. However, the optical absorption spectra of a variety of metal and ligand combinations have been studied thoroughly and related to the well understood electronic structure of  $\text{Pt}(\text{CN})_4^{2-}$ .

The photochemistry of these compounds is limited for two major reasons. The observed excited state lifetimes, although very long in the solid state and in rigid glasses, are very short in fluid solution at room temperature.<sup>17</sup>

This restricts the possibilities for bimolecular reactivity. The second flaw is that the square planar geometry leaves the excited molecule wide open to oxidation and solvolysis to an octahedral  $d^6$  complex. Because the solvent molecules stabilize the oxidized form, the possibility of a catalytic cycle becomes undermined.

Many years ago it was noticed that concentrated solutions and some crystals of  $\text{Rh}(\text{CNR})_4^+$  ions were highly colored.<sup>10</sup> Dilute solutions are always yellow, as are most crystals containing these complexes. Gray *et al.*<sup>18</sup> began to investigate this intense coloration, realizing the advantages of appreciable absorbance in the visible region with regard to potentially useful photochemical reactions. They showed through several methods, including X-ray crystallography,<sup>19</sup> that the intense absorption in the visible region in these transition metal isocyanides was due to dimerization of the two  $d^8$  centers. In solution, however, the concentration of metal ions had to be rather high in order to get appreciable dimerization, hampered by equilibrium constants favoring the interaction of only about  $10^1$ - $10^2$  for various isocyanide ligands.<sup>19</sup>

Aside from their potential photochemistry,  $d^8$  systems such as  $\text{Pt}(\text{CN})_4^{2-}$  are known to stack into linear chains when accompanied by certain cations.<sup>20</sup> These materials exhibit interesting electrical conductivity properties reflecting their one dimensional structure. Interrante<sup>21</sup>

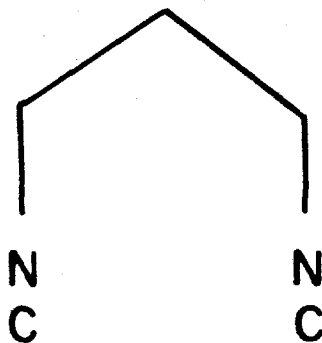
has shown through the use of an X $\alpha$ -SCF calculation that the interaction between two d<sup>8</sup> centers can be viewed as the building block of these extended chains. The general spectroscopic effects observed in the solution oligomerization support the conclusions of Interrante.

By synthesizing a bridging diisocyanide, the two rhodium(I) centers could be locked into this dimeric interaction enabling the preparation of a pure solution of only dimers, facilitating spectroscopic studies. Several ligands were prepared from commercially available diamines:<sup>22,23</sup> 1,3 diisocyanopropane,<sup>11</sup> 2,5 dimethyl diisocyanohexane, and 1,8 diisocyanomenthane. They have been given the trivial names "bridge", "tetramethyl four bridge", and "dimethyl bridge", abbreviated as b, TMB, and DMB, respectively. Figure 1a shows the structure of these ligands. All three bridges react with Rh<sub>2</sub>(COD)<sub>2</sub>Cl<sub>2</sub> to produce the ions Rh<sub>2</sub>(b)<sub>4</sub><sup>2+</sup>, Rh<sub>2</sub>(TMB)<sub>4</sub><sup>2+</sup>, and Rh<sub>2</sub>(DMB)<sub>4</sub><sup>2+</sup>. X-ray crystal structures have been obtained on the salts Rh<sub>2</sub>(b)<sub>4</sub>(Bph<sub>4</sub>)<sub>2</sub>,<sup>24</sup> Rh<sub>2</sub>(TMB)<sub>4</sub>(PF<sub>6</sub>)<sub>2</sub>,<sup>24</sup> and Rh(DMB)<sub>4</sub>(PF<sub>6</sub>)<sub>2</sub>.<sup>25</sup> The ORTEPS of the first two of these dimeric d<sup>8</sup> ions are shown in Figure 1b.

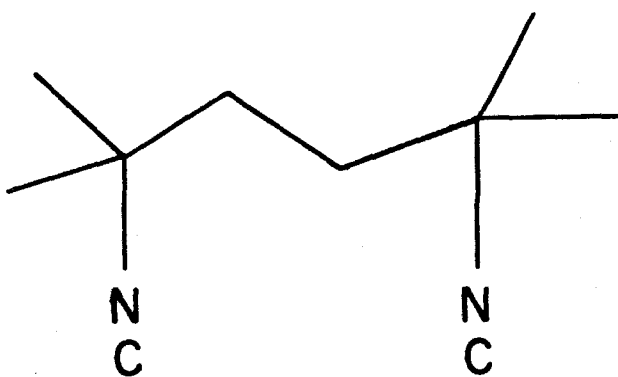
Rh<sub>2</sub>(b)<sub>4</sub><sup>2+</sup> and Rh<sub>2</sub>(TMB)<sub>4</sub><sup>2+</sup> have metal-metal distances of 3.24 Å and 3.26 Å, respectively. Rh<sub>2</sub>(DMB)<sub>4</sub><sup>2+</sup> has a metal-metal distance of 4.47 Å placing it in a somewhat different class than the former ions. The ligand configuration in all three cases is that of two square planar

Figure 1. a) Structures of three bridging diisocyanides, 1,3 diisocyanopropane (bridge), 2,5 dimethyl diisocyanohexane (TMB), and 1,8 diisocyanomethane (DMB). b) ORTEPS of  $\text{Rh}_2(\text{TMB})_4^{2+}$  and  $\text{Rh}_2(\text{b})_4^{2+}$ .

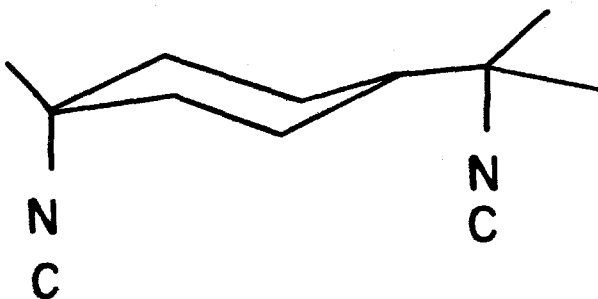
BRIDGE



TMB

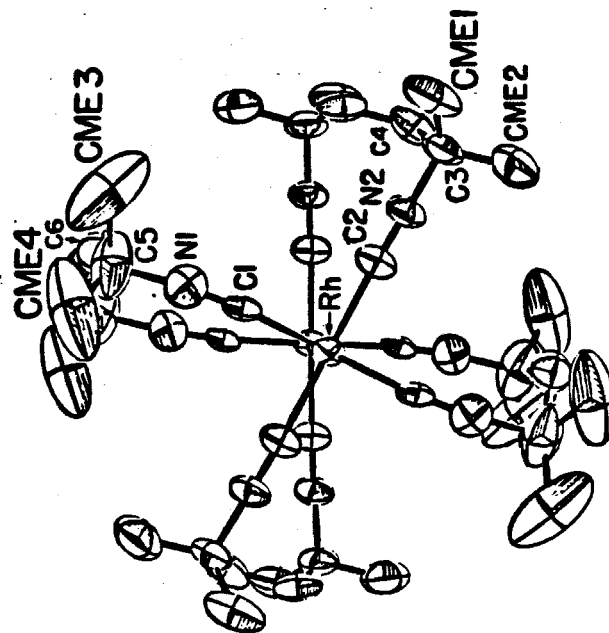


DMB

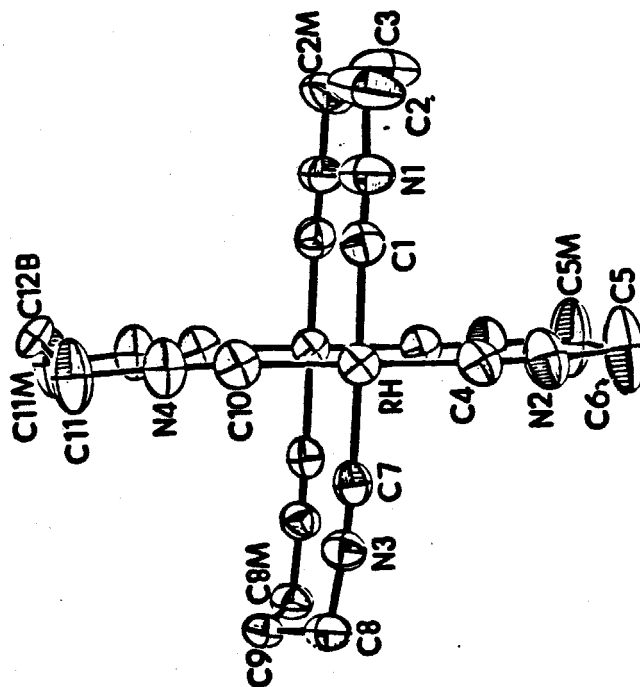




3.26 Å



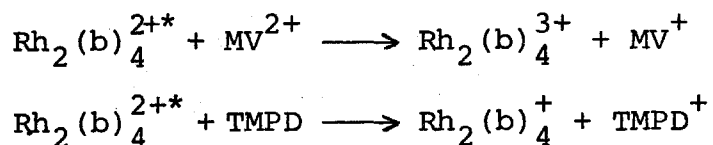
3.24 Å



rhodium(I) ions placed face to face. The relative orientation of the isocyanides are eclipsed in the case of  $\text{Rh}_2(\text{b})_4^{2+}$  and staggered to some extent in  $\text{Rh}_2(\text{TMB})_4^{2+}$  and the dimer of  $\text{Rh}(\text{CNph})_4^+$ ,  $[\text{Rh}(\text{CNph})_4]_2^{2+}$ .<sup>19</sup> The ability of TMB and the free monomers to allow a twisting with respect to the two planes reflects the rigidity of the ligand. TMB, because of its additional tetrahedral carbon linkage in the bridgehead, is presumably a much more adaptable ligand than bridge with respect to the relative geometries of the two metal ions. This rigidity or lack of it between bridge and the other larger bridging ligands plays an important role in the excited state lifetimes observed in this series.

In 1978, it was discovered that  $\text{Rh}_2(\text{b})_4^{2+}$  exhibited a reasonably intense luminescence with a lifetime less than 2 nsec.<sup>26</sup> It has been assigned as fluorescence from the lowest spin allowed excited state. Through flash photolysis it was determined that there was also a long lived transient associated with this molecule having a lifetime of 8.3  $\mu\text{sec}$  in fluid solution. It was postulated that this transient was due to population of the lowest energy spin forbidden excited state produced through intramolecular nonradiative decay of the lowest spin allowed state. This is a remarkably long fluid solution lifetime for a rhodium(I)  $\pi$  acceptor complex. Unlike the 2 nsec singlet state, it is sufficiently long to permit

bimolecular excited state reactions. S. Milder subsequently showed that this excited state is both a powerful oxidant and reductant capable of undergoing the reactions



where TMPD is tetramethylphenylenediamine and  $\text{MV}^{2+}$  is the methylviologen dication.<sup>27</sup>

The properties of  $\text{Rh}_2(\text{b})_4^{2+}$  are quite different from those of the monomers. The intense visible absorption and long lived excited state have suggested excellent possibilities for photocatalysis. Recent investigations indicate certain iridium dimers similar to  $\text{Rh}_2(\text{b})_4^{2+}$  have even more promise.

Mann and Gray have determined qualitatively the spectroscopic effects of dimerization on the  $d^8$  metal center, accounting for the intense visible absorption present in the dimers and absent in the monomers. The major goal of this research is to verify not only the abbreviated description of Mann and Gray, but to determine all the consequences of dimerization on the electronic structure of  $d^8$  square planar complexes. The assignment of the various excited states in these dimers will be discussed at length. These assignments can be used to develop a molecular orbital picture with sufficient versatility to account for all the

spectral and photophysical properties exhibited by this general class of  $d^8$  dimers. This general electronic structure can be extended to explain other higher oligomers and infinite chain systems.

The details of the electronic structure obtained from various spectral measurements can be used to predict excited state geometries. The value of knowing the magnitude and direction of the excited state distortions should not be underestimated. The relative geometries of the various states in a molecule not only represent the differences in bonding between these states, but also have fundamental implications regarding the intramolecular nonradiative pathways which frequently determine the lifetime of a given state.

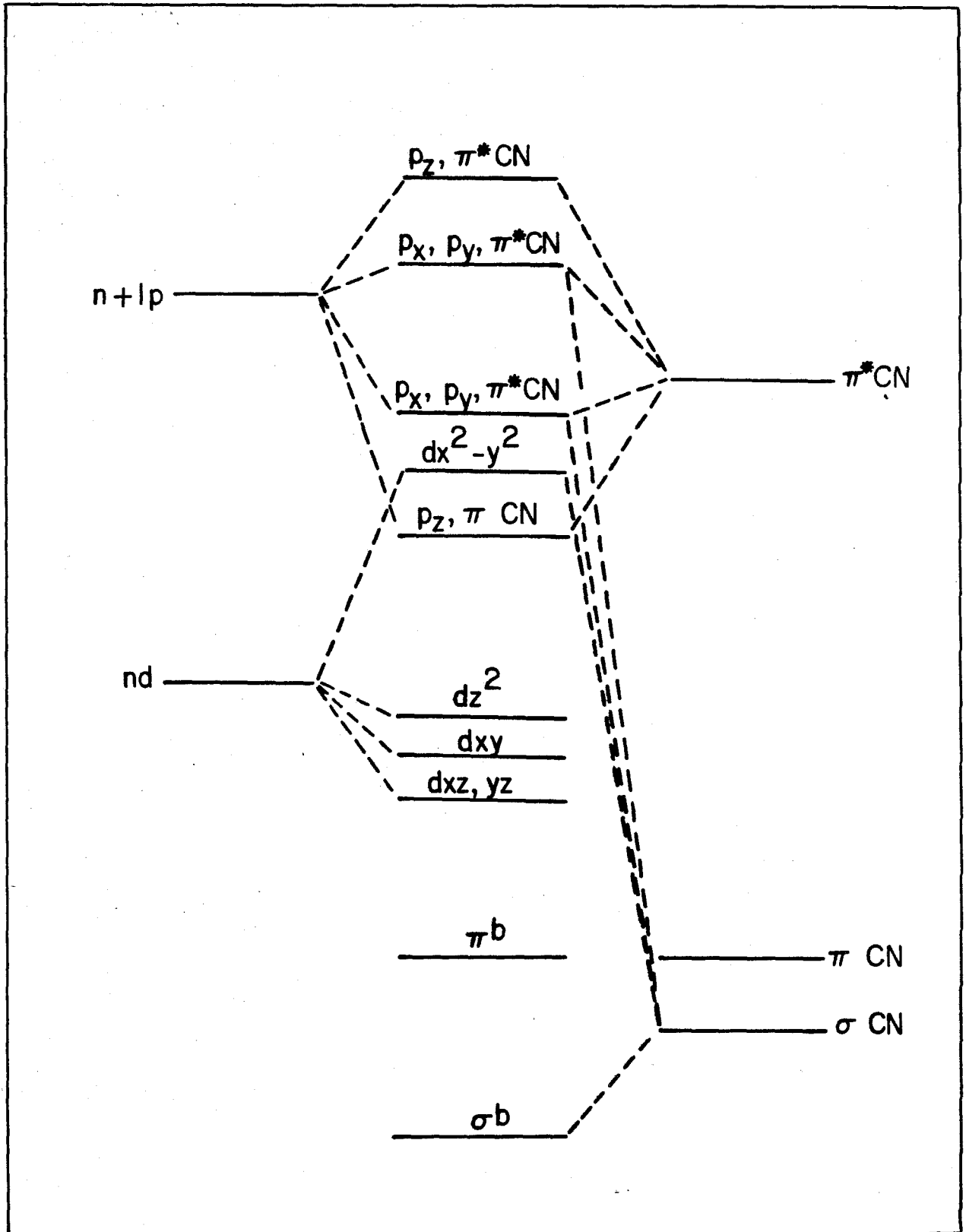
In order to begin to discuss the electronic structure of these dimers, a clear understanding of monomeric spectra and structure is needed. A brief description of the current understanding of the optical spectra of square planar  $d^8$  transition metal complexes with  $\pi$  acceptor ligands is presented here.

In 1963 Gray and Ballhausen published a paper describing the electronic structure of a variety of  $d^8$  cyanides and halides based on the solution absorption spectra of these ions.<sup>28</sup> This paper was the result of a number of papers written in the late 1950's and early 1960's

assigning absorption bands in specific systems. Gray and Ballhausen concluded that the intense absorption bands ( $\epsilon \sim 10^4$ ) in the near U.V. region in  $\text{Ni}(\text{CN})_4^{2-}$ ,  $\text{Pd}(\text{CN})_4^{2-}$ , and  $\text{Pt}(\text{CN})_4^{2-}$  are metal to ligand charge transfer transitions. The molecular orbital diagram used to describe these bands is shown in Figure 2. The most important feature of this diagram is the placement of the  $a_{2u}(\pi^*\text{CN})$  orbital at lower energy than the  $e_u(\pi^*\text{CN})$  orbital. This  $a_{2u}$  stabilization is a consequence of the square planar geometry. The  $a_{2u}$  can interact with the unoccupied  $p_z$  metal orbital stabilizing the charge transfer. The  $e_u$  orbital does not interact with  $p_x$  and  $p_y$  as much because these metal orbitals have significant  $\sigma$  antibonding interaction with the  $\text{CN}^-$  ligands. This  $\sigma^*$  interaction raises the energy of  $p_x$  and  $p_y$  reducing their ability to mix with  $e_u(\pi^*\text{CN})$ . The selective energy stabilization of the  $a_{2u}$  charge transfer orbital results in the location of the MLCT bands at unusually low energy.

The energy ordering of the d set in  $\text{Pt}(\text{CN})_4^{2-}$  and  $\text{Ni}(\text{CN})_4^{2-}$  was determined by Cowman and Gray in 1973.<sup>29</sup> They were fortunate enough to obtain the polarizations of the charge transfer bands which determined the d orbital ordering in Figure 2. In the  $\text{Pt}(\text{CN})_4^{2-}$  spectrum, the lowest lying spin allowed band at 263 nm is assigned as  ${}^1A_{1g} \rightarrow {}^1A_{2u}$  ( $5d_{z^2} \rightarrow 6p_z, \pi^*\text{CN}$ ). The next allowed band is assigned as  ${}^1A_{1g} \rightarrow {}^1E_u$  ( $5d_{xz,yz} \rightarrow 6p_z, \pi^*\text{CN}$ ). There are

Figure 2. The molecular orbital diagram of a  $d^8$  square planar metal complexed with cyanide ligands.



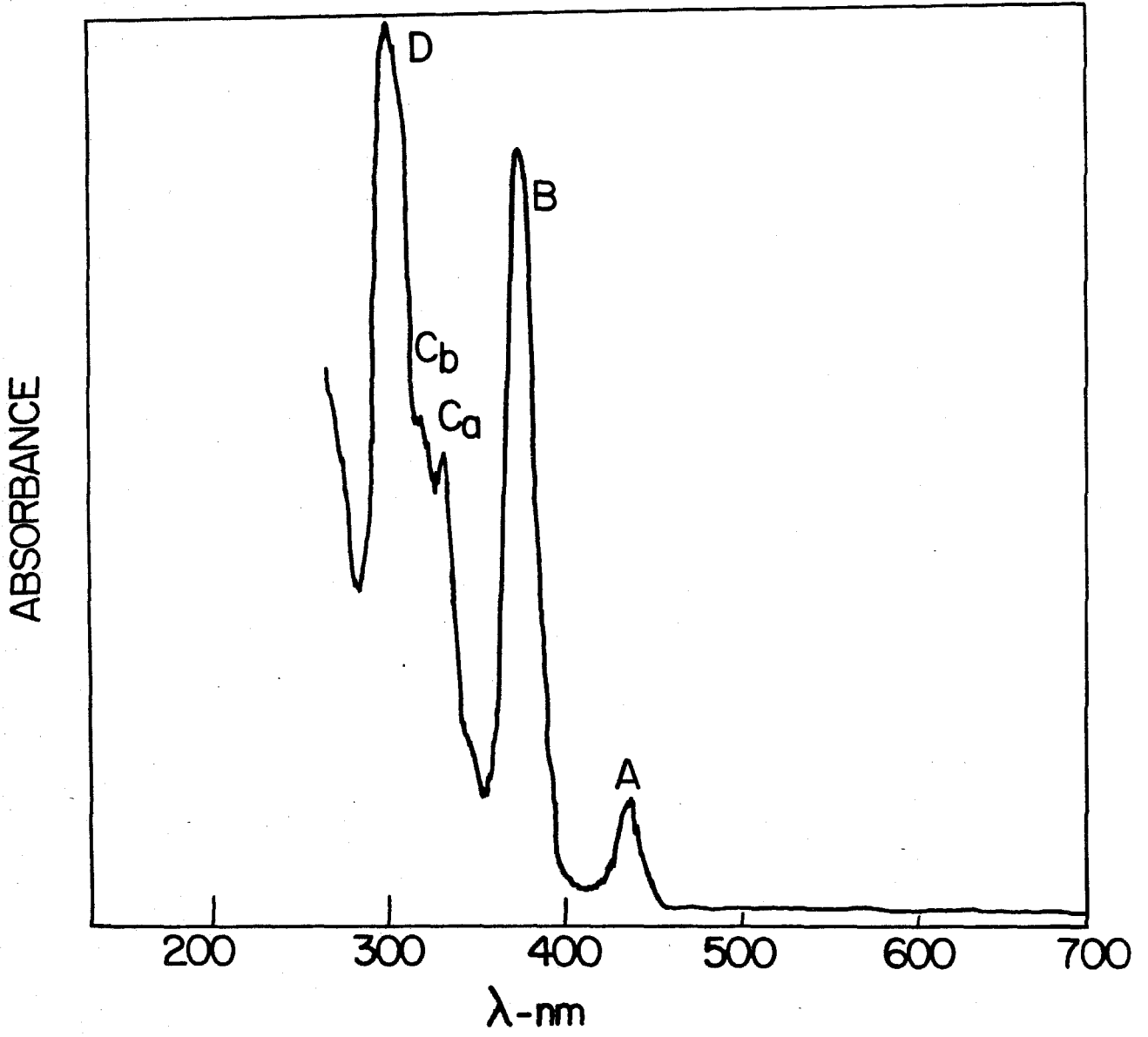
other weak features placed in this region, some correspond to d-d metal localized transitions (in  $\text{Ni}(\text{CN})_4^{2-}$  transitions to  $d_{x^2-y^2}$ ) and others are orbitally or spin forbidden charge transfer bands. However, the splitting of the  $d_{z^2}$  and  $d_{xz,yz}$  is clearly the dominant spectroscopic feature.

In 1975 Isci and Mason assigned the spectra of rhodium and iridium aliphatic isocyanides.<sup>30</sup> Solution absorption and MCD spectra combined with the conclusions of Cowman and Gray gave assignments drawing direct analogies to  $\text{Pt}(\text{CN})_4^{2-}$ . Geoffroy<sup>31</sup> has since continued to assign the charge transfer spectra of dozens of  $d^8$   $\pi$  acceptor complexes in analogy to the work of Gray, Ballhausen, and Mason.

The spectrum of a solution of  $\text{Rh}(\text{t-butNC})_4^+$  is shown in Figure 3. The bands A, B, Ca, Cb, and D are assigned as  ${}^1A_{1g} \rightarrow {}^3A_{2u}$  ( $4d_{z^2} \rightarrow 5p_z, \pi^*\text{CNR}$ ),  ${}^1A_{1g} \rightarrow {}^1A_{2u}$  ( $4d_{z^2} \rightarrow 5p_z, \pi^*\text{CNR}$ ),  ${}^1A_{1g} \rightarrow {}^3E_u$  ( $E_u$ ) ( $4d_{xz,yz} \rightarrow 5p_z, \pi^*\text{CNR}$ ),  ${}^1A_{1g} \rightarrow {}^3E_u$  ( $A_{2u}$ ) ( $4d_{xz,yz} \rightarrow 5p_z, \pi^*\text{CNR}$ ),  ${}^1A_{1g} \rightarrow E_u$  ( $4d_{xz,yz} \rightarrow 5p_z, \pi^*\text{CNR}$ ). This is essentially the same spectrum exhibited by all rhodium(I) ions complexed with aliphatic isocyanides. The molecular orbital diagram in Figure 2 is appropriate for these assignments.

Chapter 2 of this thesis will consider the modifications on this molecular orbital diagram resulting from dimerization. The bonding character of some of the excited states in the dimers will be shown to be different from these parent

Figure 3. 15K absorption spectrum of  $\text{Rh}(\text{t-butylNC})_4^+$   
imbedded in polymethylmethacrylate.



monomer states. It will be suggested that some excited states are delocalized throughout the dimer whereas others appear to be localized on a single metal center.

Chapter 3 examines the luminescent properties of these dimers. The results are interpreted in terms of a current theoretical model predicting the observed temperature dependence, accounting for many of the subtle differences between the various dimers. The influence of the ligands will be shown to be a significant factor in the lifetime of the  ${}^3A_{2u}$  excited state in the dimers. The properties of the ligands and the internuclear interaction have a combined relationship determining the important difference between the monomer and dimer excited state photophysical properties.

Chapter 4 presents high resolution absorption and emission spectra of  $d^8$  a dimer,  $Pt_2(H_2P_2O_5)_4^{4-}$ . The spectra obtained on this complex tests many of the generalizations deduced from the rhodium diisocyanide experiments. The vibronic structure observed in this complex, particularly in the  ${}^3A_{2u}$  phosphorescence, presents detailed spectroscopic data supporting work recently done on the low temperature photophysics of the  ${}^3A_{2u}$ .

The conclusions developed by this study help to determine many of the details of  $d^8-d^8$  interactions, a significant characteristic of square planar complexes. They also point out the general applicability of a complete

spectral study on an inorganic system regarding photo-physical, photochemical and bonding characteristics. It shows the wealth of information to be gained regarding photophysical processes not usually observed in organic molecular systems, but nonetheless quite prevalent in high symmetry inorganic complexes. An understanding of these uniquely inorganic characteristics will be very useful in developing and refining potential photoreagents and photocatalysts.

CHAPTER 2Absorption Spectroscopy and Bonding of  
Rhodium(I) Diisocyanides

## Section I

Most of the consequences from the interaction between two square planar  $d^8$  ions can best be described through a molecular orbital scheme. This type of bonding model has worked very well for many other binuclear metal complexes. It will be shown that the majority of the spectral features associated with the  $d^8$  isocyanides can be accounted for through a picture like this augmented with the inclusion of configurational interaction. This chapter will present the experimental evidence required to develop a M.O. diagram with sufficient detail to explain the energies of the various electronic transitions observed throughout the visible and near U.V. spectral regions and also to account for their observed polarizations and band shapes.

Preparations of Materials

Ligands. A method similar to that of Ugi<sup>32</sup> was used to prepare all the diisocyanoalkanes used.

1,3-diisocyanopropane. 22 g of 1,3 diaminopropane (Aldrich), 20 gm of  $CHCl_3$ , 200 ml of 50% NaOH solution, and 200 ml of  $CH_2Cl_2$  as a solvent were reacted together for 2 hours in the presence of a phase transfer catalyst benzyltriethylammonium chloride. The organic phase was separated and dried over  $MgSO_4$ . The orange solution was purified on an Alumina column to yield a clear solution of 1,3 diisocyanopropane.

2,5 dimethyldiisocyanohexane (TMB). This diisocyanide was prepared from 2,5 dimethyldiaminohexane (Aldrich) by a method similar to that used for 1,3 diisocyanopropane. Instead of column purification, because TMB is solid, it was recrystallized from ethanol.

1,8 diisocyanomenthane (DMB). Conditions identical to those used for TMB were employed using the starting material 1,8 diaminomenthane (Aldrich).

### Rhodium Compounds

Rh<sub>2</sub>(1,3 diisocyanopropane)<sub>4</sub>(Bph<sub>4</sub>)<sub>2</sub>. An excess of ligand was added to a CHCl<sub>3</sub> solution of [Rh(COD)Cl]<sub>2</sub>. The dark blue precipitate was isolated and redissolved in methanol. A concentrated methanol solution of Na(Bph<sub>4</sub>) was added to precipitate a purple solid. Large single crystals of Rh<sub>2</sub>(b)<sub>4</sub>(Bph<sub>4</sub>)<sub>2</sub>·CH<sub>3</sub>CN were obtained from slow cooling of a hot saturated CH<sub>3</sub>CN solution of Rh<sub>2</sub>(b)<sub>4</sub>(Bph<sub>4</sub>)<sub>2</sub>.

Rh<sub>2</sub>(TMB)<sub>4</sub>(Bph<sub>4</sub>)<sub>2</sub>. A stoichiometric amount of ligand was added to a toluene solution of Rh<sub>2</sub>(COD)(PF<sub>6</sub>)<sub>2</sub> prepared by metathesis of [Rh(COD)Cl]<sub>2</sub> with Ag PF<sub>6</sub>. The PF<sub>6</sub><sup>-</sup> salt was dissolved in methanol and the Rh<sub>2</sub>(TMB)<sub>4</sub><sup>2+</sup> ion was precipitated with a methanol solution of Na(Bph<sub>4</sub>).

10 mg of  $\text{Rh}_2(\text{TMB})_4(\text{Bph}_4)_2$  was dissolved in 20 ml of  $\text{CH}_3\text{CN}$ . Water was added until the solution clouded, followed by a small amount of  $\text{CH}_3\text{CN}$  to redissolve the  $\text{Rh}_2(\text{TMB})_4(\text{Bph}_4)_2$ . This solution was allowed to stand for several days to evaporate the  $\text{CH}_3\text{CN}$ . Large but thin (2 mm x 2 mm x 30  $\mu\text{m}$ ) single crystals were obtained.

$\text{Rh}_2(\text{DMB})_4(\text{Bph}_4)_2$ . This dimer was prepared in identical fashion to  $\text{Rh}_2(\text{TMB})_4(\text{Bph}_4)_2$ .

$\text{Rh}(\text{CNR})_4^+$ . Salts of these ions were prepared according to Reference 19.

### Instrumentation

Absorption spectra were obtained with a Varian Instrument Cary 17 absorption spectrometer. This instrument was equipped with a Hamamatsu R955 photomultiplier tube to enhance the response in the 650-900 nm region.

Emission spectra were obtained using an instrument constructed in this laboratory. An Oriel Model 6240 arc lamp power supply powers a Hanovia 150W Xe or 200W Hg/Xe arc lamp used as an excitation source. The white light from the arc lamp is wavelength selected with a Spex minimate grating monochromator (f/4.0) and modulated with a Princeton Applied Research Model 125A light chopper. This excitation beam, with resolution up to 1 nm is focused with fused silica lenses onto the sample.

Emitted light is collected and dispersed with a Spex 1870 .5 meter grating monochromator (f/6.9) equipped with 1411SW and 1811SW entrance and exit slits. The dispersed light is detected with a Hamamatsu R955 or R406 photomultiplier tube in a Precision Instruments Model 3377D dry ice-cooled housing. High voltage for the PMT is obtained from a Precision Instruments Model 204 high voltage power supply. The signal is amplified using a PAR Model 186A lock-in amplifier equipped with a PAR 181 current sensitive preamplifier and displayed on a chart recorder.

Luminescence lifetimes were measured using a pulsed laser system constructed in this laboratory. A frequency doubled Quanta Ray Nd:YAG pulsed laser (10 nsec pulse duration) was used to excite the samples. Emission decay was dispersed through a McPherson Model 270 .35 meter monochromator and detected with a Hamamatsu R955 PMT. The signal was converted to voltage using a  $50\Omega$  terminator and recorded photographically with a Tektronix 466 100 MHz storage oscilloscope.

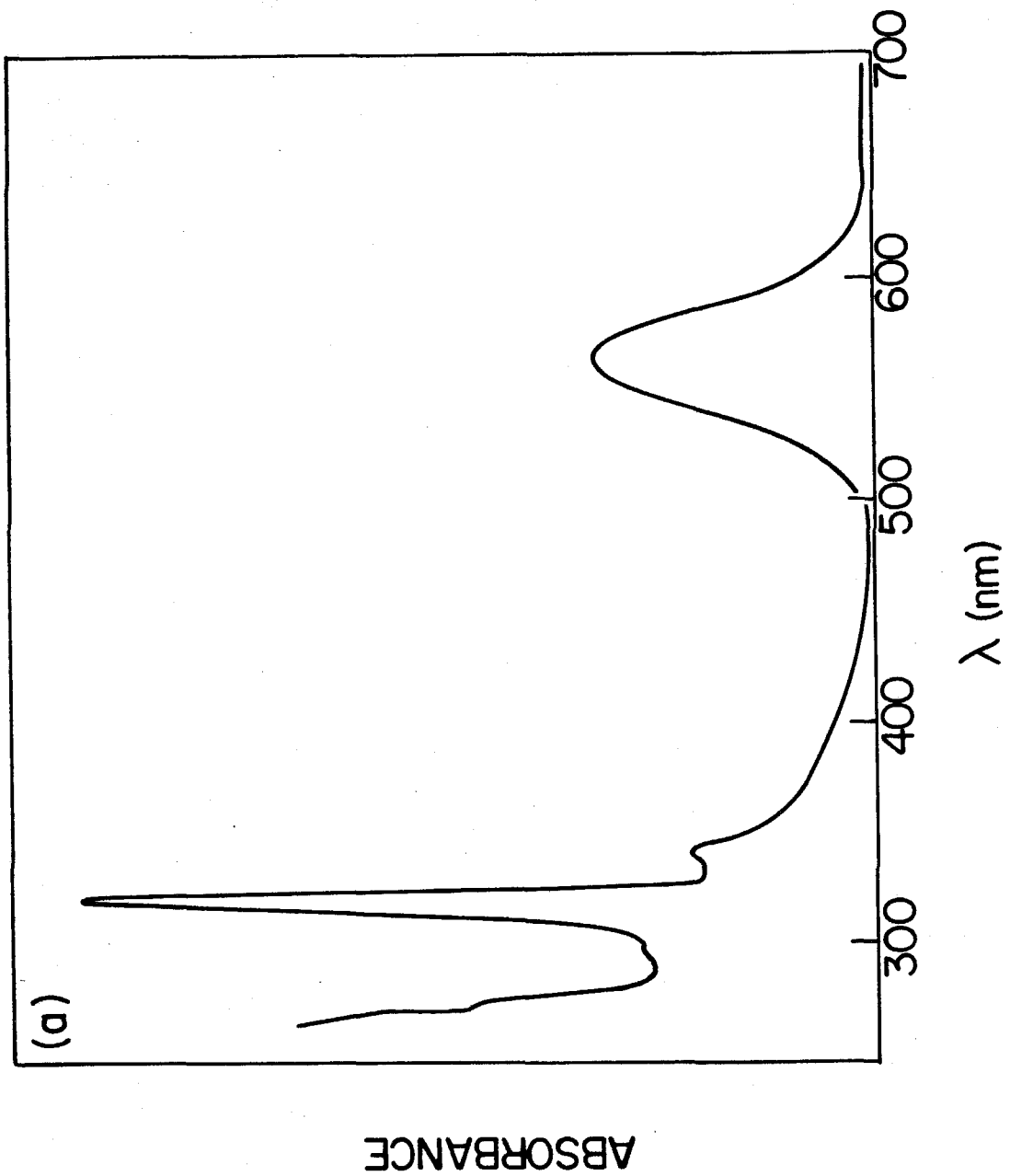
An Andonian O-24 variable temperature liquid helium optical dewar was used to obtain the low temperature data reported. Sample temperature was detected with a calibrated carbon glass resistor imbedded in a brass block placed very near the sample on the sample rod.

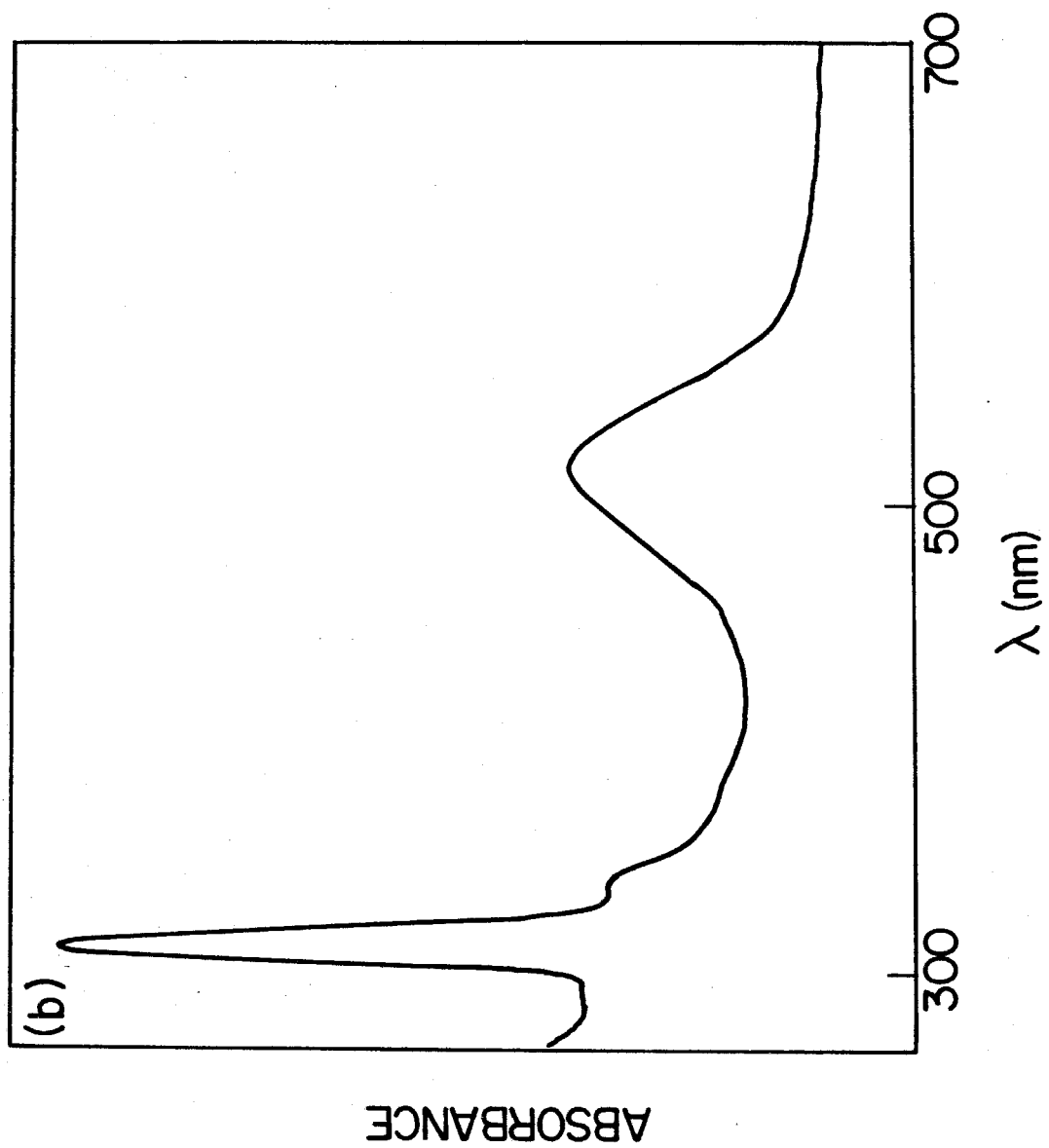
## Section 2

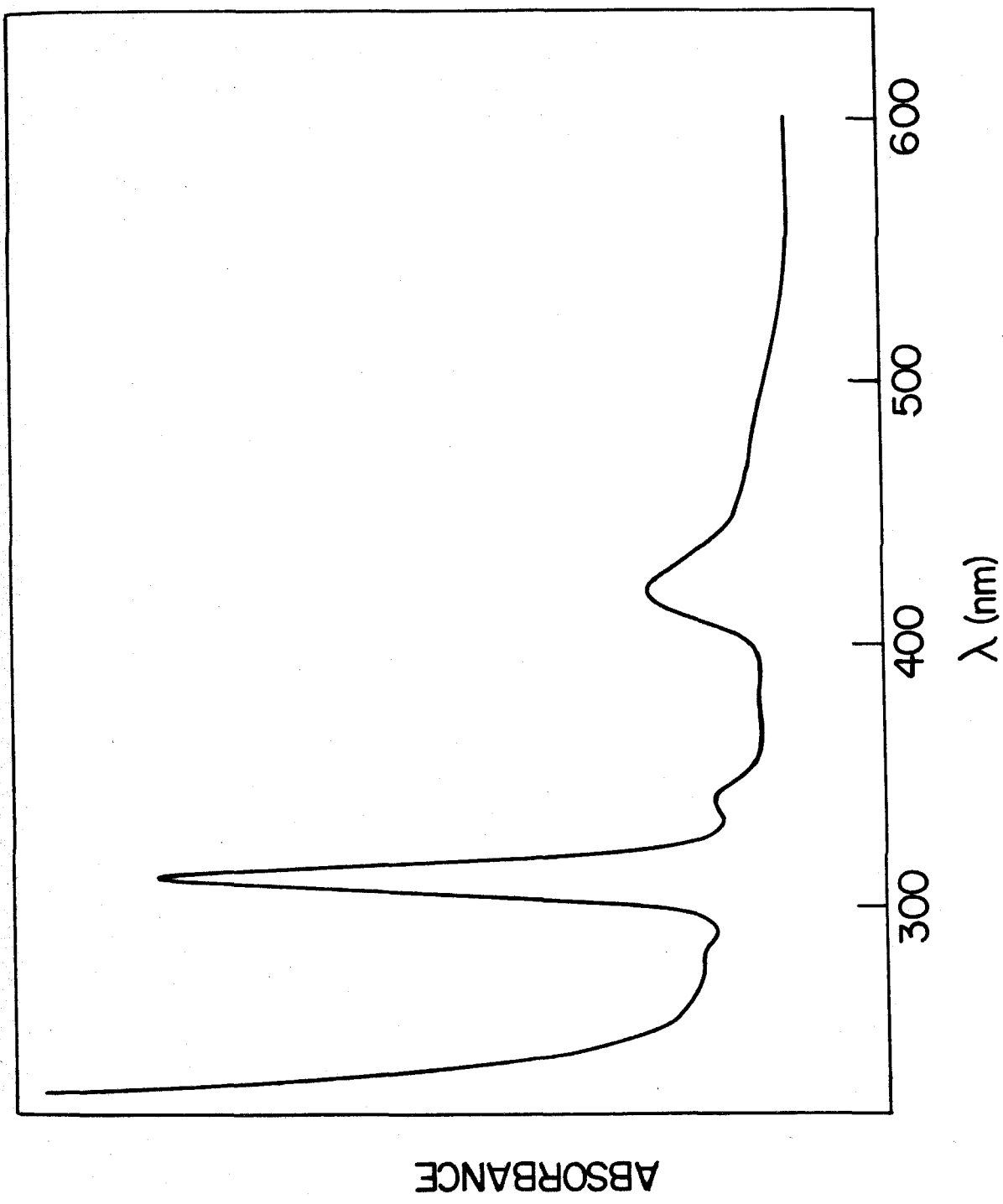
Figure 4 shows the solution absorption spectra of various rhodium(I) isocyanide dimers. The comparison between these spectra and those characteristic of the monomers emphasizes the fact that there are significant changes in the electronic structure of these  $d^8$  ions upon dimerization. The salient features are the following: the appearance of an intense absorption in the 500-600 nm region accompanied by the loss of the absorption of 420 nm, the apparent constancy of the intense feature at 310 nm in both the dimers and the monomers, the loss of a weak feature at 480 nm clearly present in the monomeric spectra. The unique bandshape for the lowest band in  $\text{Rh}_2(\text{DMB})_4^{2+}$  demonstrates an effect of dimerization in spite of the metal-metal distance of 4.47 Å.

The molecular orbital diagram in Figure 5, originally presented by Mann and Gray, accounts for these gross spectral changes. Upon dimerization, the  $d_{z^2}$  and  $p_z, \pi^*\text{CNR}$  orbitals on each individual metal ion interact to form metal-metal bonding and antibonding orbitals. The transition in the monomer,  $d_{z^2}(a_{1g}) \rightarrow \pi^*\text{CNR}(a_{2u})$  is lowered in energy becoming  $d_{z^2}\sigma^*(a_{2u}) \rightarrow p_z, \pi^*\text{CNR} \sigma(a_{1g})$ . The transition assigned as  $d_{xz,yz}(e_g) \rightarrow \pi^*(a_{2u})$  in the monomers will be less shifted due to the insensitivity of the  $d_{xz,yz}$  set ( $\pi$  metal-metal antibonding) to the presence of the other ion at this long distance.

Figure 4. a) Absorption spectrum of  $\text{Rh}_2(\text{b})_4^{2+}$  in a PMMA film at 15K. b) Absorption spectrum of  $\text{Rh}_2(\text{TMB})_4^{2+}$  in 2-methyl THF/acetonitrile at 300K. c) Absorption spectrum of  $\text{Rh}_2(\text{DMB})_4^{2+}$  in 2-methyl THF/acetonitrile in 77K.







This model can be tested through single crystal absorption spectroscopy coupled with a group theoretical analysis of the symmetry of the various states involved in the electronic transitions. Single crystal studies add an additional advantage since polarization effects can allow for the observation of weak transitions obscured in solution. The assignments and energies of the states in the dimer, although in excellent agreement with most of the predictions of the molecular orbital diagram, also serve to raise some questions as to the validity of such a simple description with respect to the finer details of metal-metal bonding.

Selection rules for optical transitions are based on the matrix elements of the electric and magnetic multipole operators with the two electronic states involved in the transitions. The transition probability is a sum of all the multipole (electric dipole, quadrupole, as well as magnetic multipoles) matrix elements of the form  $\langle \phi_{\text{ex}} | \hat{g} | \phi_{\text{gr}} \rangle^2$ . The symmetry of this matrix element must contain a totally symmetric component in order to be non zero. The absolute magnitude of this transition moment cannot be determined by symmetry, but a wealth of experimental evidence has placed order of magnitude values for different multipole operators.

This experimental evidence, as well as theoretical consideration,<sup>33</sup> demonstrates that the largest of these is the electric dipole operator. Other coupling schemes between vibronic wave functions (Herzberg-Teller) can allow for non-zero but significantly smaller electric dipole matrix elements when a symmetry forbidden transition is accompanied by a change in the quantum number of a molecular vibration of appropriate symmetry. Spatial symmetry is not the only selection rule relevant to optical spectra. Spin multiplicity plays an important role as well, with the selection rule being  $\Delta S = 0$  for an allowed transition. Transition element compounds possess relatively large spin orbit coupling creating eigenstates that can be admixtures of states with different spin multiplicity thus relaxing the  $\Delta S = 0$  selection rule. In compounds of high symmetry, however, orbital selection rules are still quite significant, resulting in strong polarizations for nominally  $\Delta S = 0$  transitions and selective mixing of states where  $\Delta S \neq 0$ . This symmetry selective mixing of states with different spin quantum numbers results in spin forbidden transitions possessing polarizations not necessarily representative of the spin allowed  $\Delta S = 0$  "parent" transition.

Group theoretical methods can determine whether a given transition will be allowed or forbidden. Table 1 shows the expected intensities and polarizations for the

TABLE 1

Orbital Transition	Symmetry <sup>a</sup>	Polarization	Expected Singlet $\epsilon$
$d_z 2\sigma^* \rightarrow p_z, \pi^*$	$A_{2u}$	z	$10^4$
$d_z 2\sigma \rightarrow p_z, \pi^*$	$A_{1g}$	Forbidden	$10^3-10^2$
$d_{xy} \rightarrow p_z, \pi^*$	$B_{1u}, B_{2g}$	Forbidden	$10^3-10^2$
$d_{xz, yz} \rightarrow p_z, \pi^*$	$E_u$	x, y	$10^4$
	$E_g$	Forbidden	$10^3-10^2$
$d_z 2\sigma^* \rightarrow d_{x^2-y^2}$	$B_{1g}, B_{2u}$	Forbidden	$10^3-10^2$
$d_z 2\sigma \rightarrow d_{x^2-y^2}$	$B_{2u}, B_{1g}$	Forbidden	$10^3-10^2$
$d_{xy} \rightarrow d_{x^2-y^2}$	2 x $A_{1u}$	Forbidden	$10^3-10^2$
	2 x $A_{2g}$	Forbidden	$10^3$
$d_{xz, yz} \rightarrow d_{x^2-y^2}$	2 x $E_g$	Forbidden	$10^3-10^2$
	2 x $E_u$	x, y	$10^{3b}$

<sup>a</sup> $D_{4h}$  symmetries of singlet excited states generated from the corresponding orbital transition. All non-degenerate ungerade states have a double group  $E_u$  triplet component that is x, y polarized.  $^1E_u$  states have both an  $A_{2u}$  (z polarized) and an  $E_u$  (x, y polarized) triplet component.

<sup>b</sup>Although formally allowed, this transition is expected to be weak because of the  $g \rightarrow g$  parentage of the monomer transition.

possible transitions in the molecular orbital diagram in Figure 5. These polarizations and selection rules are those expected for a dimer of  $D_{4h}$  symmetry. In fact,  $Rh_2(TMB)_4(PF_6)_2$  has only  $D_2$  symmetry at its crystallographic site and  $Rh_2(b)_4(Bph_4)_2$  preserves only the mirror plane relating the two metal ions in the crystal. In this case, emphasis must be placed on the important role of an effective molecular symmetry which may vary depending on the particular property in question. The  $D_{4h}$  point group seems to be the effective symmetry for the intense features in  $Rh_2(b)_4(Bph_4)_2$ . In the following treatment on this dimer this point group will be used to designate the electronic states, molecular orbitals, and vibrational modes. The other rhodium diisocyanides can have only  $D_4$  symmetry due to the lack of the inversion operation caused by the partially staggered ligand configuration. When considering spin forbidden transitions, the double group  $\bar{D}_{4h}$  or  $\bar{D}_4$ , which includes the symmetry of electron spin into the analysis, will be point groups chosen to denote the electronic terms. It will be clear from the data that these molecules certainly display a distinct tendency to retain their axial symmetry regardless of their crystallographic site.

Figure 6 shows the single crystal polarized absorption spectrum of  $Rh_2(TMB)_4(Bph_4)_2$ . The orientation of the metal-metal axis is not known in this particular salt.

Crystal thickness is estimated from the solution spectrum to be about .3  $\mu\text{m}$ . Figure 7 shows the single crystal polarized spectrum of a sample of  $\text{Rh}_2(\text{b})_4(\text{Bph}_4)_4 \cdot \text{CH}_3\text{CN}$ . The crystal structure<sup>24</sup> shows the metal-metal axis to be exactly coincident with the crystallographic b axis. This spectrum was obtained on the (100) face of this monoclinic crystal.<sup>34</sup> Since symmetry demands the extinction directions to be parallel and perpendicular to the b axis, these two polarizations are placed precisely parallel and perpendicular to the molecular metal-metal bond. Crystals sufficiently thin to obtain the entire optical spectrum for this salt on a reasonable absorbance scale were not produced. By analogy to the structure and spectrum of this crystal of known orientation, the molecular polarizations of the thin crystal of  $\text{Rh}_2(\text{TMB})_4(\text{Bph}_4)_2$  can be identified. There are a number of spectral features of varying intensity and polarization listed in Table 2.

The assignment of most of these bands is rather straightforward. The lowest energy allowed transition at 533 nm ( $18760 \text{ cm}^{-1}$ ) is assigned as  ${}^1\text{A}_1 \rightarrow {}^1\text{A}_2$  ( $4d_{xz,yz} \rightarrow 5p_z \sigma, \pi^* \text{CNR}$ ). The observed polarizations are those expected from these transitions in the  $\text{D}_4$  point group. These polarizations with the two allowed transitions parallel and perpendicular to the metal-metal axis confirm the assignments proposed by Mann and Gray.

Figure 5. Molecular orbital diagram for the interaction of two square planar  $d^8$  metal ions complexed with isocyanide ligands.

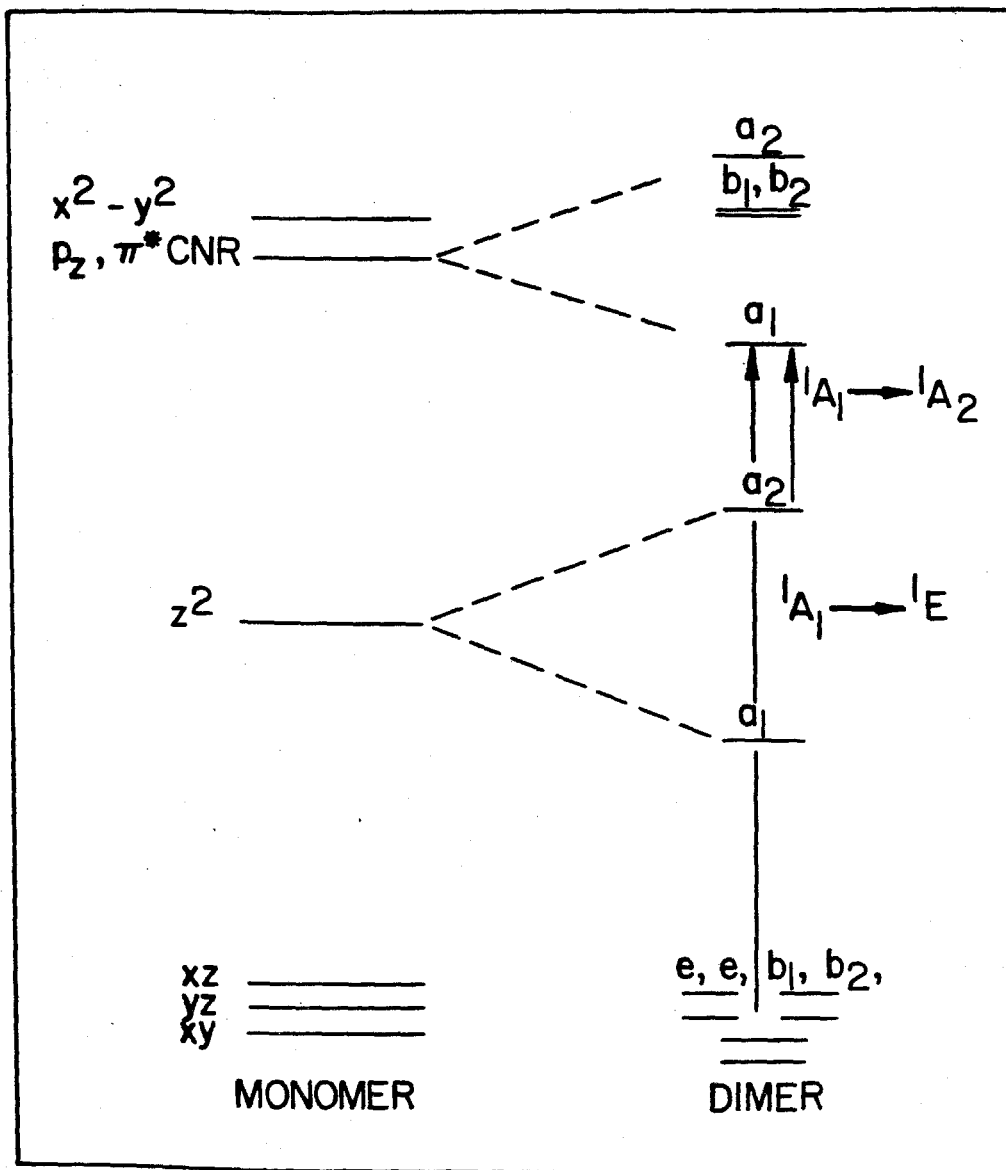


Figure 6. Single crystal absorption spectrum of a very thin ( $\sim 0.3 \mu$ ) crystal of  $\text{Rh}_2(\text{TMB})_4(\text{Bph}_4)$  at 300K; perpendicular polarization (dashed line), and parallel polarization (solid line).

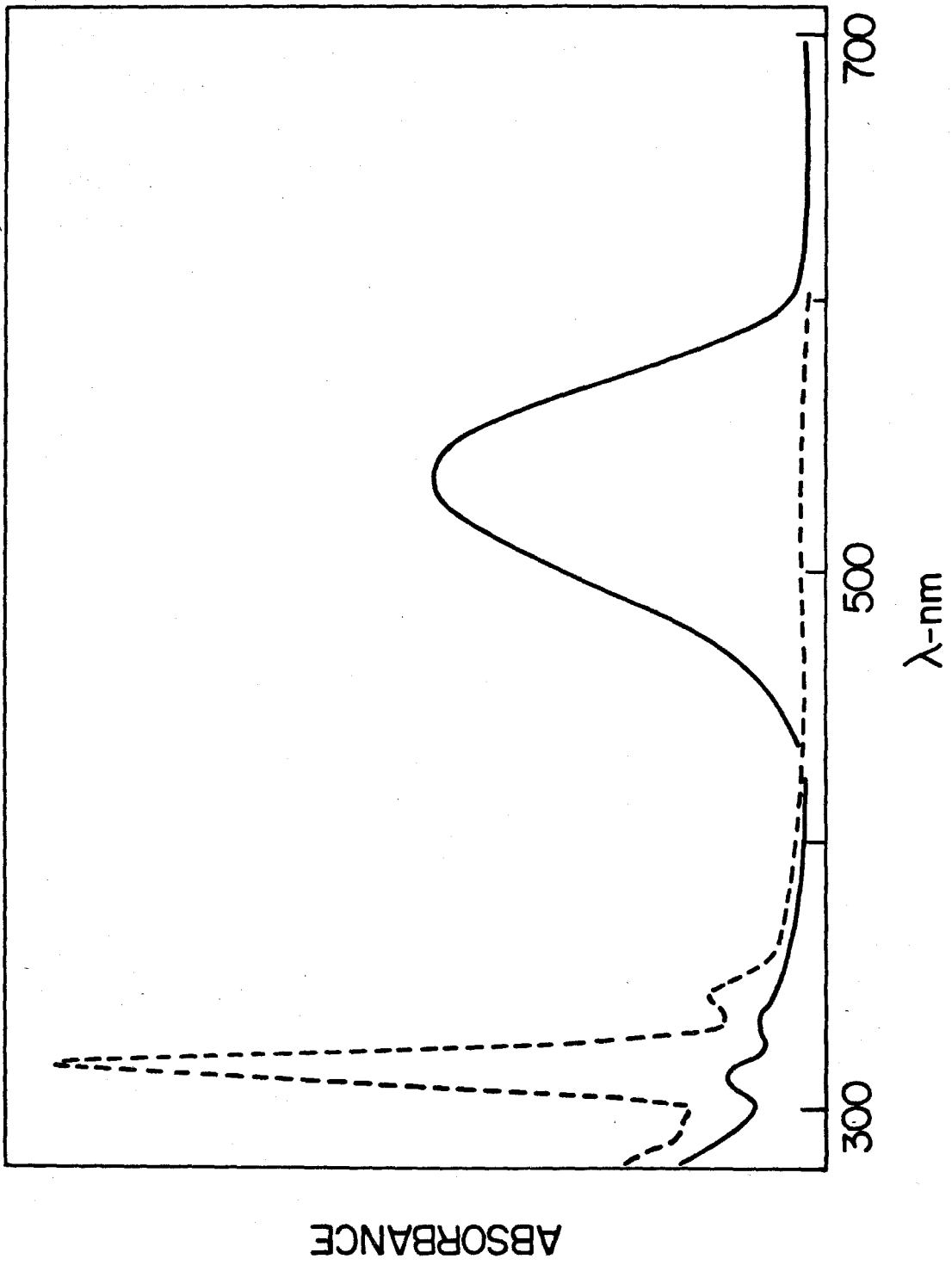


Figure 7. Single crystal absorption spectrum of a thin sample of  $\text{Rh}_2(\text{b})_4(\text{Bph}_4)_2$  at 5K; (z) parallel polarization (dashed line) and (x,y) perpendicular polarization (solid line).

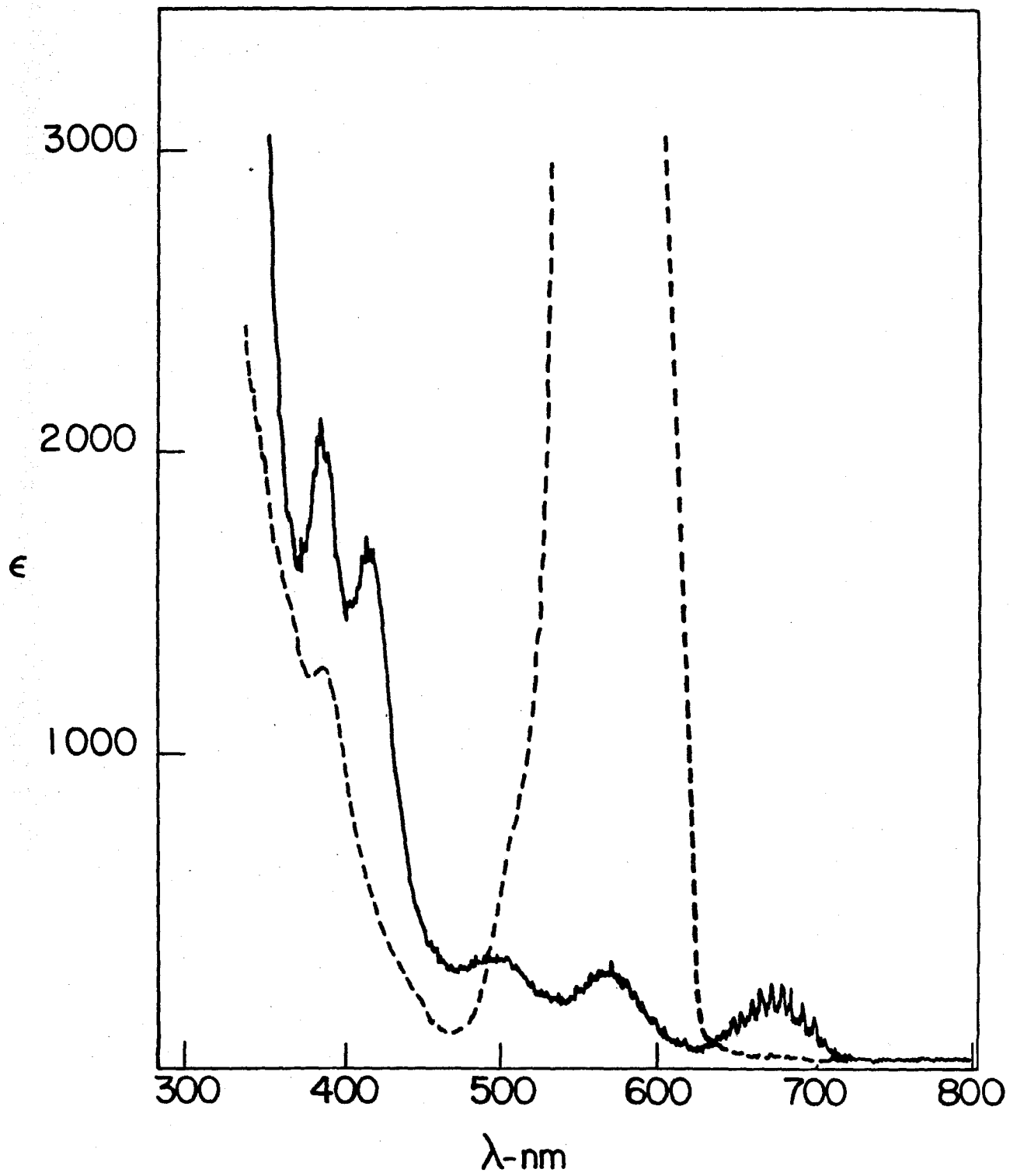


TABLE 2

Band	Polarization	Assignment
533 nm	z	$d_{2\sigma^*} \rightarrow p, \pi^*$ $1_{A_1}^z \rightarrow 2_{A_2}$
380 nm	z	$d_{xy} \rightarrow d_{x^2-y^2}$ $1_{A_1} \rightarrow 1_{A_2}$
342 nm	x,y	$d_{xz,yz} \rightarrow p_z, \pi^*$ $\rightarrow 3_E(E)$
335 nm	z	$d_{xz,yz} \rightarrow p_z, \pi^*$ $1_{A_1} \rightarrow 3_E(A_2)$
316 nm	x,y	$d_{xz,yz} \rightarrow p_z, \pi^*$ $1_{A_1} \rightarrow 1_E$
313 nm	z <sup>a</sup>	$d_{xy} \rightarrow p_z, \pi^*$ $1_{A_1} \rightarrow 1_{B_1}, 1_{B_2}$
296 nm	x,y	$d_{xz,yz} \rightarrow p_z, \pi^*$ $1_{A_1} (v=0, CNR) \rightarrow$ $1_E (v=1, CNR)$

<sup>a</sup>x,y polarization obscured by the absorption at 313 nm.

Several smaller bands are observed in addition to the dominant transitions in the spectrum. In particular, the intense absorption at 316 nm ( ${}^1A_1 \rightarrow {}^1E$ ) is surrounded by a number of bands: 342 nm (x,y polarized), 335 nm (z polarized), 313 nm (z polarized), and 296 nm (x,y polarized).

Consider the states obtained by including spin orbit coupling with the Hamiltonian described by their double group representations:  ${}^1E \rightarrow E$ ,  ${}^3E \rightarrow A_1 + A_2 + B_1 + B_2 + E$ . Two of these five triplet states can gain absorption intensity through mixing with singlets that transform with the same irreducible representations in the double group.  ${}^3E(E)$  can interact with  ${}^1E(E)$  lying only a few hundred wavenumbers away.  ${}^3E(A_2)$  can interact with  ${}^1A_2(A_2)$ , the intense absorption band at 533 nm. We would expect to see these two transitions at slightly lower energy than the  ${}^1E$  band; the  $A_2$  state should have a z polarized transition and the transition to the E state should be x,y polarized. These two bands are observed and assigned as such,  ${}^1A_1 \rightarrow {}^3E(E)$  at 342 nm and  ${}^1A_1 \rightarrow {}^3E(A_2)$  at 335 nm.

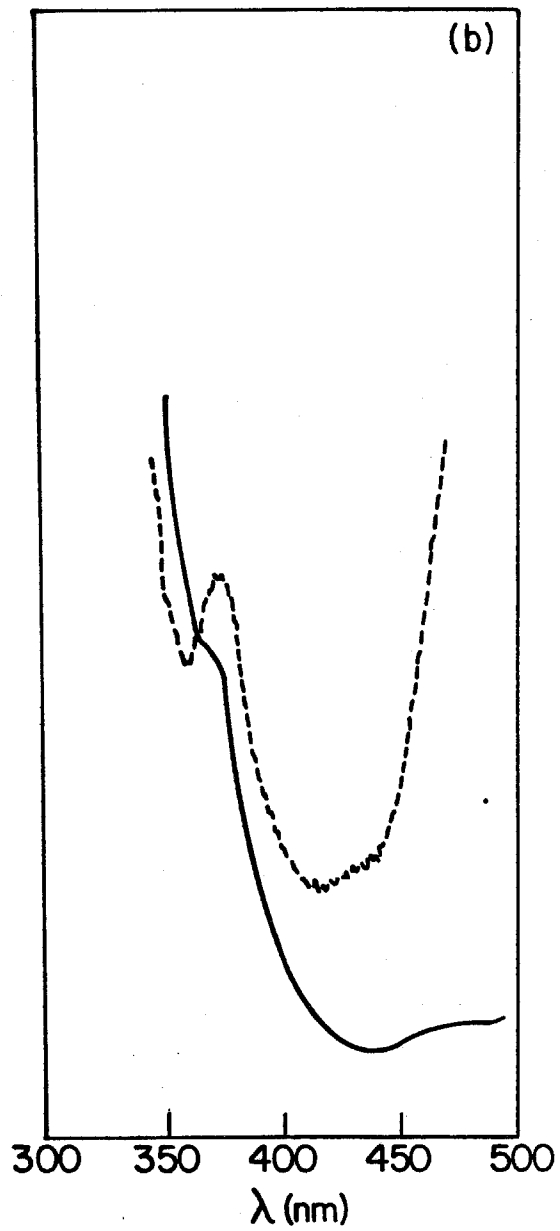
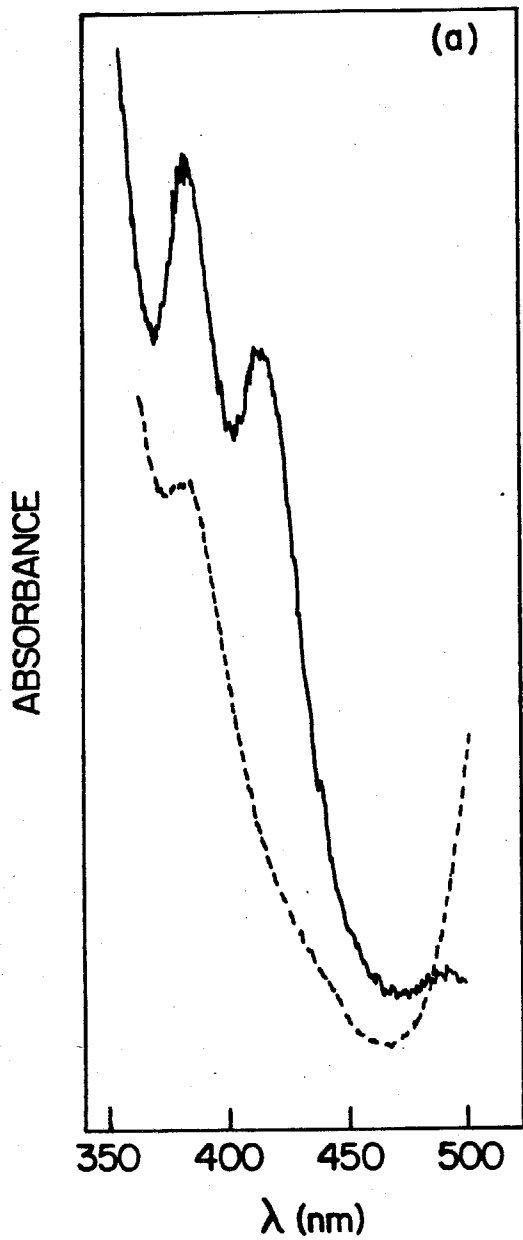
To higher energy from the  ${}^1E$  is a weak absorption with z polarization at 313 nm. It may also be present in the x,y polarization; however, the intense  ${}^1E$  obscures this energy region. A concrete assignment of this band is not possible based simply on the polarized spectra of these dimers. By consulting the work done on monomeric d<sup>8</sup>

$\pi$  acceptor complexes,<sup>29,30</sup> it appears as though a logical assignment would be  ${}^1A_1 \rightarrow {}^1B_1$  ( $4d_{xy} \rightarrow 5 p_z, \pi^*CNR$ ). This transition would be expected to lie in this energy region. The sizeable transition moment for this band probably results from the actual site symmetry of the molecule in the crystalline state. Although formally forbidden in  $D_4$  ( $B_1, B_2 \times A_1 = B_1, B_2$ ), lower symmetry such as  $D_2$  would result in a z polarized transition as is observed.

The highest energy band discernible in this salt, before the phenyl absorption of  $Bph_4^-$ , is an x,y polarized transition located at 296 nm ( $33780 \text{ cm}^{-1}$ ). It is  $2130 \text{ cm}^{-1}$  above the maximum of the  ${}^1E$  and is assigned as the first component of a totally symmetric progression in the  ${}^1E$  absorption of the CN stretching frequency,  ${}^1A_{1v=0} \rightarrow E_{v=1}$ .

Figure 8 shows the spectra of thicker samples of these two rhodium(I) isocyanide dimers in the 450  $\rightarrow$  360 nm region. In both  $Rh_2(TMB)_4(Bph_4)_2$  and  $Rh_2(b)_4(Bph_4)_2$  there is a band system placing its intense components at about 380 nm. In  $Rh_2(b)_4(Bph_4)_2$  there are four distinct bands present at low temperature.  $Rh_2(TMB)_4(Bph_4)_2$  exhibits only two bands; one intense and one quite weak. In  $D_{4h}$  or  $D_4$  the fully allowed bands  ${}^1A_1 \rightarrow {}^1A_2$  and  ${}^1A_1 \rightarrow {}^1E$  possess  $\epsilon$ 's on the order of  $10^4$ . These weaker bands have extinction coefficients on the order of  $10^3$ , suggesting they are transitions that are not fully allowed.

Figure 8. a) Absorption spectrum of  $\text{Rh}_2(\text{b})_4(\text{Bph}_4)_2$  at 5K; (z) parallel polarization (dashed line), (x,y) perpendicular polarization (solid line).  
b) Absorption spectrum of  $\text{Rh}_2(\text{TMB})_4(\text{Bph}_4)_2$  at 5K; (z) parallel polarization (dashed line), (x,y) perpendicular polarization (solid line).



There are several candidates for this transition terminating in  $4d_{x^2-y^2}$  (metal ligand antibonding):  $4d_{z^2\sigma^*,\sigma} \rightarrow 4d_{x^2-y^2}$ ,  $4d_{xy} \rightarrow 4d_{x^2-y^2}$ , and  $4d_{xz,yz} \rightarrow 4d_{x^2-y^2}$ . Table 3 examines the symmetry of these states in various point groups lower than  $D_4$ . Because these bands at 380 nm are not fully allowed, it is likely that the lower symmetry of the molecule as a result of ligand conformation is responsible for the transition intensity. The most useful piece of information regarding the assignment of this band system is the comparison of this spectral region between  $Rh_2(b)_4^{2+}$  and  $Rh_2(TMB)_4^{2+}$ . The  $C_s$  site symmetry of  $Rh_2(b)_4(Bph_4)_2 \cdot CH_3CN$  possessing only a mirror plane that relates the two rhodium centers differs significantly from  $Rh_2(TMB)_4(Bph_4)_2$  where no mirror plane can exist. In  $Rh_2(TMB)_4(PF_6)_2 \cdot 2CH_3CN$  the site symmetry is  $D_2$ .  $Rh_2(TMB)_4(Bph_4)_2$  does not have such high symmetry and presumably preserves only an equatorial  $C_2$ .

The eclipsed configuration of  $Rh_2(b)_4^{2+}$  allows for an interaction of  $\delta$  and  $\delta^*$  symmetry for the  $4d_{x^2-y^2}$  and  $4d_{xy}$  orbitals. A skewed geometry diminishes the size of this interaction substantially. Considering the possibilities for these transitions in  $Rh_2(b)_4^{2+}$  it is seen that  $d_{z^2\sigma} \rightarrow d_{x^2-y^2}$  and  $d_{z^2\sigma^*} \rightarrow d_{x^2-y^2}$  produce only two bands each. Because  $\sigma$  and  $\sigma^*$  are split significantly in these molecules, we would expect to see only transitions from one or the other in any given band system covering

TABLE 3

	<u>D<sub>4h</sub></u>	<u>D<sub>4</sub></u>	<u>D<sub>2</sub></u>	<u>C<sub>2</sub>(x)</u>	<u>m(z)</u>
$d_{z^2\sigma} \rightarrow d_{x^2-y^2}$	B <sub>1g</sub>	B <sub>1</sub>	A	A	A'
	B <sub>2u</sub>	B <sub>2</sub>	B <sub>1</sub>	B	A''
$d_{z^2\sigma^*} \rightarrow d_{x^2-y^2}$	B <sub>2u</sub>	B <sub>2</sub>	B <sub>1</sub>	B	A''
	B <sub>1g</sub>	B <sub>1</sub>	A	A	A'
$d_{xz,yz} \rightarrow d_{x^2-y^2}$	E <sub>g</sub>	E	B <sub>2</sub> , B <sub>3</sub>	A, B	A'', A''
	E <sub>u</sub>	E	B <sub>2</sub> , B <sub>3</sub>	A, B	A', A'
$d_{xy} \rightarrow d_{x^2-y^2}$ b→b b→a a→b a→a	A <sub>2g</sub>	A <sub>2</sub>	B <sub>1</sub>	B	A'
	A <sub>1u</sub>	A <sub>1</sub>	A	A	A''
	A <sub>1u</sub>	A <sub>1</sub>	A	A	A''
	A <sub>2g</sub>	A <sub>2</sub>	B <sub>1</sub>	B	A'
z x, y	A <sub>2u</sub>	A <sub>2</sub>	B <sub>1</sub>	B	A''
	E <sub>u</sub>	E	B <sub>2</sub> , B <sub>3</sub>	A, B	A', A'

about a thousand wavenumbers. In addition,  $d_{z^2\sigma^*}$  and  $d_{z^2\sigma}$  are sensitive to the metal-metal distance whereas the 380 nm system is not. The  ${}^1A_{2u}$  energies for  $Rh_2(b)_4^{2+}$  and  $Rh_2(TMB)_4^{2+}$  differ by  $1700\text{ cm}^{-1}$  but both molecules have a distinct transition at about 380 nm. These arguments rule out an assignment of  $d_{z^2}(\sigma\text{ or } \sigma^*) \rightarrow d_{x^2-y^2}$ .

The transition  $d_{xz,yz} \rightarrow d_{x^2-y^2}$  can be ruled out based on selection rules in the point groups for these two molecules.  $C_2(x)$  and  $m(z)$  allow for both x,y and z polarized transitions, but because of the  $g \rightarrow g$  parentage in higher symmetry, the z transitions are not expected to be as intense as those that are x,y polarized. In  $C_2(x)$ , upon considering that the polarization character in this formally z allowed band is predominantly in the y component (notice the correlation from  $D_2$ ), the z intensity is not expected to be competitive with the x,y intensity as in the spectrum.

This leaves the assignment of this band as  $d_{xy} \rightarrow d_{x^2-y^2}$ . The data agree with this assignment to an astonishing extent for a formally forbidden transition. It is likely that the  $\delta$ - $\delta^*$  splitting for both  $d_{x^2-y^2}$  and  $d_{xy}$  will be similar since in the absence of ligands they are a degenerate set. There are four bands predicted in this description: a pair of states accidentally degenerate described as  $\delta^*xy \rightarrow \delta^*x^2-y^2$  and  $\delta^b_{xy} \rightarrow \delta^b_{x^2-y^2}$ , and two bands split by twice the  $\delta$  interaction,  $\delta^b_{xy} \rightarrow \delta^*x^2-y^2$  and

$\delta^*xy \rightarrow \delta^b x^2-y^2$ . The first two produce  ${}^1A_{2g}$  states and the second two produce  ${}^1A_{1u}$  states in  $D_{4h}$ . They are  ${}^1A_2$  and  ${}^1A_1$  in  $D_4$ .

The site symmetry of the  $Rh_2(b)_4^{2+}$  ion makes all of these transitions allowed. The first two should be close in energy and x,y(a') polarized. The others should straddle the two A' states and be z polarized. This is exactly what is observed: z polarized bands at 382 nm and 435 nm and x,y polarized bands at 387 nm and 415 nm. As was mentioned before, the site symmetry of  $Rh_2(TMB)_4^{2+}$  as the  $PF_6^-$  salt is  $D_2$ . Other salts probably possess lower site symmetry, perhaps  $C_2(x)$ .  $D_2$  predicts only two allowed transitions to  ${}^1B_1$  states, both z polarized.  $C_2(x)$  symmetry predicts all four states to be allowed, two in x polarization and two in y and z. In  $Rh_2(TMB)_4^{2+}$ , because of the lack of  $\delta$  bonding, these states are not expected to be split. A broad band, present in both z and x,y polarization is observed at 385 nm. The z polarization, however, is distinctly more intense than the x,y directions suggesting that the effective symmetry may be  $D_2$  in all cases.

Based on the above argument, the set of transitions at 420 nm - 380 nm that appears to remain energy invariant for this whole class of molecules is due to transitions to  $4d_{x^2-y^2}$  from  $4d_{xy}$ .

It is interesting to comment on the presence of  $\delta$  splitting at such a long distance ( $3.24 \text{ \AA}$ ). The actual energy difference observed for the location of these states in the spectrum of  $\text{Rh}_2(\text{b})_4^{2+}$  is not only a consequence of the  $\delta$  interaction, but is also the result of any configurational interaction between states of the same symmetry. This accounts for the splitting observed in the x,y polarized spectrum of  $\text{Rh}_2(\text{b})_4(\text{Bph}_4)_2$ . Therefore, the z polarized splitting of  $3200 \text{ cm}^{-1}$  is not truly representative of twice the  $\delta$  interaction. Because of these additional effects, the extraction of a value representing the strength of the  $\delta$  interaction is not possible.

One state easily observed in the monomer spectra is that assigned to  $^1\text{A}_{1g} \rightarrow ^3\text{A}_{2u}$  located at 434 nm ( $\epsilon = 260$ ) in  $\text{Rh}(\text{CNEt})_4^{+30}$ . Because of the shift in energy of the  $^1\text{A}_{2u}$  upon dimerization, the  $^3\text{A}_{2u}$  would be expected to be at slightly lower energy than this singlet in the dimer. In order to predict the polarization of this state double group selection rules must be consulted.

$^3\text{A}_{2u}$  transforms as  $\text{A}_{1u}$  and  $\text{E}_{1u}$  in the spin orbit double group  $\bar{\text{D}}_{4h}$ . The electric dipole operator transforms as  $\text{E}_{1u}$  and  $\text{A}_{2u}$ . The transition intensity of  $^1\text{A}_{1g} \rightarrow ^3\text{A}_{2u}$  will therefore lie in the  $\text{E}_{1u}$  (x,y) polarization. Although the singlet will be z polarized, the corresponding triplet is expected to have x,y polarization as the allowed direction.

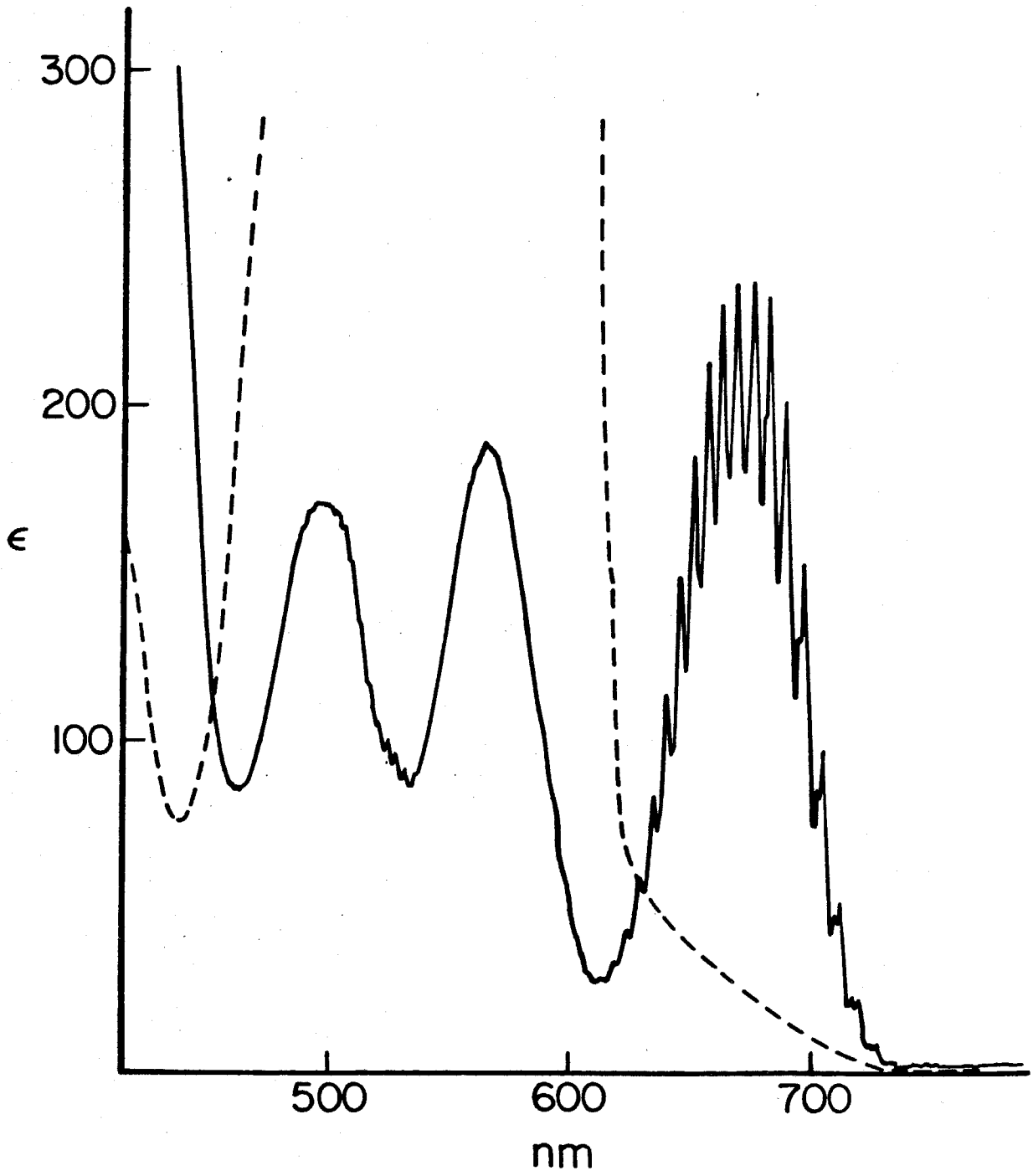
The spectra of  $\text{Rh}_2(\text{b})_4(\text{Bph}_4)_2$  and  $\text{Rh}_2(\text{TMB})_4(\text{Bph}_4)_2$  exhibit an x,y polarized band ( $\epsilon \sim 100$ ) a few thousand wave numbers below the  ${}^1\text{A}_{1g} \rightarrow {}^1\text{A}_{2u}$  transition at 650 nm and is assigned as  ${}^1\text{A}_{1g} \rightarrow {}^3\text{A}_{2u}(\text{E}_u)$  ( $4d_{z^2}\sigma^* \rightarrow 5p_z\sigma, \pi^*\text{CNR}$ ). This region is shown in Figure 9.

Comparing the intensity of  ${}^1\text{A}_{1g} \rightarrow {}^3\text{A}_{2u}$  in the dimers ( $\epsilon \sim 40\text{-}80$  per Rh) with the intensity for the corresponding transition in monomeric rhodium(I) isocyanides ( $\epsilon \sim 200\text{-}500$  per Rh) presents an interesting example of the high effective symmetry of these states. In the above selection rule discussion the presence of an  $\text{E}_{1u}$  component in the double group does not alone enable  ${}^3\text{A}_{2u}(\text{E}_{1u})$  to gain any transition intensity.  ${}^3\text{A}_{2u}(\text{E}_{1u})$  must be able to mix in some singlet wave function of the same double group irreducible representation. The nearest double group  $\text{E}_{1u}$  with singlet character is the  ${}^1\text{E}_u$  state at 316 nm. To first order, a spin orbit interaction will alter the  ${}^3\text{A}_{2u}(\text{E}_{1u})$  wave function as

$$|{}^3\text{A}_{2u}'\rangle = |{}^3\text{A}_{2u}\rangle + |{}^1\text{E}_u\rangle \frac{\langle {}^1\text{E}_u | \text{H}_{\text{SO}} | {}^3\text{A}_{2u}\rangle}{E_{3\text{A}_{2u}} - E_{1\text{E}_u}} .$$

The coefficient of the  ${}^1\text{E}_u$  part of the wave function is inversely proportional to the energy separation between the two states in question. The transition intensity will be proportional to the square of

Figure 9. Absorption spectrum of the visible region in the  
(x,y) perpendicular polarization (solid line) and  
(z) parallel polarization (dashed line) of  
 $\text{Rh}_2(\text{b})_4(\text{Bph}_4)_2 \cdot \text{CH}_3\text{CN}$ .



$$\langle {}^3A_{2u} | r | {}^1A_{1g} \rangle = \langle {}^3A_{2u} | r | {}^1A_{1g} \rangle + \frac{\langle {}^3A_{2u} | H_{SO} | {}^1E_u \rangle}{E_{3A_{2u}} - E_{1E_u}} \langle {}^1E_u | r | {}^1A_{1g} \rangle .$$

The transition moment for a  ${}^3A_{2u}$  state removed from the  ${}^1E_u$  by a large energy gap, as in the dimers, will be less than that for the monomers where the  ${}^3A_{2u}$ ,  ${}^1E_u$  splitting is much smaller.

The only other potentially assignable bands in the spectrum of  $\text{Rh}_2(\text{b})_4^{2+}$  are the two bands in the x,y polarization at 568 nm and 500 nm along with the sharp structure between them. Because of the temperature dependence and location of the band at 568 nm, it is assigned as  ${}^1A_{1g} \rightarrow {}^1A_{2u}$ . This band can have intensity in the x,y direction by accompanying the pure electronic transition with a change in one quantum of an  $e_g$  mode. The overall symmetry of the excited state is then  $A_{2u} \times E_g = E_u$ . This type of transition, called a vibronic transition, is expected to lose intensity upon cooling due to a depopulation of the  $e_g$  mode in the ground state. Unlike the fully allowed, or spin orbit allowed transitions in this spectrum, this band is almost twice as weak at 5K than at 300K.

The assignment of the other broad band at 500 nm is ambiguous. It appears to follow the position of the

${}^1A_{1g} \rightarrow {}^1A_{2u}$  band in the other rhodium diisocyanides.

It may be simply the  ${}^1A_{1g} \rightarrow {}^1A_{2u}$  with an  $e_g$  CN vibration.

The transition at 296 nm supports this possibility.

Alternatively, a number of transitions such

as  $d_{z^2} \rightarrow d_{x^2-y^2}$  or  $d_{xz,yz} \rightarrow d_{x^2-y^2}$  may be in this energy region.

The sharp structure between these broad bands suggests the presence of another electronic state of significantly different character than these other low lying states. The sharp structure along with an extinction coefficient of only about 5 indicates this state is probably a triplet. It is not distorted in the same way as are the other low lying excited states. This is exhibited by the maximum of the band occurring at about  $\nu = 4$  in a  $130\text{ cm}^{-1}$  mode. The overall width of the structure is only a few hundred wave numbers. Because of this different shape and analogies to a similar band in the platinum dimer discussed in Chapter 4, this band is assigned as  ${}^1A_{1g} \rightarrow {}^3A_{1g}$  ( $4d_{z^2}\sigma \rightarrow 5p_z\sigma, \pi^*CNR$ ). The analysis of the structure and arguments supporting this assignment are presented later.

### Section 3

The spectrum of  $\text{Rh}_2(\text{DMB})_4^{2+}$  in solution is in some ways similar to the other dimers but in other ways quite different. The spectrum is shown in Figure 4c. As in all the  $d^8$  systems there is an intense sharp feature at 310 nm. This is assigned

as  ${}^1A_1 \rightarrow {}^1E$  ( $4d_{xz,yz} \rightarrow 5p_z, \pi^*CNR$ ). The lower energy band is demonstrably different in shape and energy than the  ${}^1A_1 \rightarrow {}^1A_2$  transition in  $Rh_2(b)_4^{2+}$  and  $Rh_2(TMB)_4^{2+}$ . Since the metal-metal distance is 4.47 Å in  $Rh_2(DMB)_4(PF_6)$ , it is interesting that there should be any change in the optical spectrum relative to the separate monomers. The band position and shape can be explained in terms of a weakly interacting pair of monomers producing a pair of  ${}^1A_2$  excited states. One excited state corresponds to a metal metal bonding state and the other corresponds to a metal to ligand charge transfer transition analogous to the  ${}^1A_2$  in the monomers. Figure 5 shows the splitting of  $d_{z^2}(\sigma, \sigma^*)$  and  $p_z, \pi^*CNR(\sigma, \sigma^*)$  set produce two  ${}^1A_1 \rightarrow {}^1A_2$  transitions;  $d_{z^2}\sigma(a_1) \rightarrow p_z\sigma^*, \pi^*CNR(a_2)$  and  $d_{z^2}\sigma^*(a_2) \rightarrow p_z\sigma, \pi^*CNR(a_1)$ . In cases where the metal-metal interaction is strong, these two states are split enough to place the higher energy  ${}^1A_{2u}$  state ( $d_{z^2}\sigma \rightarrow p_z\sigma^*, \pi^*CNR$ ) out of the optical spectrum. At 4.47 Å this splitting is much smaller and both  $\sigma^* \rightarrow \sigma$  and  $\sigma \rightarrow \sigma^*$  are observed.

The shapes of the two transitions in this band suggest the different excited state geometries the  ${}^1A_2$ 's have relative to each other. The lower state ( $\lambda_{max} = 475$ ) is broader than the upper one ( $\lambda_{max} = 420$ ). Examination of the bandwidth of the  ${}^1A_{2u}$  in  $Rh(t-butNC)_4^+$  shows it to be about  $1400\text{ cm}^{-1}$  wide and is relatively temperature independent. The low temperature width for  $Rh_2(TMB)_4^{2+}$  is

about  $1700 \text{ cm}^{-1}$ . More importantly, its 300K bandwidth is about  $2900 \text{ cm}^{-1}$ .

A qualitative description of an excited state geometry can be obtained through an analysis of the width of its absorption band as a function of temperature.<sup>35</sup> Classical potential surface theory states that the normalized second moment of an absorption band is related to vibrations and distortions through the relation

$$M_2 = \sum_i S_i (h\omega_i)^2 \coth \frac{h\omega_i}{2kT}$$

where  $S_i$  is the Huang-Rhys factor, representative of the distortion in the excited state in vibrational mode  $i$ . The vibrational energy  $h\omega_i$  in the coth function determines whether a significant temperature dependence for the second moment will be observed. When  $2kT > h\omega_i$ ,  $\coth h\omega_i/2kT$  becomes linear in temperature. A low energy vibration will allow for a change in  $M_2$  with temperature, provided the two states involved in the transition have different equilibrium geometries along this coordinate.

The two bonding coordinates in which the  $p_z, \sigma^* \text{CNR}$  orbital differs from  $d_{z^2}$  are along the metal-metal and the metal ligand (M-CNR) bonds. In the case of the monomer, the  $d_{z^2} \rightarrow p_z, \pi^* \text{CNR}$  transition can only distort along the metal ligand coordinate having a vibrational frequency of  $460 \text{ cm}^{-1}$ . This will allow the  $\coth \left( \frac{h\omega}{2kT} \right)$  term to range

from 1 to 1.25 from 0K to 300K, predicting a band with a relatively small temperature dependence.

In the  $\text{Rh}_2(\text{DMB})_4^{2+}$ , the two bands composing the low energy system have different temperature dependences. The low energy broad side sharpens up a great deal, but the high energy side is fairly temperature independent. This suggests that the lower energy broad band contains much of the metal-metal character, a much lower energy vibration. The wave function for this state is delocalized over the metal centers whereas the state on the higher energy side appears to be similar to the  ${}^1A_{2u}$  in the individual monomers.

The development of the assignments for many of the states observed in the optical spectrum of rhodium(I) isocyanide dimers is now complete. This study is in a position to develop some of the more detailed information offered by the spectrum of  $\text{Rh}_2(\text{b})_4^{2+}$ . Through the vibronic structure in the  ${}^3A_{2u}$  state in this molecule, details such as the  $d_{z^2}\sigma, \sigma^*$  splitting, ground state and excited state bond energies, and absolute energy changes of the various orbitals of the  $\sigma$  manifold can be determined. Much of the next section will serve to extract the metal-metal bond distance in this low lying  ${}^3A_{2u}$  excited state. This distortion upon electronic excitation is characteristic of a kind of excited state very different from others that have been observed in inorganic compounds.

## Section 4

Absorption and emission bands are not necessarily broad and featureless. In favorable cases, the individual vibronic transitions can be observed in the low temperature crystal spectrum of inorganic species. For both mononuclear and binuclear complexes there are many examples of varying degrees of vibrational structure composing an optical absorption band but there are few examples of structured luminescence<sup>36,37</sup> in inorganic compounds.

In the event vibrational structure is observed, the information contained in the energies and intensities of these individual lines can aid the spectroscopist in a number of ways. It can help with assignments of orbitals involved in the electronic transitions because the orbital composition of one state *vs.* another is intimately related to the bonding in the system. As the bonding changes from one state to another, the equilibrium geometry of the molecule changes as well. The force constants will change appropriately, following an increase or decrease in bond strength. This change in force constant will be represented as a change in vibrational frequencies observed in an absorption spectrum relative to the vibrational frequencies in the emission or raman spectrum.

Several papers have been written on the analysis of a structured absorption or emission band.<sup>37</sup> All are correct within the theoretical framework chosen. The major flaw in most of this work is a rather poor treatment of the application of the theory toward spectroscopic data. There are many pitfalls and subtle considerations associated with this kind of analysis. This section will not only cover the correct theoretical treatment, but also illuminate some of the deceptions that can be present in such an analysis.

The Franck-Condon Principle<sup>38</sup> states that a molecular system upon interaction with light will undergo what is termed a "vertical" transition. The initial state and final state in the adiabatic approximation are represented by

$$|i\rangle = \phi_i(r, Q) \prod_i X_{iv}''(\xi_i)$$

$$|f\rangle = \phi_f(r, Q) \prod_i X_{iv}'(\xi_i)$$

The electric dipole transition moment for an allowed transition between these two states is

$$D_{if} = \langle f | \sum e r_i | i \rangle .$$

Because the electronic absorption process takes place in about  $10^{-16}$  sec and the nuclear vibrations are on the order of  $10^{-14}$  sec, the transition occurs "instantaneously"

relative to the nuclear motions. The dipole moment matrix element is therefore evaluated for both states at the equilibrium coordinates of the ground state. This yields an overall transition moment

$$D_{if} = \langle \phi_f(r,0) | \sum_i r_i | \phi_i(r,0) \rangle \times$$

$$\prod_i \langle \chi_{i v''}''(\xi_i) | \chi_{i v'}'(\xi_i) \rangle .$$

The squares of the overlap integrals  $\langle \chi_{i v''}''(\xi_i) | \chi_{i v'}'(\xi_i) \rangle$  are called the Franck-Condon Factors (FCF). For different vibrational quanta in  $|\chi_{i v'}'(\xi_i)\rangle$  the overlap with the  $v'' = 0$  level of  $|\chi_{i v''}''(\xi_i)\rangle$  will be different. The intensities of a given vibronic transition will be proportional to the square of the corresponding FCF for that vibration.

Writing the potential energy for the vibrational coordinates in the ground state as a harmonic potential results in the vibrational wave functions

$$\chi_{i v''}'' = \sqrt{\sqrt{\frac{\alpha''}{\pi}} \left( \frac{1}{2^{v''} v''!} \right)} \exp\left(-\frac{1}{2} \alpha'' \xi_i^2\right) H_{v''}(\sqrt{\alpha''} \xi_i)$$

where  $\alpha'' = \frac{M\omega''}{\hbar}$ ,  $M$  = effective mass of the vibration, and  $H_{v''}$  is a Hermite polynomial of order  $v''$ . The excited state vibrational wave function for the same coordinate is expressed as

$$\chi'_{iv'} = \left( \frac{\alpha'}{\sqrt{\pi}} \right) \left( \frac{1}{2^{v'} v'!} \right) \exp \left( -\frac{1}{2} \alpha' (\xi_i + \Delta \xi_i)^2 \right) \quad \times$$

$$H_{v'} \left( \sqrt{\alpha'} (\xi_i + \Delta \xi_i) \right)$$

using the coordinates of the ground state equilibrium position.  $\Delta \xi_i$  is the difference in the minima of the potential energy curves representing the excited state and ground state along the coordinate  $\xi_i$ . It can be shown<sup>38</sup> that

$$\langle \chi''_{i0} | \chi'_{iv'} \rangle = \langle \chi''_0 | \chi'_0 \rangle \left( \frac{1}{2^{v'} v'!} \right) \left( \frac{\alpha'' - \alpha'}{\alpha'' + \alpha'} \right)^{\frac{v'}{2}} \quad \times$$

$$H_{v'} \left( \frac{\alpha''}{\alpha'' + \alpha'} \sqrt{\frac{\alpha' (\alpha'' + \alpha')}{\alpha'' + \alpha'}} \Delta \xi_i \right)$$

yielding the intensities of a  $\chi_0^{\text{gr}} \rightarrow \chi_{v'}^{\text{ex}}$  line relative to the  $\chi_0^{\text{gr}} \rightarrow \chi_0^{\text{ex}}$  line of an allowed band. These factors reflect the overall shape of the absorption band.

These overlap integrals can be used to develop the theoretical intensity distribution for either an absorption or emission band. To generate the observed experimental shape, the squares of the overlap integrals must be multiplied by the appropriate energy factors derived from the Einstein relationships

$$\frac{\text{Abs } v=v'}{\text{Abs } v=0} = \left( \frac{\langle \chi_0 | \chi_{v'} \rangle}{\langle \chi_0 | \chi_0 \rangle} \right) \left( \frac{E_{v'}}{E_0} \right)$$

$$\frac{I^{\text{em}}_{v=v''}}{I^{\text{em}}_{v=0}} = \left( \frac{\langle \chi_{v''} | \chi_0 \rangle}{\langle \chi_0 | \chi_0 \rangle} \right)^2 \left( \frac{E_{v''}}{E_0} \right)^4$$

For a molecular electronic transition that results in a distortion along only one normal coordinate these equations will generate values which can then be placed at their appropriate energies to produce a stick diagram representing the calculated bandshape.

There are a number of approximations and assumptions made in the development of these Franck-Condon Factors. Clearly the first and foremost assumption concerns the applicability of the Franck-Condon Principle itself. The transition moment is evaluated at  $Q_0$ , the equilibrium geometry of the initial state, but the molecule in its initial state has a probability of undergoing a transition to the excited state at a geometry different from  $Q_0$ . The Franck-Condon Principle assumes that independent of the true geometry of the molecule at the moment the electronic transition takes place, the matrix elements  $\langle \phi_f(r,0) | \sum e r_i | \phi_i(r,0) \rangle$  are close to the correct values. This approximation could be questioned for molecules with an initial state with a broad minimum, such that  $\chi_{v=0}^i$  has classical turning points at very different geometries.

The next approximation made in this treatment regards the use of harmonic potentials for the development of the vibrational wavefunctions used to calculate the Franck-Condon factors. This is a legitimate assumption provided the observed structured optical transition has evenly spaced vibronic lines.

The third approximation involves the actual normal coordinate description used to get the set of symmetry adapted vibrational wavefunctions. In this approximation, these normal coordinates are chosen so that off diagonal elements connecting these normal coordinates are zero. Because the equilibrium position for the excited state will be different in general from the ground state and the actual potential function, irrespective of the difference in equilibrium geometry, will be different for various internal modes, the linear combinations of these internal modes that produce normal modes will differ somewhat from state to state. This is known as a Duschinsky Effect and can possibly be very important in the development of a Franck-Condon Analysis (FCA).

The next consideration in the FCA deals with the correlation between the calculated diagram and the experimental structured spectrum. The major limitation associated with a stick diagram is that it can only account for progressions in one vibrational mode with one origin. These sticks have no linewidth and cannot account for the

overlap of two vibronic lines. This could be a good representation for small gas phase molecules where lines are typically very sharp. In the solid state, however, individual vibronic lines can have widths on the order of the vibrational spacings. Large molecules frequently distort in several vibrational modes, as a consequence of the fact that the promotion of an electron from one molecular orbital to another involves changes in the bonding along several coordinates. Because the molecular orbitals themselves are symmetry-adapted, they may represent many different "local" interactions.

The best way to avoid these inaccuracies associated with a stick diagram is to realize that the FCF's represent the intensities of a vibronic transition independent of linewidth. Linewidth and shape (gaussian or lorentzian) can be assumed to generate a smooth curve representing the spectroscopic data. The effect of more than one progression and distortion along orthogonal coordinates can be dealt with easily by simply adding the individual contributions of each line at any given wavelength. The parameter affecting the shapes of the overall band,  $\Delta\xi_i$ , can then be adjusted to produce a smooth curve that is the best fit to the actual data.

In practice, the validity of an FCA employing the technique illustrated above is a little more complex than it appears on the surface. Considering simply the calculation of the

band intensities, it can be seen that a number of parameters are required. Both the ground state and excited state frequencies must be known. The vibrational spacings in a structured absorption band yield the excited state frequency for the distorting mode; the raman spectrum can supply the ground state values. If structured emission is present, the ground state frequency can be obtained through the spacings of these lines as well. Correct numbering of the vibrational quanta is also important. The 0-0 transition must be observed in order to get this numbering. An incorrect numbering will mislocate the apparent maximum, resulting in an incorrect fit.

It is also not clear on the surface that a correct value for a distortion,  $\Delta\xi$ , cannot be uniquely determined in practice unless both the excited state and ground state vibrational frequencies are known. The parameters  $\alpha', \alpha''$  and  $\Delta\xi$  are linearly independent in the overlap expression, so they should all be independently adjustable, yielding different bandshapes. The problem lies with the experimentalist's ability to choose the best fit. The overall width of an absorption band is proportional to

$$\sqrt{\frac{(\alpha')^4}{\alpha''}} \Delta\xi^{2/35}$$

at low temperature, according to a potential surface analysis not involving the actual vibrational overlaps. Even in the structured system, any combination of these parameters producing the overall width of a band will yield an approximate fit. In a structured absorption

band,  $\alpha'$  will be known from the spacing in the absorption lines. Unless  $\alpha''$  is also known from emission or raman spectra, there will be a set of solutions for  $\frac{(\Delta\xi)^2}{\alpha''}$  yielding approximately the same width; allowing for  $(\Delta\xi)^2$  and  $\alpha''$  to be grossly incorrect. If both  $\alpha'$  and  $\alpha''$  are known then only  $(\Delta\xi)^2$  is adjusted to fit the bandshape and is thus uniquely determined.

$\alpha'$  and  $\alpha''$  are proportional to the vibrational frequencies in their respective states. These are mass normalized frequencies. In order to get the distortion in terms of a change in bond distance  $\Delta X$ , the correct effective mass for the distorting vibration must be known. This mass is directly related to how the normal modes reflect the internal modes of the molecule. Binuclear metal-metal bonded complexes have an internal mode described by the change in the distance between the two metal nuclei. The effective mass of this vibration is the reduced mass for the atoms involved  $\frac{m_1 m_2}{m_1 + m_2}$ . This internal mode may not be a normal mode of the system. The mass of the ligands can cause this normal mode to have an effective mass different from that of two metals producing a  $|\Delta X|$  somewhat smaller than that which the diatomic approximation yields.

This discussion outlines the theoretical and practical position of a Franck-Condon Analysis of a weakly structured electronic transition. Keeping these approximations and requirements in mind, the next section addresses the spectrum

of  $\text{Rh}_2(\text{b})_4(\text{Bph}_4)_2$  and then applies this type of analysis to determine the geometry of the  ${}^3\text{A}_{2\text{u}}$  excited state.

### Section 5

Figure 9 displays the polarized absorption spectrum of the  ${}^3\text{A}_{2\text{u}}$  in  $\text{Rh}_2(\text{b})_4(\text{Bph}_4)_2$  at 5K. The band consists of 21 distinct peaks with an average spacing of about  $145\text{ cm}^{-1}$ . The origin is located at 751.5 nm. This region is shown in Figure 10. There is a spacing of about  $60\text{ cm}^{-1}$  in addition to the  $145\text{ cm}^{-1}$  progression making the first nine peaks appear as doublets. The linewidth for both members of the doublet may be estimated at about  $70\text{ cm}^{-1}$ . The higher energy lines have considerably larger linewidths resulting in a blending of the doublets into a single band. Table 4 gives the energies of these individual lines.

This is the only  $d^8$  isocyanide compound studied showing this structure. Ligands such as TMB, DMB, or monoisocyanides do not permit this vibrational fine structure at low temperature although there is a distinct  ${}^3\text{A}_{2\text{u}}$  band in the absorption spectrum of their respective rhodium(I) complexes. The molecular orbital diagram suggests the triplet state,  ${}^3\text{A}_{2\text{u}}$  will have the same geometry as the  ${}^1\text{A}_{2\text{u}}$  with the only difference between the two states being the energy of electron pairing. Because the bandshapes of these two transitions are nearly identical,

Figure 10. Origin region of the  ${}^1A_{1g} \rightarrow {}^3A_{2u}$  absorption band  
in  $\text{Rh}_2(\text{b})_4(\text{Bph}_4)_2 \cdot \text{CH}_3\text{CN}$ .

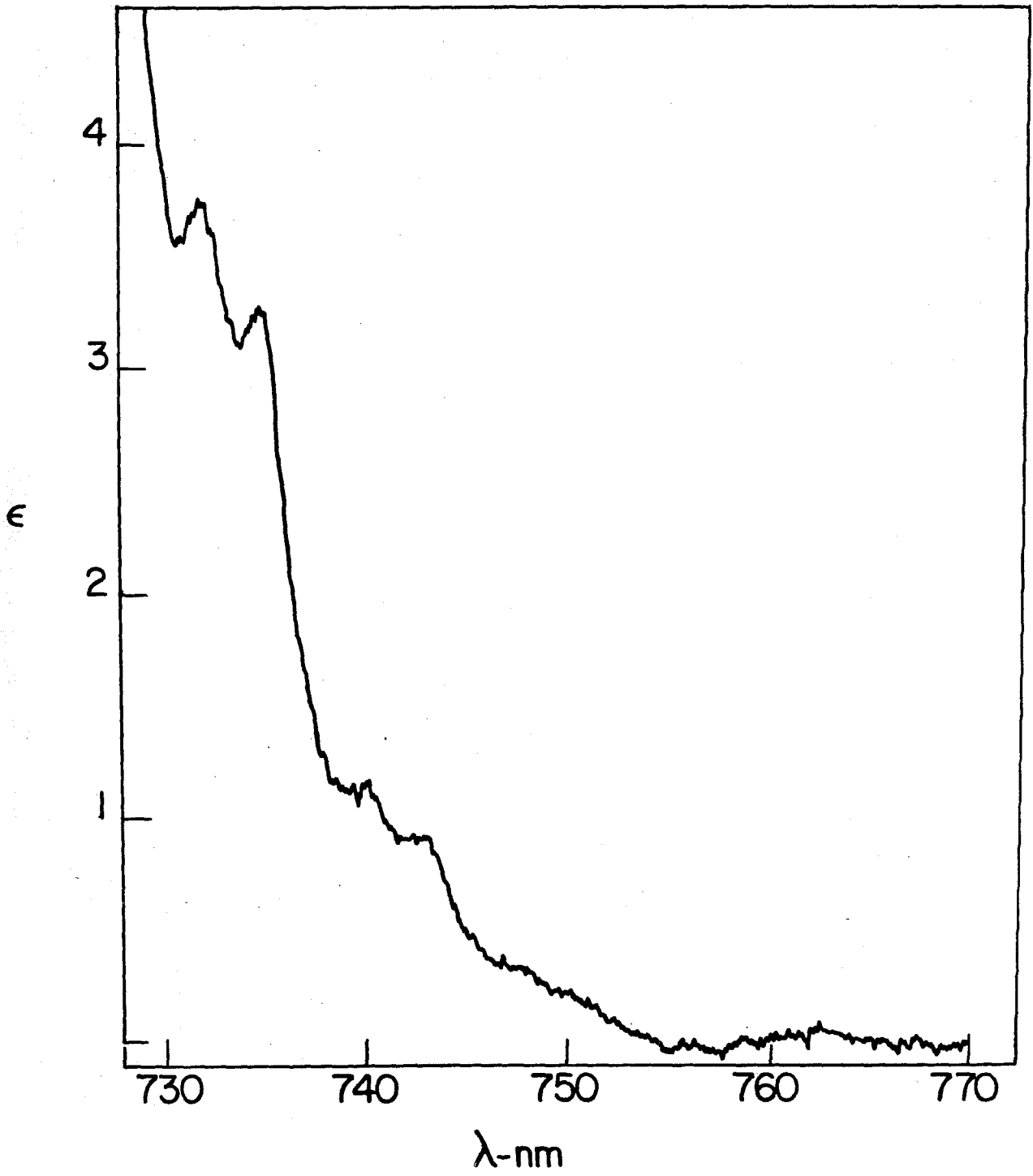


TABLE 4

$v^a$	$E_v$ ( $\text{cm}^{-1}$ )	$\Delta^b$	$E_v - E_{v-1}$
0	13306 13369	63	
1	13455 13513	58	149
2	13607 13661	54	152
3	13752 13805	53	145
4	13897 13943	51	145
5	14040 14094	54	145
6	14188 14232	44	148
7	14331 14376	45	143
8	14479 14513	34	148
9	14619 14662	43	140
10	14764		145
11	14906		142
12	15046		140
13	15186		141
14	15333		146
15	15473		140
16	15613		140
17	15754		141
18	15895		141
19	16033		138
20	16176		143
21	16038		132

<sup>a</sup>The assigned  $a_{1g}$  (Rh-Rh) vibrational quantum number.

<sup>b</sup>Spacings between the principal peak in the progression and secondary (ligand deformation) peaks.

the Franck-Condon Analysis of the structure in the  ${}^3A_{2u}$  will yield the excited state geometries for both of these orbitally equivalent states.

Totally symmetric ground state vibrations are observed in the resonance raman spectrum of both crystals and solution.<sup>40</sup> A progression of three lines in an  $85\text{ cm}^{-1}$  mode is seen as the dominant feature in the crystal. Resonance raman enhances the modes in which the resonant state is distorted from the ground state. Because the  ${}^{1,3}A_{2u}$  distorts predominantly in a  $145\text{ cm}^{-1}$  mode, this frequency of  $85\text{ cm}^{-1}$  correlates to the same mode in the ground state.

The next question is to what mode do these vibrational frequencies of  $145\text{ cm}^{-1}$  and  $85\text{ cm}^{-1}$  correspond; what is the coordinate and effective mass associated with this vibration? All evidence supports the assignment of this vibration as predominantly associated with the metal-metal stretching coordinate. In order for the  ${}^3A_{2u}$  state to have an absorption progressing in this mode, this coordinate must be totally symmetric. The low energy  $a_{1g}$  vibrations of this chromophore are the metal metal stretch, the metal-metal ligand bend, and the metal ligand stretch. The metal ligand stretch is observed about  $465\text{ cm}^{-1}$  in the i.r. and raman spectra, ruling out this vibration as the assignment. The metal-metal ligand bend is expected to be higher than  $85\text{ cm}^{-1}$ , probably higher than  $200\text{ cm}^{-1}$ . In addition,

there is no precedent for a bending vibration to couple so strongly (Huang-Rhys factor  $\sim 10$ ) to an electronic transition. This is because bending coordinates are not directly associated with interatom bonding unlike stretching vibrations. Other binuclear metal complexes are known to show progressions in absorption spectra to high quantum numbers; in all cases this progressing mode is undoubtedly the metal-metal stretch.

The  $60 \text{ cm}^{-1}$  vibration is assigned as a ligand deformation mode. It is possible that it may be due to a lattice mode but the presence of a similar vibration in  $\text{Pt}_2(\text{H}_2\text{P}_2\text{O}_5)_4^{4-}$ , which will be discussed later, suggests that it is a consequence of this bridging molecular structure.

The overall bandshape is generated by measuring the necessary parameters based on the 0-0 and 0-1 transition and varying only one parameter,  $\Delta\xi_{\text{MM}}$ . The calculated best fit and observed spectrum for the overall band and the origin region are displayed in Figures 11 and 12. The values used to calculate this band are

ground state vibration frequency	= $85 \text{ cm}^{-1}$
excited state vibrational frequency	= $148.5 \text{ cm}^{-1}$
0-0 linewidth	= $70 \text{ cm}^{-1}$
second vibration linewidth	= $80 \text{ cm}^{-1}$
splitting of doublet structure	= $57 \text{ cm}^{-1}$
anharmonicity	= $.38 \text{ cm}^{-1}$
second line intensity	= .7
result for best fit ( $\Delta\xi$ )	= $\pm .31 \text{ \AA}$

Figure 11. Comparison of the experimental  ${}^1A_{1g} \rightarrow {}^3A_{2u}$  absorption band (top) and calculated band (bottom).

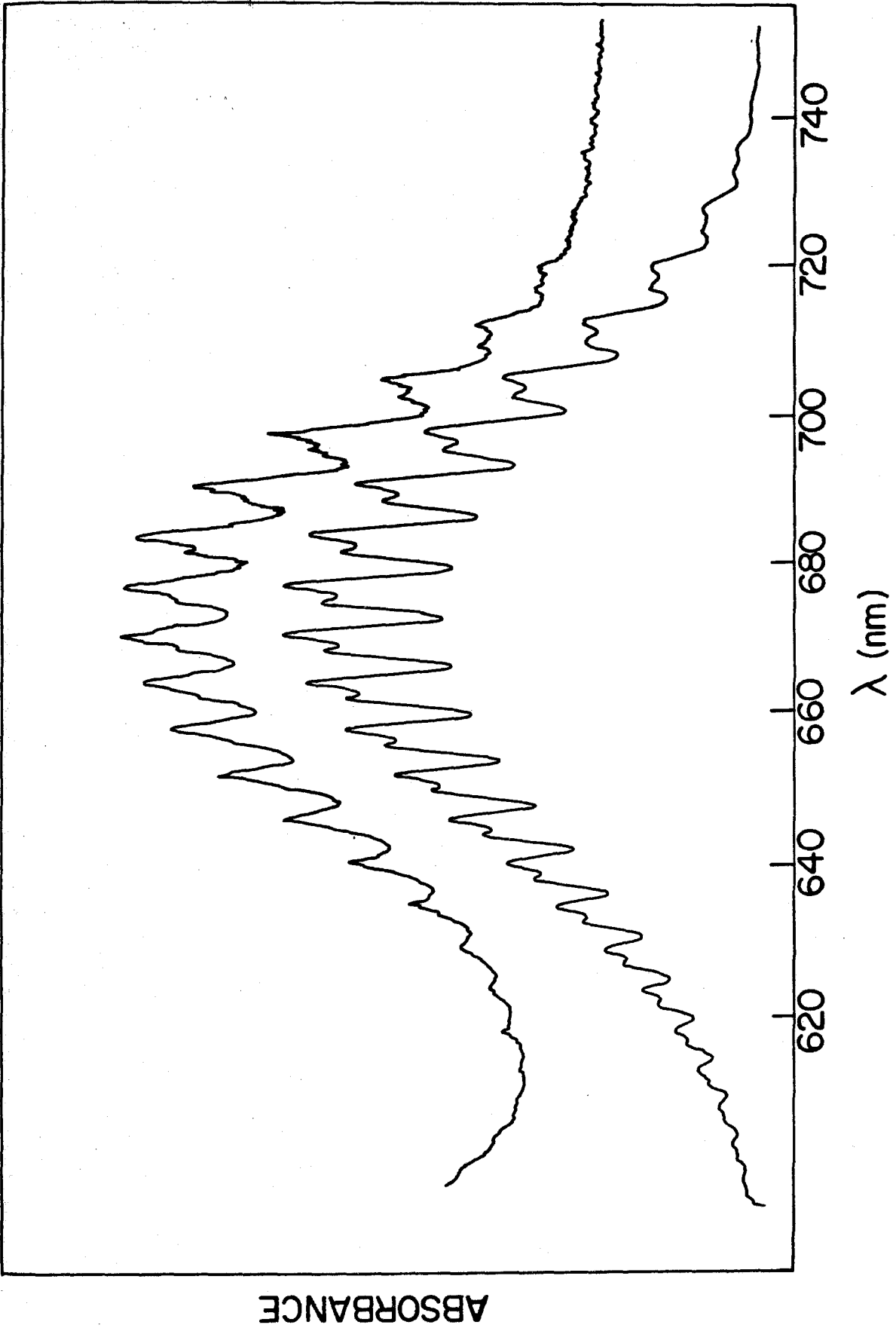
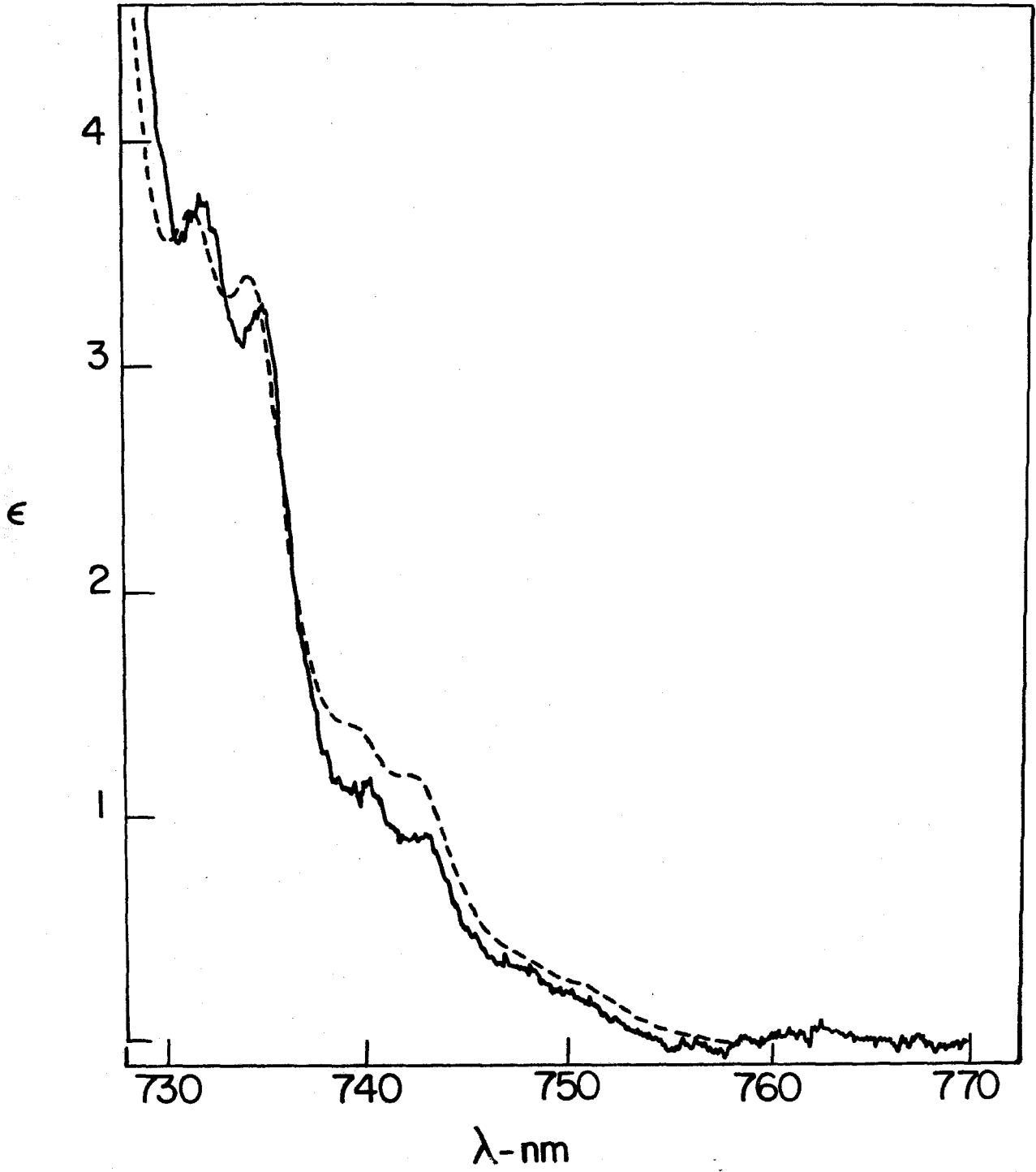


Figure 12. Comparison of the origin region of the  ${}^1A_{1g} \rightarrow {}^3A_{2u}$ ; experimental (solid line) and calculated (dashed line).



The correct  $\Delta\xi$  must not only fit the overall bandshape, but calculate the origin region properly as well. This is a test that can sort out the difficulties mentioned in the previous section involving the relationship between the frequency in the ground state and the geometric distortion variable,  $\Delta\xi$ . A locus of points of a given  $\frac{\Delta\xi^2}{\alpha}$  will reproduce the intense part of the band correctly as was mentioned before, but only one of these solutions will have a correct intensity distribution for  $v = 0:1:2:3$  progression. When both  $\alpha'$  and  $\alpha''$  are known, this region serves as an additional check on the validity of the general treatment. The result for this region is shown in Figure 12.

### Section 6

The  $\Delta\xi$  present in the equation expressing the value of the FCF's has a sign associated with it. It is positive if the excited state has a longer bond along the normal coordinate and negative if there is a contraction associated with the excited state equilibrium bond distance. Because the FCF's are the squares of the Franck-Condon overlaps,  $\Delta\xi$  is only ever represented in the calculation as  $(\Delta\xi)^2$ . A treatment such as this cannot distinguish whether the final state is contracted or expanded relative to the initial state.

In almost all cases for diatomics there is a reciprocal relationship between force constant and bond distance.<sup>41</sup>

The excited state ( ${}^3A_{2u}$ ) vibrational frequency is distinctively

higher than that of the ground state. Provided these vibrations have roughly the same normal coordinate, the diagonal force constant will also be much higher. Badger's rule<sup>42</sup> and other empirical relationships suggest that this increase in force constant denotes a contracted excited state giving this state a shorter bond distance than the ground state. The ground state bond distance between the two metal atoms is 3.24 Å from crystallographic data. The absolute distortion,  $\Delta X$ , is .31 Å if the effective mass is assumed to be that of the two rhodium atoms (diatomic approximation). Another choice of the effective mass would be to use the  $\text{Rh}(\text{CN})_4$  core, resulting in a distortion of .22 Å.

The diatomic approximation has been used for a number of other binuclear systems and produced reasonable results for excited state distortions and distances. There is a good correlation of metal-metal distances and force constants in  $D_{4h}$  dimers when the equatorial ligands are ignored.<sup>43</sup> Because various ligands are used in developing this series, the inclusion of the masses of equatorial ligands would scatter this logical and appealing correlation. Because of the support from these chemical perturbations and correlations, the distortion of .31 Å is favored, but either choice of effective mass results in a sizable contraction for the excited state. The diatomic approximation places the excited state metal-metal distance at  $3.24 \text{ Å} - .31 \text{ Å} = 2.93 \text{ Å}$ .

This distance corresponds closely to that of  $\text{Tc}_2(\text{CO})_{10}$ <sup>44</sup> (3.04 Å) and  $\text{Rh}(\text{b})_4\text{Cl}_2(\text{Bph}_4)_2$  (2.83 Å).<sup>45</sup> These two compounds are  $d^7$  dimers and have a molecular orbital description similar to the  $d^8$  species with one major difference. They are oxidized by two electrons relative to the  $d^8$  systems, having a full metal-metal bond due to no electron density in the  $d_{z^2}\sigma^*$  orbital. The vibrational frequencies for these compounds are  $148\text{ cm}^{-1}$ <sup>46</sup> and  $134\text{ cm}^{-1}$ , respectively. Normal coordinate analysis suggests that the presence of the axial ligands places the true metal-metal stretches closer to  $180\text{ cm}^{-1}$ . The  $149\text{ cm}^{-1}$  fundamental in  $\text{Rh}_2(\text{b})_4^{2+}$  ( ${}^3A_{2u}$ ) indicates almost a full metal-metal  $\sigma$  bond. The molecular orbital description in Figure 4 is consistent with this result. The promotion of an electron from  $d_{z^2}\sigma^*$  to  $p_z\sigma, \pi^*\text{CNR}$  results in a configuration of  $(d_{z^2}\sigma)^2(d_{z^2}\sigma^*)^1(p_z\sigma)^1$ ; three bonding and one antibonding electrons providing a single  $\sigma$  bond.

A vibrationally structured band contains information about dissociation energies. In diatomic molecules the dissociation limits can frequently be observed as the spacings between vibrational quanta decrease until a continuum is reached. This shows the well depth of a state which determines the energy required to completely separate the atoms along the bonding coordinate. Methods have been developed to obtain this dissociation energy

when convergence to a continuum is not observed. One such method is known as a Birge-Sponer<sup>47</sup> extrapolation.

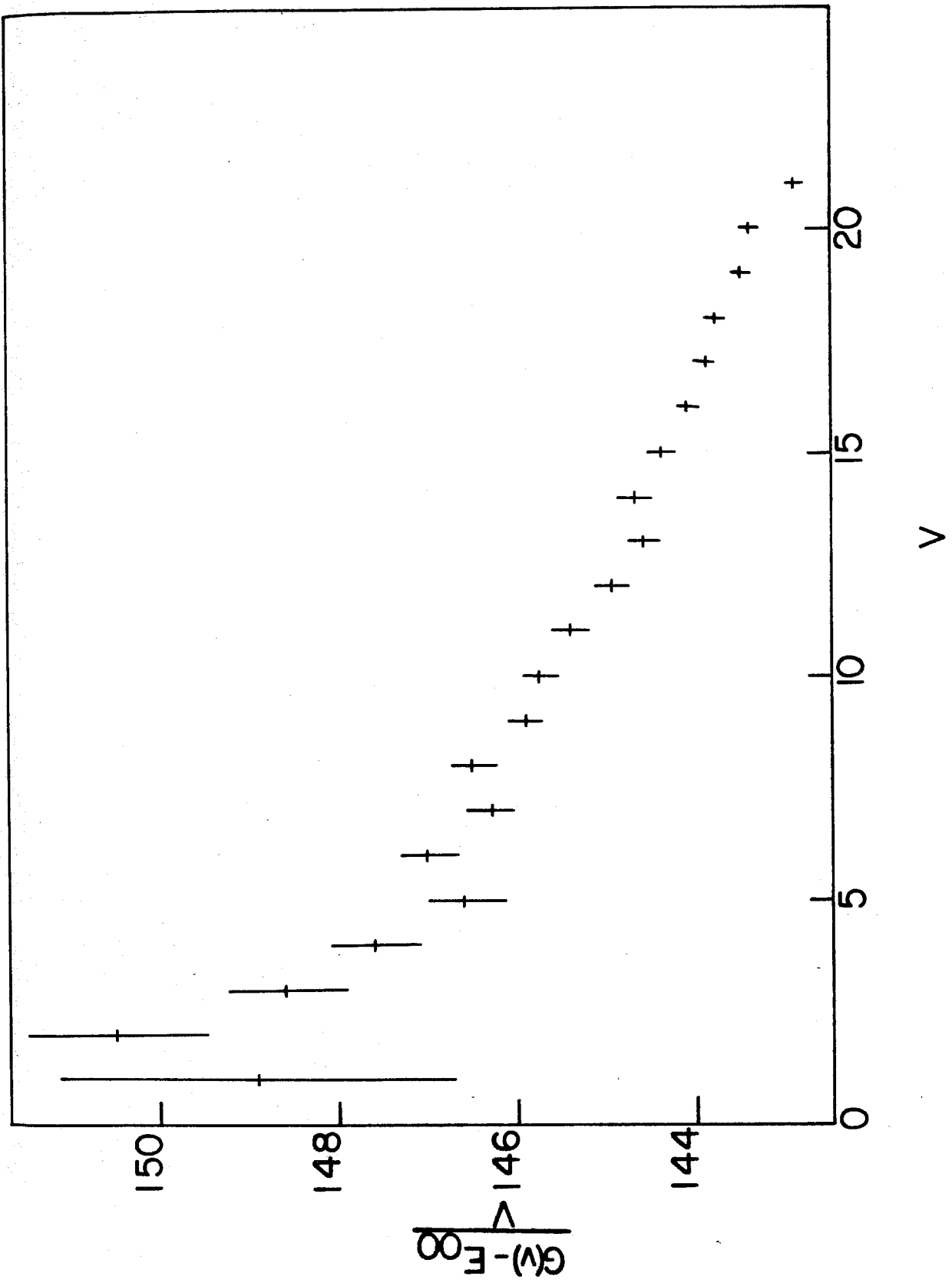
The energy of a given vibrational term for any state can be written as

$$G_0(v) = E_{00} + \hbar\omega_0 v = \hbar\omega_0 x_0 v^2 + \dots$$

By truncating this series after the first anharmonic term, the last vibrational quantum number before dissociation is  $v_D = \frac{\hbar\omega_0}{2\hbar\omega_0 x_0}$ . The dissociation energy  $D_0$  will be  $\frac{\hbar\omega_0^2}{4\omega_0 x_0}$ . If  $\frac{G_0(v) - E_{00}}{v}$  is plotted against  $v$ ,  $\omega_0 x_0$  is obtained as the slope of this line. Figure 13 shows this plot for  $\text{Rh}_2(\text{b})_4^{2+}$ .

The curve in Figure 13 is not a straight line, suggesting that the truncation of the  $G_0(v)$  series is not experimentally sound. We must return to the nature of the entire molecule, including its ligands, to extract some information from this curve.  $\text{Rh}_2(\text{b})_4^{2+}$  has a dissociation energy along the metal-metal coordinate that is not due to bonding interaction between the two rhodium ions but is ultimately dominated by the strength of the bridging ligand and its interaction with the metal ion. For complete dissociation many metal ligand or intraligand bonds must be ruptured. Only in an unbridged metal dimer such as  $\text{M}_2(\text{CO})_{10}$  ( $\text{M} = \text{Mn}, \text{Tc}, \text{Re},$ ) or  $\text{M}_2\text{Cl}_8^{2-}$  ( $\text{M} = \text{Mo}, \text{Re}$ ) in the gas phase would the anharmonicity reflect solely the metal-metal interaction. A better molecule to study would be a dimer

Figure 13. Plot of  $(G(v) - E_{00})/v$  vs.  $v$  reflecting anharmonicity of the  ${}^3A_{2u}$  state in the metal metal vibration.



such as  $[\text{Rh}(\text{CNph})_4]_2^{2+}$ . Unfortunately, none of the dimers of this type examined showed any vibrational structure.

The curvature of the  $G_0(v)/v$  vs.  $v$  plot is positive. In many diatomics where curvature is observed it is negative, indicating most of the higher order terms in the polynomial expansion lower the dissociation threshold. The influence of a bridging ligand and the crystalline state would predict a positive curvature. As the vibrational quanta become larger, the classical turning points for the potential surface occur at more extreme bond distances. The crystal structures for  $\text{Rh}_2(\text{b})_4(\text{Bph}_4)_2$  and  $\text{Rh}_2(\text{b})_4\text{Cl}_2^-(\text{Bph}_4)_2$  suggest 1,3 diisocyanopropane can accommodate distances of 2.83 Å and 3.24 Å. At  $v = 15$  in the  ${}^3A_{2u}$  state with the diatomic approximation the classical turning points are at 2.56 and 3.30 Å. These extreme distances indicate that forces involved in ligand deformation will participate to a greater extent in  $v = 15$  than  $v = 0$ .

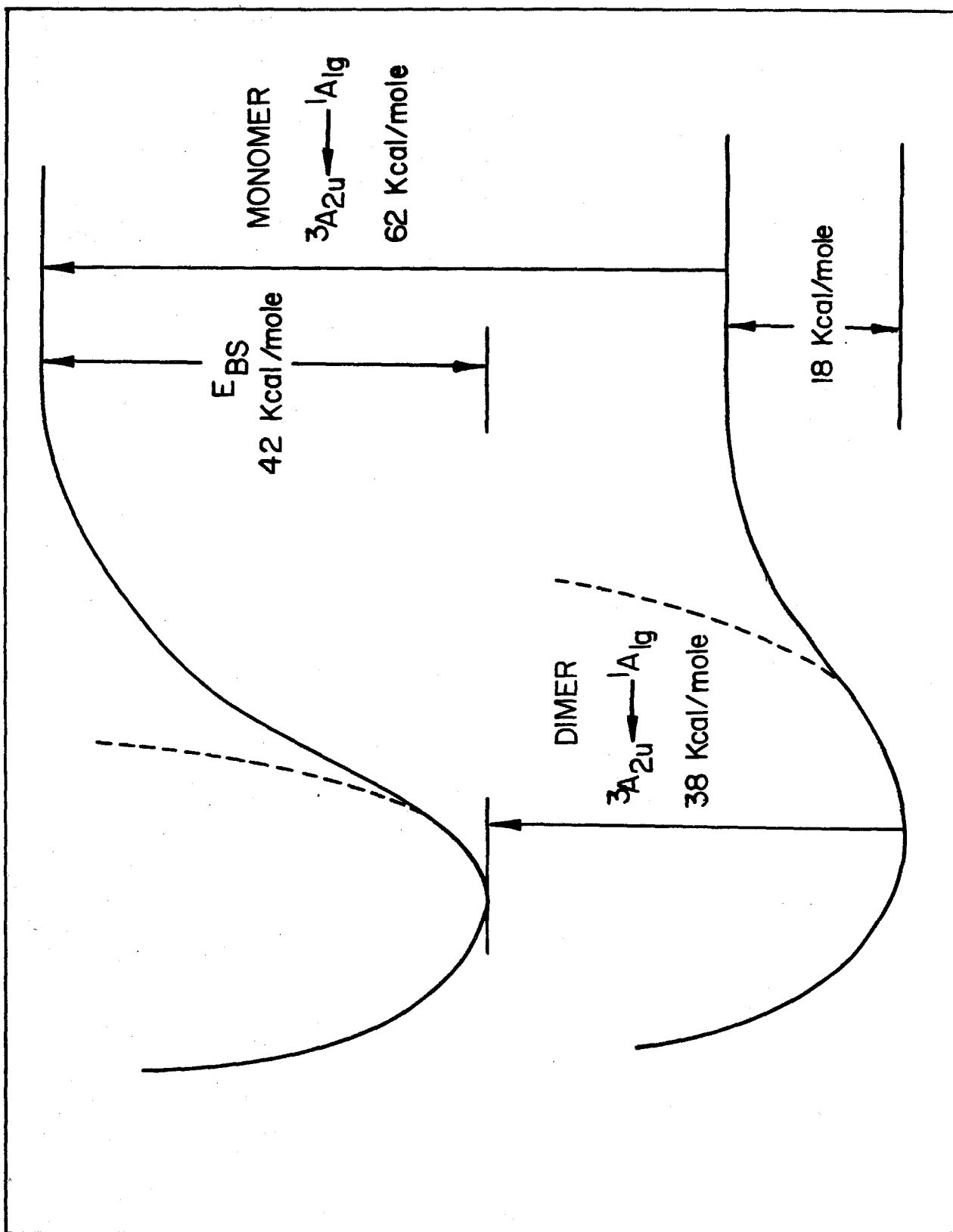
Another reason for this curvature may simply be from an experimental artifact. As the vibrational quantum number increases, the vibronic linewidth increases serving to blend the fundamental progression and the band  $60 \text{ cm}^{-1}$  above into one line. This will shift the apparent maximum of the fundamental progression to higher energy causing a positive curvature for this plot at higher vibrational quanta.

If either of these explanations is correct for the nonlinearity of Figure 13, it can be suggested that the earlier part of the curve (*i.e.*  $v = 0$  to  $v = 10$ ) is representative of the "pure" metal interaction and the surface obtained including this anharmonicity will separate out the "ligand free" contribution to the overall dissociation energy. This interaction, separate from the ligand contribution, contains the information relevant to the molecular orbital description.

The value for the slope from  $v = 0$  to  $v = 10$  is  $\omega_0 x_0 = .38 \text{ cm}^{-1}/\text{quantum number}$ . This yields a  $D_0$  of 42 kcal/mole. This result, although associated with a large error due to the method used, is in good agreement with other estimates of molecules containing single metal metal bonds.

An energy cycle may now be used to calculate the bond energy of the ground state. Figure 14 depicts this cycle. The  ${}^1A_{1g} \rightarrow {}^3A_{2u}$  0-0 in  $\text{Rh}(\text{t-butNC})_4^+$  represents the energy of the  ${}^1A_{1g}$  state relative to the  ${}^3A_{2u}$  state for dimers at infinite metal-metal separation. Because the bond energy for the excited state is known from the Birge-Sponer extrapolation, the ground state bond energy,  $D_0^{\text{gs}}$ , can be calculated to be  $D_0^{\text{gs}} = ({}^1A_{1g} \rightarrow {}^3A_{2u})^{\text{d}} + D_0^{\text{ex}} - ({}^1A_{1g} \rightarrow {}^3A_{2u})^{\text{m}}$ . The 0-0 for the monomer is located at 460 nm (62 kcal/mole). Combining the dimer value at 751.5 nm (38 kcal/mole) and the 42 kcal/mole from the

Figure 14. Idealized overall potential surfaces relating the monomer and dimer  ${}^1A_{1g} \rightarrow {}^3A_{2u}$  transition energies to monomer and dimer bond energies.

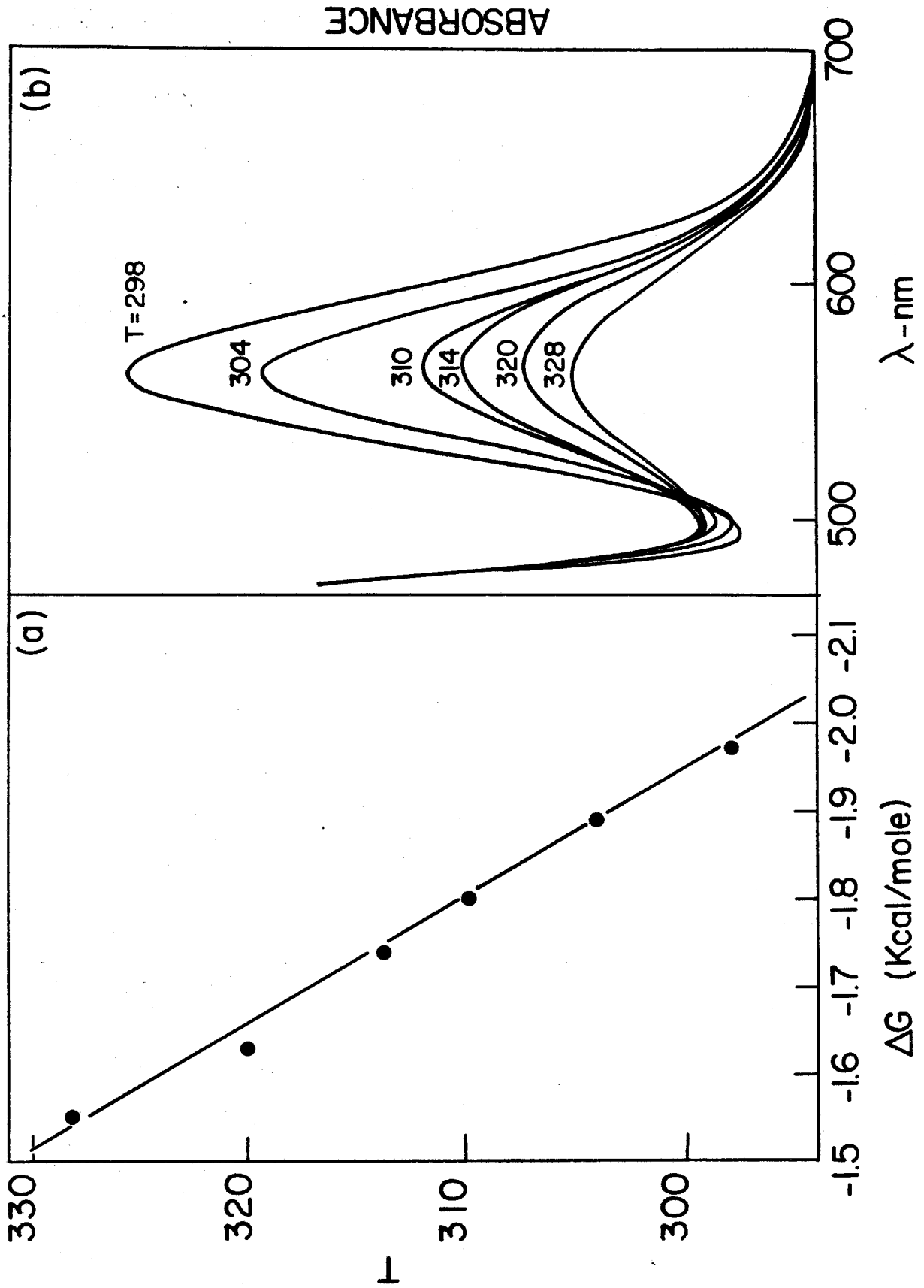


extrapolation produces a ground state value of 18 kcal/mole. This shows a weak albeit significant bonding energy for the ground state.

Another way of obtaining a thermodynamic value related to the metal-metal interaction is to simply measure the equilibrium constant for the dimerization of two monomers at various temperatures. This produces a  $\Delta H$  and  $\Delta S$  for dimerization through the well known relationship  $\Delta G(T) = -RT \ln K_{eq}(T) = \Delta H - T\Delta S$ .  $Rh(CNph)_4^+PF_6^-$  was chosen for this experiment. Mann et al.<sup>19</sup> determined the  $K_{eq}$  at 25°C enabling the temperature variation experiment to be calibrated to this known point. Figure 15 shows the points obtained in this experiment plotted to yield  $\Delta S = -15$  e.u. as the slope and  $\Delta H = -6.3$  kcal/mole.

There is a discrepancy between the 6.3 kcal/mole from the equilibrium measurements and the 18 kcal/mole from the spectroscopic extrapolation, because techniques used here are measuring fundamentally different quantities. The 6.3 kcal/mole takes into account solution effects associated with the acetonitrile partial coordination to the monomer; there are four axial positions on the two monomer ions and only two such sites on a dimer. The loss of these two bonds could account for as much as 5-10 kcal/mole, bringing the solution bond energy more in line with the spectroscopic value. Birge-Sponer extrapolations typically yield values that are high, raising the actual value to an extrapolated one of

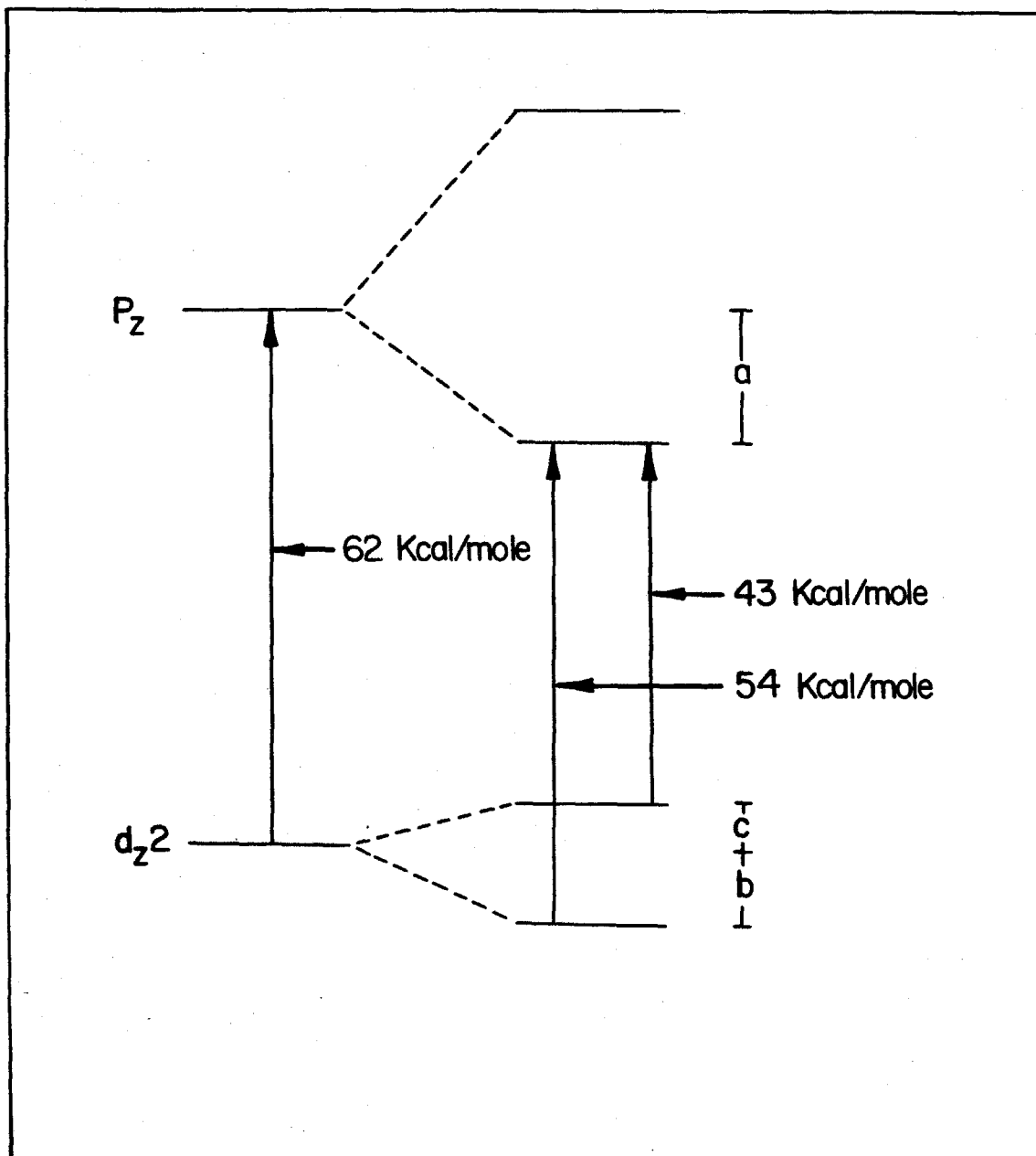
Figure 15. Plot of the  $\Delta G$  for dimerization *vs.* temperature for  $\text{Rh}(\text{CNph})_4^+$  in a 0.1 M  $(\text{n-butyl})_4\text{N}^+\text{PF}_6^-$  acetonitrile solution and spectra used to develop these points demonstrating the large change in dimer concentration, characteristic of the negative  $\Delta S$ .



18 kcal/mole. Within the errors involved it can be concluded that the ground state bond energy is less than 20 kcal/mole and probably closer to 10 kcal/mole; distinctly less than the excited state value.

We can now reconsider whether the stabilization of the  ${}^1A_{1g} \rightarrow {}^3A_{2u}$  transition is due to  $d_{z^2}\sigma^*$  destabilization or  $p_z\sigma$  stabilization. Using the known location of the  ${}^1A_{1g} \rightarrow {}^3A_{1g}$  in  $Rh_2(b)_4(Bph_4)_2$  and the ground state bond energy, the absolute stabilization of  $p_z\sigma$ ,  $d_{z^2}\sigma^*$ , and  $d_{z^2}\sigma$  can be determined. Figure 16 displays this calculation. The optical transitions observed are 62 kcal/mole, 43 kcal/mole, and 54 kcal/mole for  ${}^1A_{1g} \rightarrow {}^3A_{1g}$  (dimer) respectively. These values yield  $a-b = 8$  and  $a+c = 19$  for the orbital stabilization energies. A third equation  $(b-c) \times 2 = 18$  kcal/mole is obtained for two electrons in each of the  $d_{z^2}\sigma$  and  $d_{z^2}\sigma^*$  orbitals. These three simultaneous equations yield  $a = 18$  kcal/mole,  $b = 10$  kcal/mole and  $c = 1$  kcal/mole. If  $(b-c) \times 2 = 6.5$  kcal/mole taken from the equilibrium measurement is used, then  $a = 15.12$ ,  $b = 7.12$  and  $c = 3.88$ . The two extremes for the ground state bond energy result in the same trend for the  $p_z, \pi^*CNR$  and  $d_{z^2}$  set;  $p_z\sigma, \pi^*CNR$  is the most  $\sigma$  bonding of the three,  $d_{z^2}\sigma$  is also bonding but not as much as  $p_z, \pi^*CNR$  and  $d_{z^2}\sigma^*$  is only slightly antibonding. At a distance of  $3.24 \text{ \AA}$  this would be the expected trend. The  $5p_z\sigma$  overlap is probably quite large. The  $d_{z^2}$  orbital has little overlap

Figure 16. Molecular orbital diagram of the  $\sigma$  metal-metal manifold depicting the stabilization of the orbitals involved in the low lying excited states and ground state of  $\text{Rh}_2(\text{b})_4^{2+}$ .



itself but gains its stabilization from the interaction with  $5p_z\sigma$ , both of which have  $a_{1g}$  symmetry. It is this configurational interaction with a strongly bonding excited state that produces the net stabilization of a formally nonbonding configuration.

The excited state stretching frequency and distortion for the  ${}^3A_{1g}$  excited state is consistent with this result. Table 5 shows the energies of the progression in the 530 nm region. The average vibrational frequency is  $130\text{ cm}^{-1}$ . The Huang-Rhys factor which is representative of the distortion is about 4. The FCF's can be calculated for this band in the same way as the  ${}^1A_{1g} \rightarrow {}^3A_{2u}$  transition. In this case, however, it is difficult to extract the overall shape of the band due to the more intense absorptions obscuring all but the sharp structure. A calculation was done to determine the  $\Delta\xi$  for a transition with  $h\omega_{gr} = 85\text{ cm}^{-1}$ ,  $h\omega_{ex} = 130\text{ cm}^{-1}$ , and a band maximum occurring at about  $v = 4$ . A rough value for  $(\Delta\xi)^2$  is obtained with the diatomic approximation yielding  $|\Delta X| = .22\text{ \AA}$ . Because  $h\omega$  increases upon electronic excitation, the distortion is presumed to be a contraction yielding a  ${}^3A_{1g}$  excited state metal-metal bond distance of  $3.02\text{ \AA}$ . These three results, the relative  $p_z$  vs.  $d_{z^2}$  bonding character, vibrational frequency and distortion for the  ${}^3A_{1g}$  state serve as checks on the assignment of the 530 nm structure as  ${}^1A_{1g} \rightarrow {}^3A_{1g}$ .

TABLE 5

<u>V<sup>a</sup></u>	<u>E<sub>V</sub> (cm<sup>-1</sup>)</u>	<u>E<sub>V</sub>-E<sub>V-1</sub></u>
0	18484	
1	18612	128
2	18748	136
3	18879	131
4	19008	129
5	19139	131
6	19268	129
7	19402	134
8	19524	122
9	19646	120
10	19782	136

<sup>a</sup>The assigned  $a_{1g}$  (Rh-Rh) vibrational quantum number.

## Section 7

The description given above is quite satisfying in many respects. It shows the relationships between vibrational frequencies, transition energies, and metal metal bonding strength. This apparent self consistency makes the molecular orbital description very attractive. However, a simple picture such as this does not account for the locations of all the transitions in these dimers.

A very important consideration is related to the energy of the  ${}^1A_{1g} \rightarrow {}^1,{}^3E_u$  ( $d_{xz,yz} \rightarrow p_z, \pi^*CNR$ ) transition. In  $Rh_2(b)_4^{2+}$ , the energy of this transition is almost exactly the same as in monomeric  $Rh(CNR)_4^+$ . Independent of the extent of dimerization, this transition occurs at about 310 nm. Very little  $\pi$  bonding is present in this system, predicting a  ${}^1A_{1g} \rightarrow {}^1,{}^3E_u$  stabilization equal to that of the  $p_z$  orbital. According to Figure 16, this is about 15 kcal/mole or  $5000\text{ cm}^{-1}$  but only a few hundred wavenumbers stabilization is observed.

Two explanations are possible. The first and least palatable makes the assertion that the  ${}^1A_{1g} \rightarrow {}^1E_u$  transition is not  $d_{xz,yz} \rightarrow p_z, \pi^*CNR$  but should be assigned as  $d_{z^2\sigma^*} \rightarrow p_x, p_y, \pi^*CNR$ . Because  $d_{z^2\sigma^*}$  does not seem to be particularly destabilized by the metal-metal interaction, the assignment of the charge transfer state  ${}^1E_u$  in this way serves to retain the same position of the  ${}^1A_{1g} \rightarrow {}^1E_u$  transition in both the monomers and dimers.

This assignment goes against the understanding of  $d^8$  electronic structure that has been developed over the last 25 years. The  $d_{z^2}$  orbital has always been placed near the  $d_{xz,yz}$  and  $d_{xy}$  orbitals in these square planar complexes. In order for this new assignment to be correct, the  $d_{z^2}$  orbital would have to be at least  $20,000 \text{ cm}^{-1}$  above the  $d\pi$  set. This condition combined with analogies to other charge transfer spectra suggests that a reassignment of the  ${}^1E_u$  excited state is inappropriate.

The other possible explanation questions the validity of the one electron molecular orbital description. In this modified picture there are two types of transitions in the dimer. Some transitions involve electrons promoted from the  $d_{z^2} \sigma$  and  $\sigma^*$  orbitals resulting in excited states such as the  ${}^1A_{2u}$  which are delocalized over the entire dimer. Other excited states such as  ${}^1E_u$  correspond to single center excitations. The metal-metal bonding is not significantly affected in these states. Essentially, the energy of the  $p_z, \pi^* \text{CNR}$  orbital in the overall multielectron wavefunction is quite sensitive to the rest of the open shell.

This second explanation easily accounts for the energies of these various transitions. It is disappointing in the respect that it adds little to the theoretical understanding of the bonding in this system. By weakening the one electron description, we invoke terms that can certainly account for this stabilization discrepancy at the

expense of a quantitative orbital ordering. The values calculated previously for the relative bonding energy of the  $p_z\sigma, \pi^*CNR, d_{z^2}\sigma^*$  and  $d_{z^2}\sigma$  orbitals lose much of their meaning. The net splitting of the  $d_{z^2}\sigma$  and  $d_{z^2}\sigma^*$  orbitals is probably still valid since the energy difference is observed as the  ${}^3A_{2u}, {}^3A_{1g}$  splitting in the absorption spectrum. Because of the closed shell nature of the  ${}^1A_{1g}$  configuration, however, the absolute ground state orbital energies cannot be confidently employed.

Neither of these explanations is particularly attractive, due to the drawbacks mentioned above. The latter explanation is likely to be more appropriate, forcing the values obtained for the orbital energies to be viewed somewhat critically despite their consistency with the metal-metal force constants.

The occurrence of vibrational fine structure in the absorption spectrum of  $Rh_2(b)_4^{2+}$  allows for the calculation of excited state bond distances and bond energies. The most significant result from this detailed study involves the orbital character of the  $5p_z, \pi^*CNR$  orbital. In the monomeric  $d^8$  isocyanides the  ${}^1A_{1g} \rightarrow {}^1A_{2u}$  transition is predominantly charge transfer. The promotion of an electron from  $4d_{z^2}$  to  $5p_z, \pi^*CNR$  corresponds to moving electron density from an orbital that is mostly metal  $4d$  to one that is isocyanide  $\pi$  antibonding. The state distorts along M-CN and C≡N coordinates. In the dimer the

data suggest the lowest  ${}^1A_{2u}$  state is dominated by the  $p_z - \bar{p}_z$  interaction. This orbital has a great deal of  $\sigma$  bonding character. It lies to higher energy than  $4d_{z^2}\sigma^*$  in spite of its increased bonding interaction not because it destabilizes other bonds but because its energy is determined by the  $n=5$  character of its atomic orbital parentage. The dimers therefore do not have a low lying  ${}^1A_{1g} \rightarrow {}^1A_{2u}$  metal to ligand charge transfer transition. This charge transfer transition is moved to higher energy through configurational interaction with the lower metal localized  ${}^1A_{2u}$  state. The broad  ${}^1A_{2u}$  state seen in these dimers is an example of a new and unique type of transition metal complex absorption band identified as  $\sigma^* \rightarrow \sigma$ . It is characterized by a decrease in the metal-metal bond length and an increase in the internuclear vibrational force constant corresponding to a change in formal bond order from zero to one.

CHAPTER 3

Luminescence and Photophysics of  
Rhodium(I) Diisocyanides

## Section 1

The fluorescence spectrum of  $\text{Rh}_2(\text{b})_4^{2+}$  was reported in 1978.<sup>26</sup> There is an intense emission band located directly to lower energy from the  $^1\text{A}_{1g} \rightarrow ^1\text{A}_{2u}$  absorption band. The quantum yield was determined to be  $\phi = .05$  along with the lifetime placed at less than 2 nsec. The dimer  $[\text{Rh}(\text{CNph})_4]_2^{2+}$  and other rhodium(I) diisocyanides all show similar behavior.

Miskowski<sup>26</sup> determined through flash photolysis techniques that there was a transient, presumably the  $^3\text{A}_{2u}$  excited state, having a lifetime of 8.3  $\mu\text{sec}$ . Subsequently Milder<sup>27</sup> was successful in quenching this excited state with electron transfer reagents possessing sufficiently high oxidation or reduction potentials. Because of the obvious usefulness of a long lived excited state with high oxidation and reduction potentials, a study was undertaken to find the corresponding phosphorescence associated with  $^3\text{A}_{2u} \rightarrow ^1\text{A}_{1g}$  radiative transitions.

Using a Perkin Elmer PMF-3 fluorimeter capable of detecting only very intense luminescence at 800 nm, it was noticed that the baseline seemed to show a reproducible deviation in this region.  $\text{Rh}_2(\text{TMB})_4^{2+}$  examined at low temperature (77K) displayed a distinct emission band at 740 nm in addition to its fluorescence band at 620 nm. The excitation spectrum demonstrated that this band was

indeed due to  $\text{Rh}_2(\text{TMB})_4^{2+}$  and not a result of an impurity. At ambient temperature  $\text{Rh}_2(\text{TMB})_4^{2+}$  does not show a well defined phosphorescence.

Figures 17a and 17b show the emission spectra of  $\text{Rh}_2(\text{TMB})_4^{2+}$  and  $\text{Rh}_2(\text{b})_4^{2+}$  at 77K and 300K with excitation into the  ${}^1\text{A}_{1g} \rightarrow {}^1\text{A}_{2u}$  absorption band. Figure 17c shows the emission spectrum of  $\text{Rh}_2(\text{DMB})_4^{2+}$  under these conditions. Clearly, the lower energy emission band in both  $\text{Rh}_2(\text{TMB})_4^{2+}$  and  $\text{Rh}_2(\text{DMB})_4^{2+}$  has a very temperature dependent quantum yield. The behavior of this band is independent of the state of aggregation or solvent viscosity. Similar temperature sensitivity is seen in the  $[\text{Rh}(\text{CNR})_4]_2^{2+}$  dimers.  $\text{Rh}_2(\text{DMB})_4^{2+}$  shows a temperature sensitivity in its fluorescence as well.  $\text{Rh}_2(\text{b})_4^{2+}$  seems to be somewhat different from all these other dimers, displaying only a small dependence on temperature.

This low energy emission band is assigned as phosphorescence from the  ${}^3\text{A}_{2u}$  excited state to the ground state. The apparent origin of the emission overlaps neatly with the low energy tail of the  ${}^3\text{A}_{2u}$  absorption in  $\text{Rh}_2(\text{b})_4^{2+}$ ,  $\text{Rh}_2(\text{TMB})_4^{2+}$  and other dimers. The low temperature lifetime of these molecules ranges from 8  $\mu\text{sec}$  to 20  $\mu\text{sec}$ . In  $\text{Rh}_2(\text{b})_4^{2+}$  the lifetime is exactly the same as the 8.3  $\mu\text{sec}$  observed in the transient absorption spectrum identifying the photoactive electron transfer state as the  ${}^3\text{A}_{2u}, d_z^2 \rightarrow p_z, \pi^*\text{CNR}$ .

It seemed puzzling that molecules so similar as  $\text{Rh}_2(\text{b})_4^{2+}$  and  $\text{Rh}_2(\text{TMB})_4^{2+}$  would have such dramatically different luminescence properties. Temperature dependence similar to that of  $\text{Rh}_2(\text{TMB})_4^{2+}$  has been reported by Gray<sup>17</sup> and studied in detail by Andrews for rhodium and iridium chelated diphosphines.<sup>16</sup> It was noted that there is a sensitivity to solvent viscosity in these monomers.

Conclusions were drawn by Andrews suggesting a distortion in the  $^3\text{A}_{2\text{u}}$  excited state that allows for rapid nonradiative decay of the excited state, reducing the quantum yield and shortening the observed excited state lifetime. This behavior in  $\text{d}^8$  dimers and  $\text{d}^8$  monomers is quite different from that seen in photophysical studies done to date on organic compounds. The interest in the chemical physics community regarding nonradiative decay mechanisms and the photochemical value of understanding the subtle ligand controlled effects present in these  $\text{d}^8$  systems prodded an attempt to analyze these data in a way which would be consistent with a general theoretical framework.

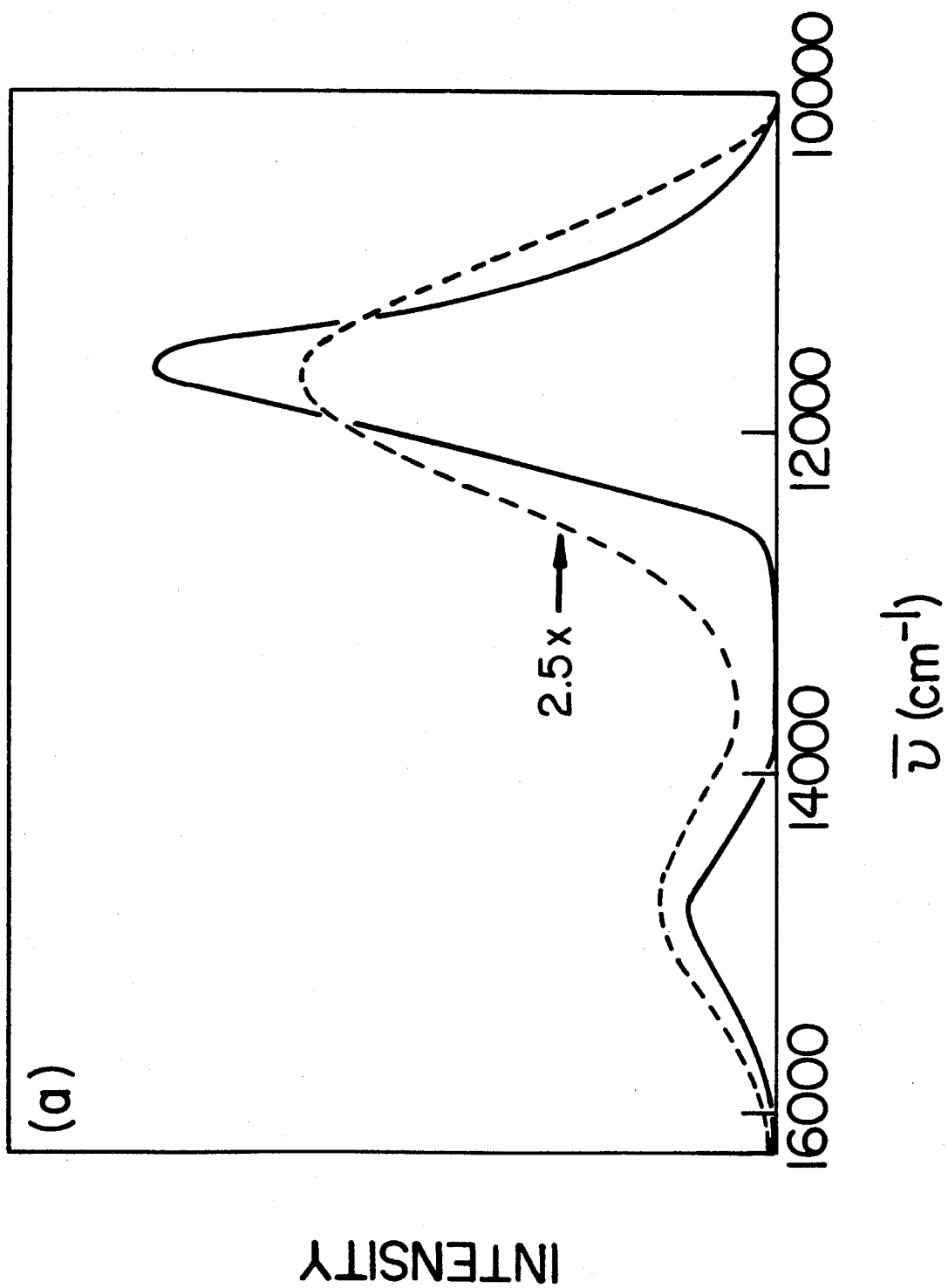
The lifetimes and some quantum yields at 77K and 300K are listed in Table 6. The quantum yields reflect the excited state lifetime through the relationship

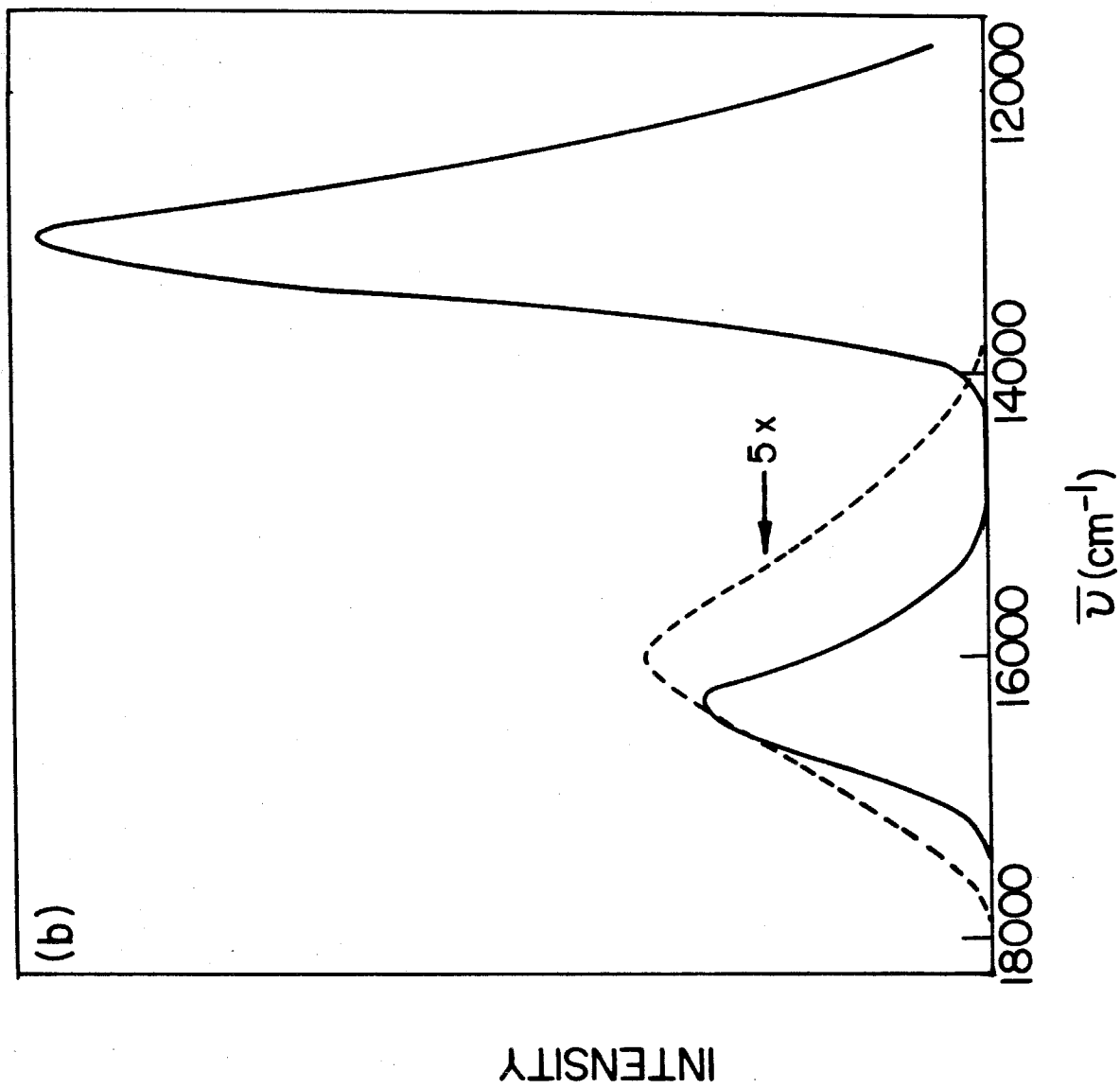
$$\phi = \frac{k_{\text{rad}}}{k_{\text{rad}} + k_{\text{nr}}} = \frac{k_{\text{rad}}}{k_{\text{obs}}}. \quad \text{Because } \tau = \frac{1}{k_{\text{obs}}} \text{ it appears that } k_{\text{nr}}$$

is changing a great deal over this temperature range. The luminescent lifetimes were measured at a number of temperatures in various solvents. All solvents gave essentially the same

Figure 17. 300K (dashed line) and 77K (solid line) emission spectra in 2 methyl-THF/acetonitrile of:

a)  $\text{Rh}_2(\text{b})_4^{2+}$ , b)  $\text{Rh}_2(\text{TMB})_4^{2+}$ , c)  $\text{Rh}_2(\text{DMB})_4^{2+}$ .





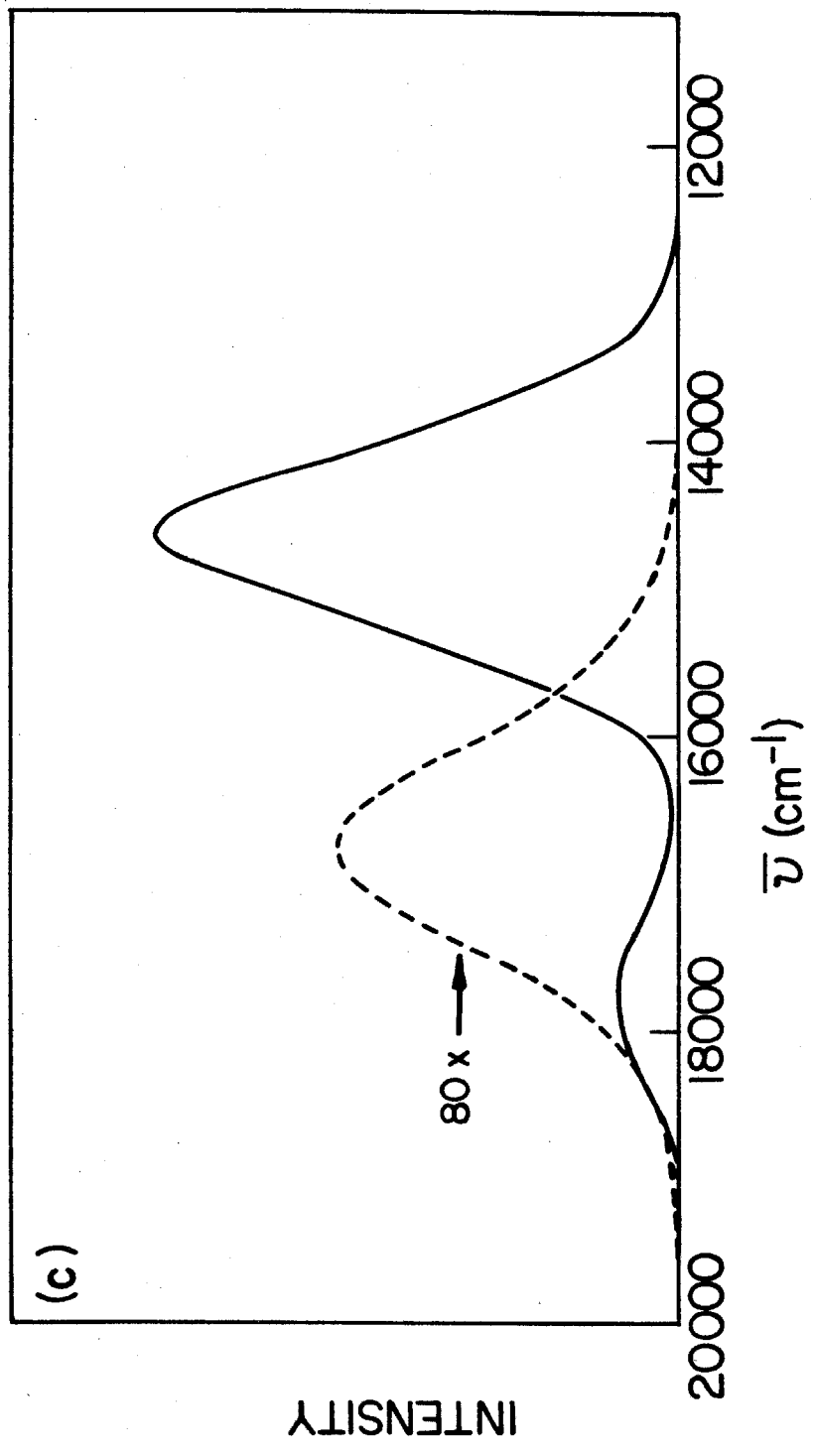


TABLE 6

Sample	$\tau_{300}^p$ $\mu\text{sec}$	$\tau_{77}^p$ $\mu\text{sec}$	$\phi_{300}^{fb}$	$\phi_{77}^{fa}$	$\phi_{300}^{pb}$	$\phi_{77}^{pa}$
$\text{Rh}_2(\text{b})_4^{2+}$ in 2Me-THF/ $\text{CH}_3\text{CN}$	8.3	12.5	.07	.08	.32	.64
$\text{Rh}_2(\text{TMB})_4^{2+}$ in 2Me-THF/ $\text{CH}_3\text{CN}$	0.34	20.5	.055	.15	-	.51
$\text{Rh}_2(\text{DMB})_4^{2+}$ in 2Me-THF/ $\text{CH}_3\text{CN}$	<.01	21.0	.0016	.016	-	.17
$[\text{Rh}(\text{phNC})_4]_2(\text{Bph}_4)_2$	.285	14.9	-	-	-	-
$\text{Rh}_2(\text{TMB})_4(\text{PF}_6)_2$	.076	20.4	-	-	-	-

<sup>a</sup>Low temperature error is  $\pm 15\%$  due to errors in correcting for absorbance changes.

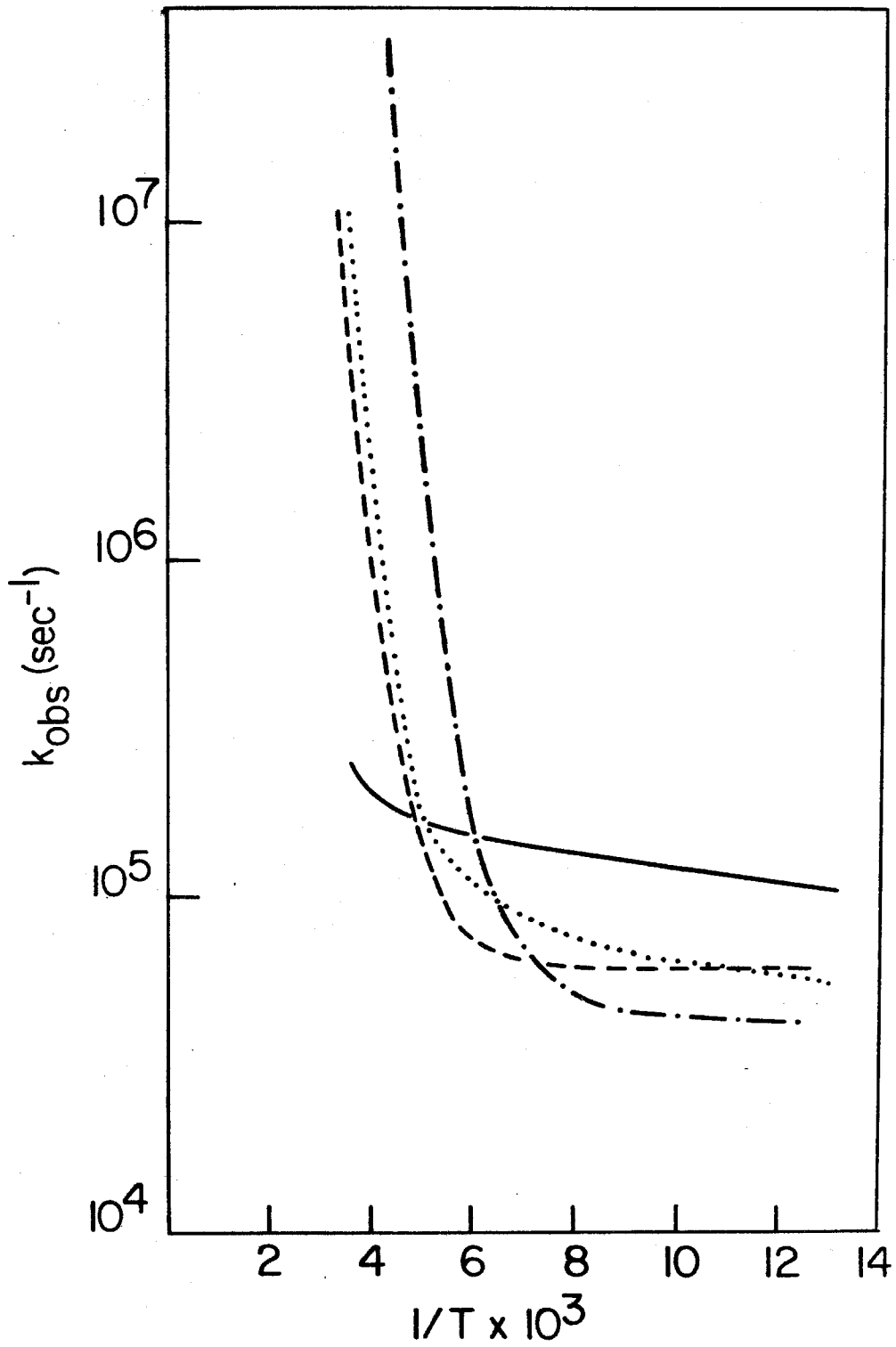
<sup>b</sup>Ambient temperature error is  $\pm 5\%$

behavior. Figure 18 plots these data for  $k_{\text{obs}}$  vs.  $1/T$ .  $k_{\text{obs}}$  is representing predominantly  $k_{\text{nr}}$  for these systems because  $\phi < .1$  at high temperatures. Figure 18 shows that these data could be represented to a first approximation as  $k_{\text{nr}} = k_0 + k_1 e^{-E_a/kT}$ , suggesting also a temperature independent contribution to the nonradiative decay. The temperature dependent part consists of an activation energy  $E_a$ , and a preexponential factor  $k_1$ . This simple Arrhenius behavior tempts the experimenter to view the nonradiative decay process as a simple activated first order "reaction".

## Section 2

The topic of nonradiative transitions has enjoyed a large portion of the experimental and theoretical efforts of chemical physicists in the past fifteen years.<sup>8,9</sup> Numerous papers have been published, characterized by elegant mathematical techniques and experimental genius. Unfortunately, the experimental work has focused primarily on organic systems. Although the models developed by theoreticians place few restrictions on molecular structure, the experimental work has tested only parts of the general theory of nonradiative relaxation. An examination of the treatment of Englman and Jortner<sup>49</sup> shows that much of the behavior seen in these inorganic systems is predicted by the theoretically derived strong coupling limit.

Figure 18. Arrhenius plot ( $\log k$  vs.  $1/T$ ) of the  ${}^3A_{2u}$  lifetime ( $\tau = 1/k$ ) of  $Rh_2(b)_4^{2+}$  (solid line),  $Rh_2(TMB)_4^{2+}$  (dashed line),  $[Rh(\text{cyclohexNC})_4]_2^{2+}$  (dotted line), and  $Rh_2(DMB)_4^{2+}$  (dot-dash line).



The generating function method allows for the comparison of various coupling limits within the description of a single initial state undergoing a nonradiative transition to a dense quasicontinuum of final states. One particularly useful aspect of this method is that the criterion involved in choosing the appropriate theoretical limits rests on the relative geometries of the initial and final states. The choice of limit, either strong or weak coupling, is determined by the size of the parameter

$$G = 1/2 \sum_j \Delta_j^2 (2\bar{n}_j + 1)$$

where  $\Delta_j$  is the distortion between the potential surfaces of the two states along the vibrational coordinate  $j$  and  $\bar{n}_j$  is representative of the average vibrational quantum number in vibrational mode  $j$  at a given temperature.

Englman and Jortner go on to make the approximation of an average vibrational frequency,  $\hbar\langle\omega\rangle$ , in order to eliminate the summation over the  $j$  modes yielding

$$G \approx \frac{E_m}{\hbar\langle\omega\rangle} \coth\left(\frac{\hbar\langle\omega\rangle}{2kT}\right)$$

where  $E_m$  is about half the Stoke's Shift between these states. The overall expression for the nonradiative transition probability is derived to be

$$W = \frac{C^2}{h} \exp(-G) \int_{-\infty}^{\infty} \exp\left(\frac{i \Delta E t}{h}\right) + G_+(t) + G_-(t) dt$$

where  $C$  is a vibronic matrix element connecting the two electronic states,  $\Delta E$  is the energy separating the minima of the two potential surfaces and

$$G_+(t) = \frac{1}{2} \sum_j |\Delta_j|^2 (\bar{n}_j + 1) \exp(i\omega_j t)$$

$$G_-(t) = \frac{1}{2} \sum_j |\Delta_j|^2 \bar{n}_j \exp(-i\omega_j t) .$$

The two limits, strong and weak coupling, are two extremes chosen to enable an analytical expression for the integral in  $W$ . Avoiding the intermediate steps, the result for strong coupling (when  $G \gg 1$ ) is

$$W_{sc} = \frac{C^2 \sqrt{2\pi}}{\hbar (E_m k T^*)^{1/2}} \exp\left(\frac{-E_a}{k T^*}\right)$$

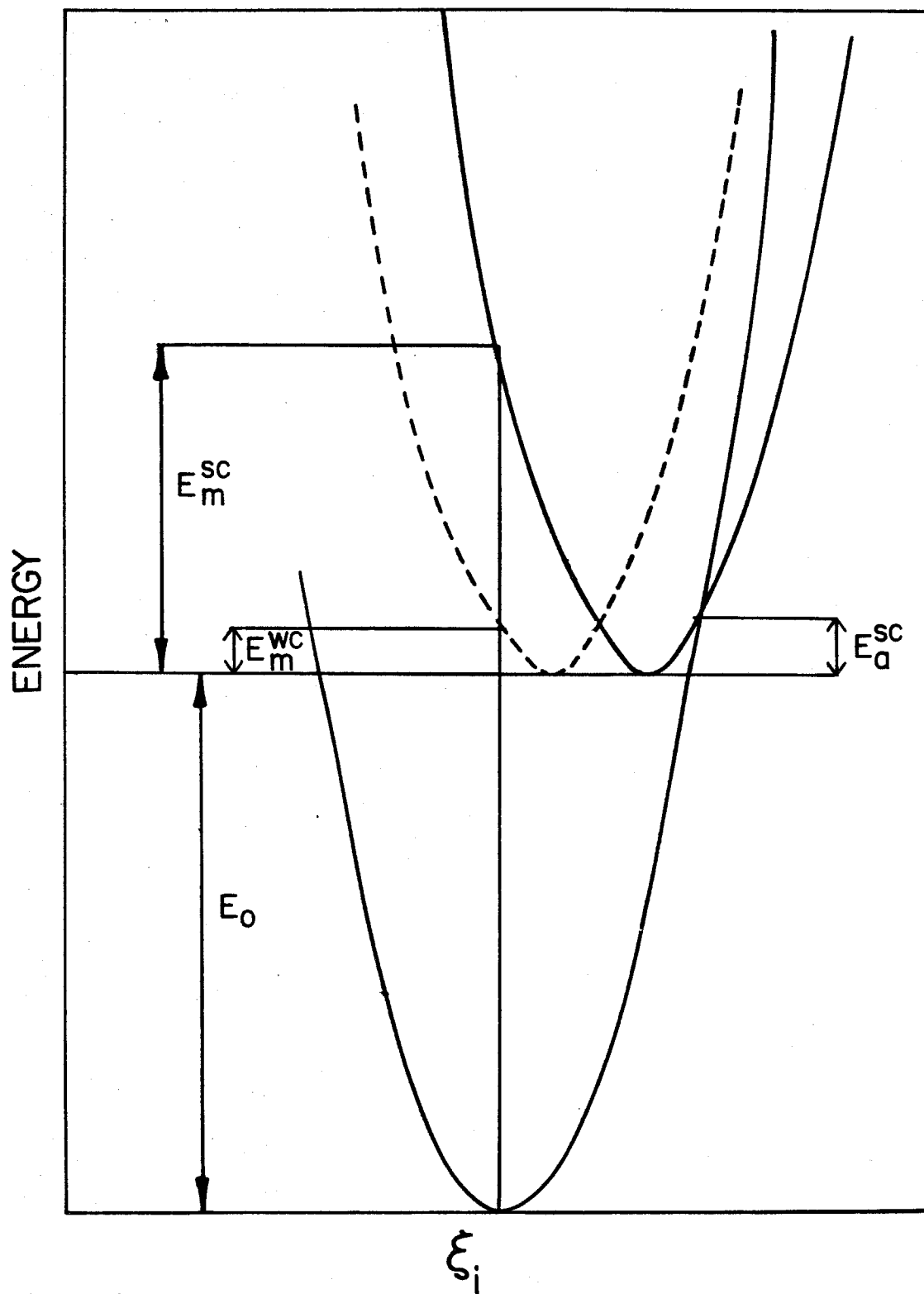
where

$$T^* = 1/2 \frac{\hbar \langle \omega \rangle}{k} \coth\left(\frac{\hbar \langle \omega \rangle}{2kT}\right)$$

and  $E_a$  is the minimum energy of intersection of the two hypercurves defined by the two states in a Born-Oppenheimer description as shown in Figure 19. The result for weak coupling (when  $G \ll 1$ ) is

$$W_{wc} = \frac{C^2}{\hbar} \sqrt{\frac{2\pi}{\hbar \omega_M \Delta E}} \exp(-1/2 \sum_j \Delta_j^2 (2\bar{n}_j + 1)) \times \\ \exp\left(-\frac{\Delta E}{\hbar \omega_M} \log\left(\frac{2\Delta E}{\sum_j \hbar \omega_M \Delta_j^2 (\bar{n}_j + 1)}\right) - 1\right)$$

Figure 19. Representative potential surfaces depicting the conditions for weak coupling (dashed line) and strong coupling (solid line).



where the subscript M refers to only the highest energy molecular vibrations, provided  $(\Delta_M)^2 \neq 0$  (although  $\Delta_M$  need not be large). In spite of the  $\bar{n}_j$ 's in the first exponential, the weak coupling rate is a slowly varying function of T. In the strong coupling limit, however, provided  $kT \geq \hbar\langle\omega\rangle$ , the temperature in the exponential dominates the overall rate.

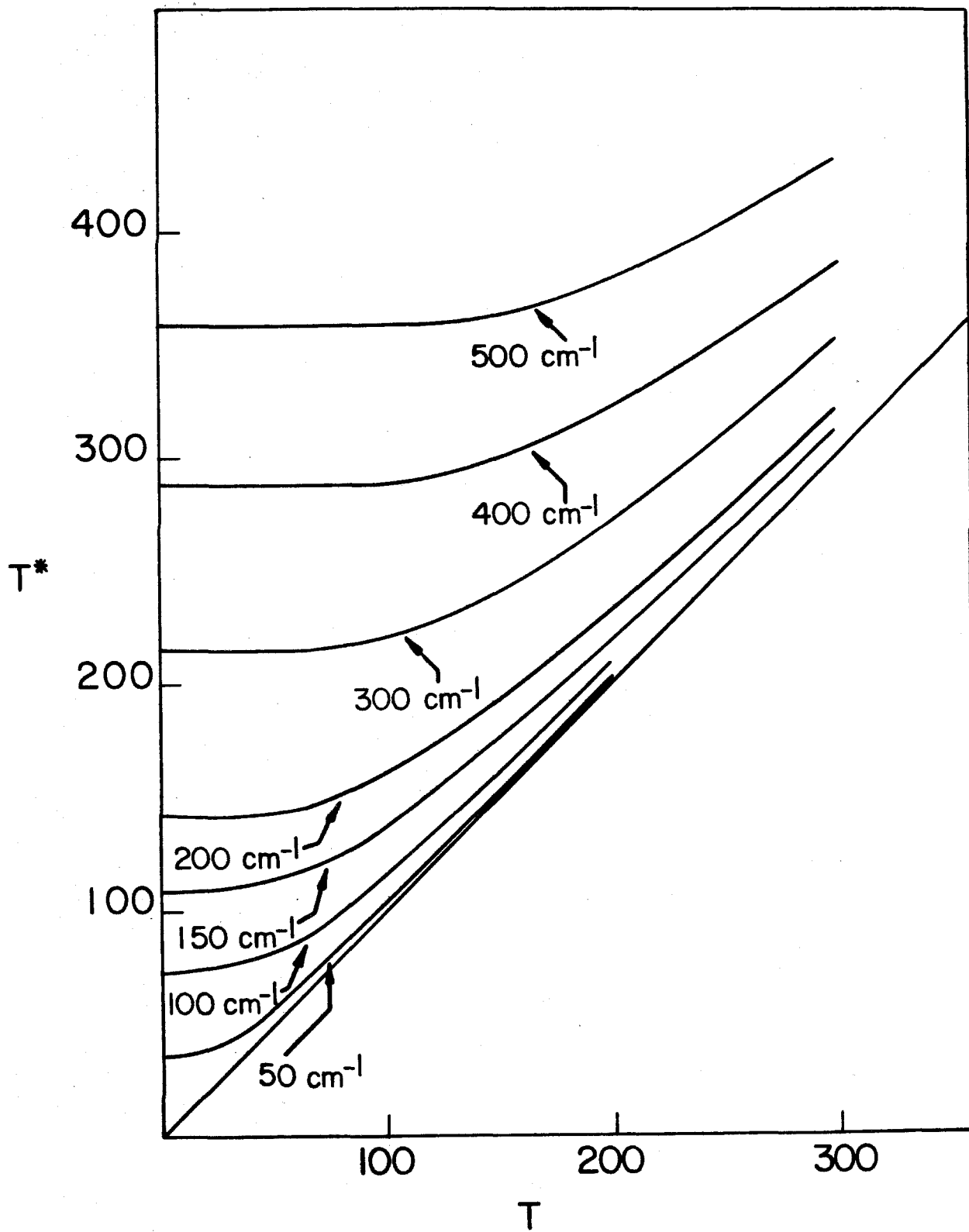
This striking contrast in the temperature dependence marks the most important experimental observable distinguishing these two limits. The data for  $\text{Rh}_2(\text{TMB})_4^{2+}$ ,  $\text{Rh}_2(\text{DMB})_4^{2+}$ , and  $[\text{Rh}(\text{CNR})_4]_2^{2+}$  appear to be indicative of this strong coupling limit at high temperature.

The two temperature limits within the strong coupling rate equation deserve some additional attention. Because the temperature in the final result for  $W_{\text{SC}}$  is an effective temperature determined by the energy of  $\hbar\langle\omega\rangle$ ,  $T^*$  does not tend to zero as T approaches zero but achieves a value of  $\hbar\langle\omega\rangle/2k$ . Examples of the  $T^*$  dependence for various  $\hbar\langle\omega\rangle$ 's are shown in Figure 20. When  $\hbar\langle\omega\rangle \leq kT$  we expect to see Arrhenius behavior, but at low temperature  $T^*$  is a constant as a function of T so the nonradiative rate should be temperature independent. These two limits are given by

$$W_{\text{LT}}^{\text{SC}} = \frac{C^2 \sqrt{4\pi}}{\sqrt{E_m} \hbar\langle\omega\rangle} \exp\left(\frac{-2E_a}{\hbar\langle\omega\rangle}\right)$$

and

Figure 20. Plot of  $T^*(\bar{n}\langle\omega\rangle, T)$  vs.  $T$ .



$$W_{HT}^{SC} = \frac{C^2 \sqrt{2\pi}}{\hbar \sqrt{E_m} kT} \exp\left(\frac{-E_a}{kT}\right)$$

The role of the mean vibrational frequency  $\langle\omega\rangle$  should be clarified. Englman and Jortner express it as  $\langle\omega\rangle = N^{-1} \sum_j \omega_j$ . It enters the rate expression through the approximation

$$G = \frac{1}{2} \sum_j |\Delta_j|^2 (2\bar{n}_j + 1) \approx \frac{E_m}{\hbar \langle\omega\rangle} \coth\left(\frac{\hbar \langle\omega\rangle}{2kT}\right)$$

where  $E_m = 1/2 \sum_j \hbar \omega_j \Delta_j^2$ . In a case where  $\Delta_j = 0$  for all but  $j = i$  and  $\Delta_i$  is large, there is no need for an approximation and

$$G = \frac{1}{2} \Delta_i^2 \coth\left(\frac{\hbar \omega_i}{2kT}\right).$$

If there is only one mode (or several) where a large distortion between the two potential surfaces is present,  $\hbar \langle\omega\rangle$  will reflect an average of only these modes which have a significant  $\Delta_j$ .

Inorganic compounds in general have many states that are distorted ( $\hbar \omega_j \ll E_{mj}$ ) to a large degree relative to a nearby state. The condition required to meet the high temperature range of this limit is whether  $kT > \hbar \langle\omega\rangle$ . It has already been shown that there are low energy distorting modes present in these systems. When the temperature is high enough for this condition to be met for a given  $\hbar \langle\omega\rangle$ ,

$\frac{d \log W}{d \beta}$  will be close to a constant characteristic of the activation energy  $E_a$ .

### Section 3

The activation energy,  $E_a$ , is seen as the slope of  $k_{nr}$  when plotted vs.  $1/T$ . Figure 18 shows these data in which all the dimers except  $Rh_2(b)_4^{2+}$  exhibit this slope. Table 7 shows the  $E_a$  values extracted for these compounds when analyzed in this fashion. In all cases the  $E_a$  appears to be about  $3000 \text{ cm}^{-1}$ . This  $3000 \text{ cm}^{-1}$  is the activation energy needed to get to the crossing of the potential surface in the diagram in Figure 19.

The geometry of the  ${}^3A_{2u}$  state is well understood from the previous chapter. The distortion and vibrational frequencies for the  ${}^3A_{2u}$  and  ${}^1A_{1g}$  states are very similar in  $Rh_2(b)_4^{2+}$  and  $Rh_2(TMB)_4^{2+}$  for the respective  ${}^3A_{2u}$  states based on the energies and bandshapes of the  ${}^1A_{1g} \rightarrow {}^3A_{2u}$  transition. The  ${}^3A_{2u}$  state is highly distorted from the  ${}^1A_{1g}$  state along the internuclear coordinate; sufficiently distorted to meet the strong coupling requirement  $\hbar\omega \ll E_m$ . Because these states have the same relative geometry in both  $Rh_2(b)_4^{2+}$  and  $Rh_2(TMB)_4^{2+}$ , but their nonradiative behavior is so different, it is likely that the rate determining step in the nonradiative decay is not a direct step to the ground state.

Where does the excitation travel before it ends as vibrations in the  ${}^1A_{1g}$  ground state, crystal phonons, or solvent librations? A consideration of the other excited states near to the  ${}^3A_{2u}$  excited state provides an answer.

A metal localized ligand field transition,  $d_{z^2} \rightarrow d_{x^2-y^2}$ , is presumed to be located in the vicinity of the  $d_{z^2} \rightarrow p_z$  transition in  $d^8$  monomers. In  $Ni(CN)_4^{2-}$  it is assigned as the lowest lying singlet excited state. Ballhausen et al.<sup>50</sup> have suggested that this state is unstable in a  $D_{4h}$  geometry relative to tetrahedral geometry; an electron in the  $d_{x^2-y^2}$  will exert a force on the ligands pushing them away from being oriented along the x and y directions. An explanation based on this distortion was offered by Andrews for the nonradiative decay rates in  $d^8$  phosphines.

The dimers do not exhibit the solvent dependence associated with the monomers, but they do appear to have a distinct "ligand rigidity" sensitivity. 1,3 diisocyanopropane as a ligand keeps the rhodium dimer close to  $D_{4h}$  geometry, but TMB allows the dimer to undergo conformational changes.<sup>51</sup> Because of the less rigid nature of TMB, DMB, and pairs of monodentate ligands, this  $D_{2d}$  distortion (the correlating symmetry between  $D_{4h}$  and  $T_d$ ) is likely to be much more facile for flexible ligand "cages". The rigidity of "bridge" prohibits this distortion.

The nonradiative intramolecular pathway can be viewed as an activation to the crossing of the  ${}^3A_{2u}$  state with a  ${}^3B_{2u}$  state associated with the  $d_{z^2} \rightarrow d_{x^2-y^2}$  transition. The energy separation at the geometry of the surface crossing between these two states corresponds to a  $p_z, \pi^* - d_{x^2-y^2}$  splitting of about  $3000 \text{ cm}^{-1}$ .

The activation to this state is strongly supported by the results for  $\text{Ir}_2(\text{TMB})_4^{2+}$ . The absorption spectrum of this complex is similar in many ways to  $\text{Rh}_2(\text{TMB})_4^{2+}$  with respect to the  $d_{z^2} \rightarrow p_z$  transitions. However,  $\text{Ir}_2(\text{TMB})_4^{2+}$  has a  ${}^3A_{2u}$  excited state lifetime of 200 nsec at both 300K and 77K. The  $d_{z^2} \rightarrow d_{x^2-y^2}$   ${}^3B_{2u}$  state will be much higher in energy relative to the  ${}^3A_{2u}$  in this third row complex because ligand field splittings are invariably much greater in the third row than in the second row. The  $E_a$  from  ${}^3A_{2u}$  to  ${}^3B_{2u}$  will be much larger, in spite of the same relative equilibrium geometries for this iridium compound resulting in no temperature dependence in the  ${}^3A_{2u}$  lifetime over the accessible temperature range.

There are two extreme ways in which the Arrhenius behavior can be viewed in terms of the adiabatic potential surfaces. Figure 21a and 21b show these two extremes comparing  $\text{Rh}_2(\text{b})_4^{2+}$  and  $\text{Rh}_2(\text{TMB})_4^{2+}$ . Figure 21a displays the limit that the  $E_a$  for  $\text{Rh}_2(\text{b})_4^{2+}$  is much higher than that of  $\text{Rh}_2(\text{TMB})_4^{2+}$ , because the ligand's influence serves to raise the electronic energy of the minimum of the  ${}^3B_{2u}$  state.

The  ${}^3B_{2u}$  cannot distort to the same minimum that can be obtained with TMB. Figure 23b shows the alternative extreme. The  $E_a$  for  $Rh_2(TMB)_4^{2+}$  and  $Rh_2(b)_4^{2+}$  is the same but the flexibility of the TMB ligand is represented as a broader well, resulting in a crossing point at the same  $E_a$  but at a different geometry. Figure 21c is a combination of these two effects. Because flexibility, electronic energy and force constants are intimately related, this intermediate description is the most likely situation.

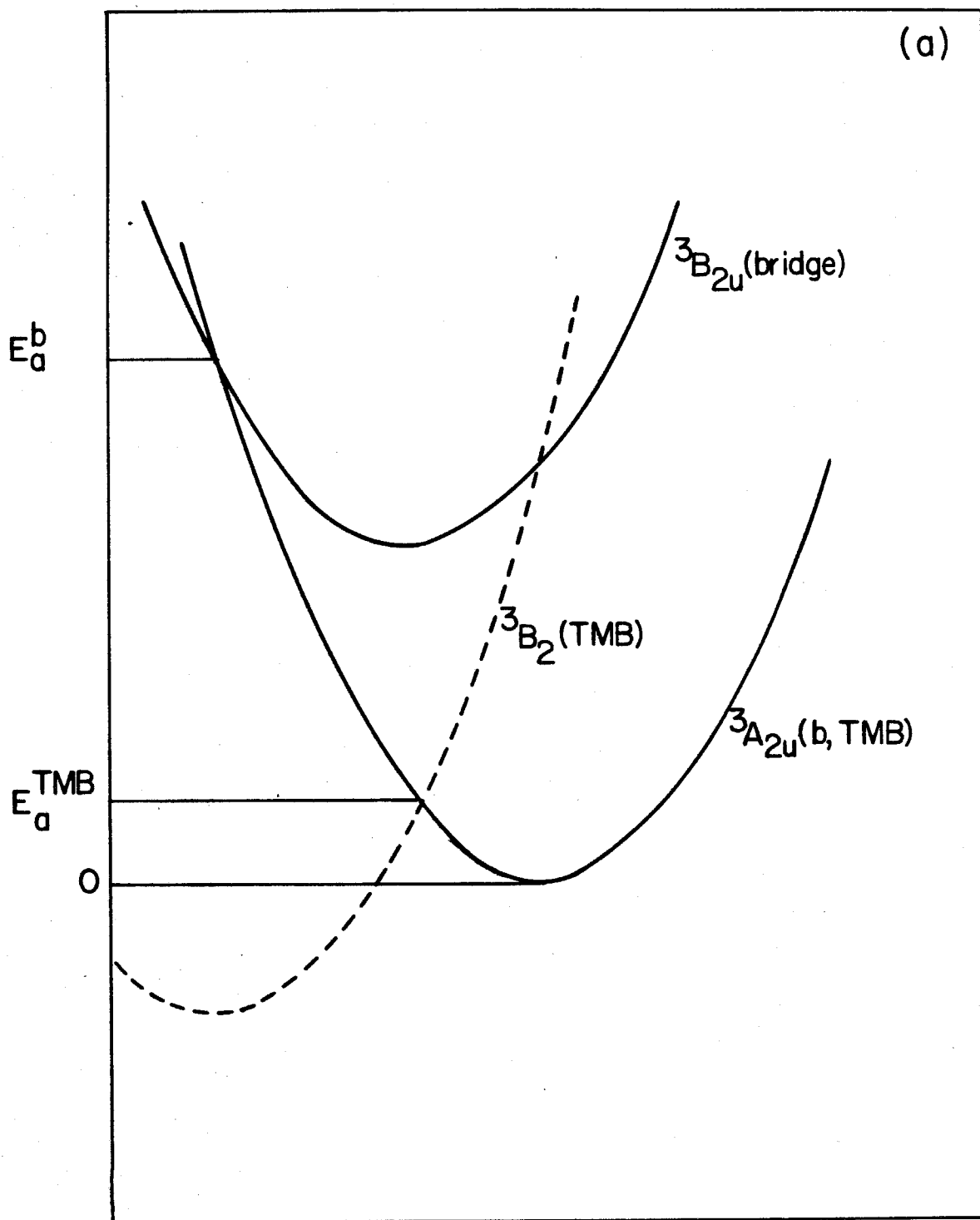
This effective frequency,  $\langle \omega \rangle$ , can be estimated from the position at which the  $k_{obs}$  begins to deviate from its low temperature value. Comparing  $Rh_2(DMB)_4^{2+}$ ,  $Rh_2(TMB)_4^{2+}$ , and  $Rh_2(b)_4^{2+}$ , the data yield values of 110K, 175K, and 250K respectively. By examining Figure 20, these temperatures at which  $T^*$  deviates from its low temperature value correlate to average effective frequencies of  $250\text{ cm}^{-1}$ ,  $500\text{ cm}^{-1}$ , and  $800\text{ cm}^{-1}$ .

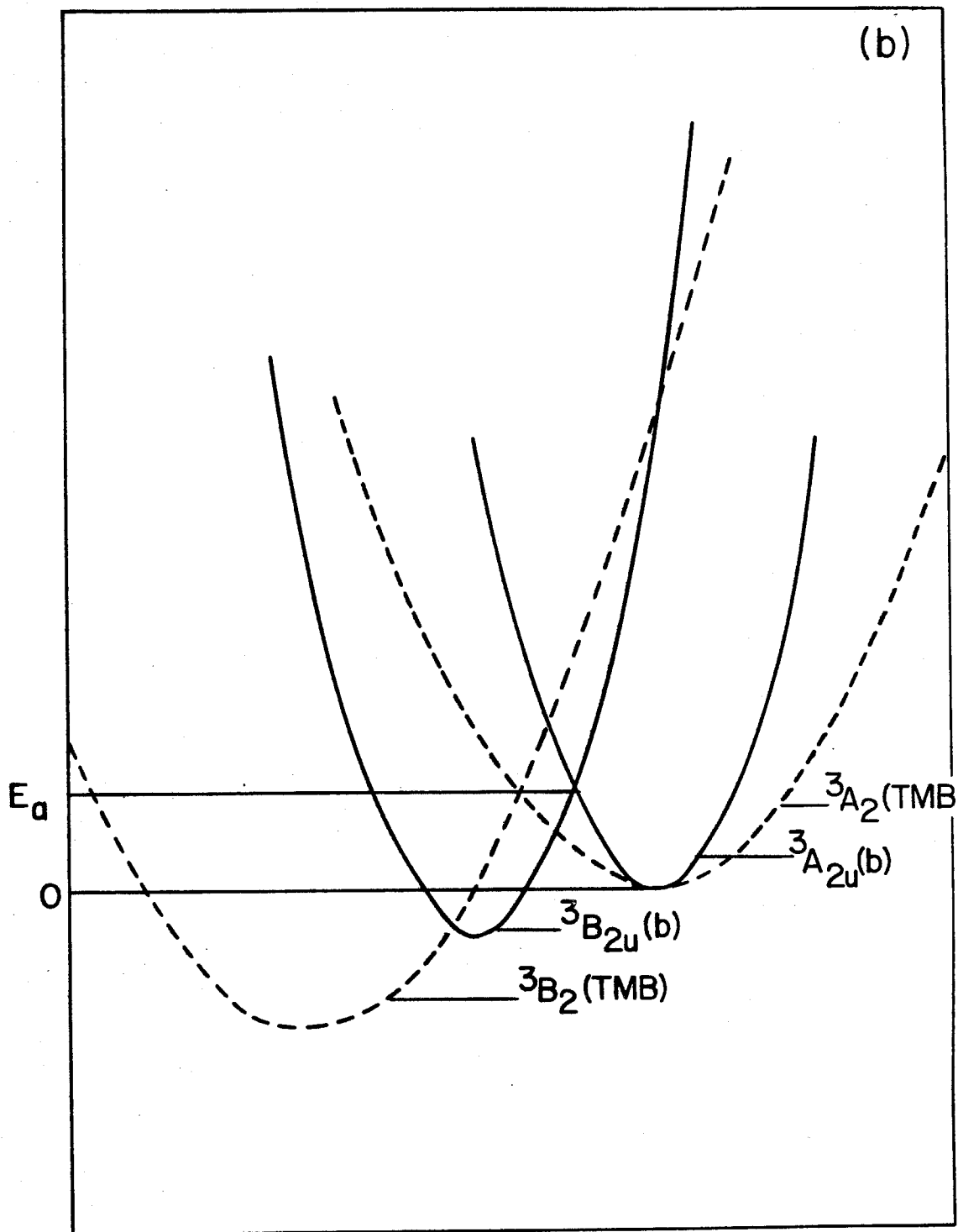
The plot of  $\log k_{obs}$  vs.  $\frac{1}{T}$  gives a slope of

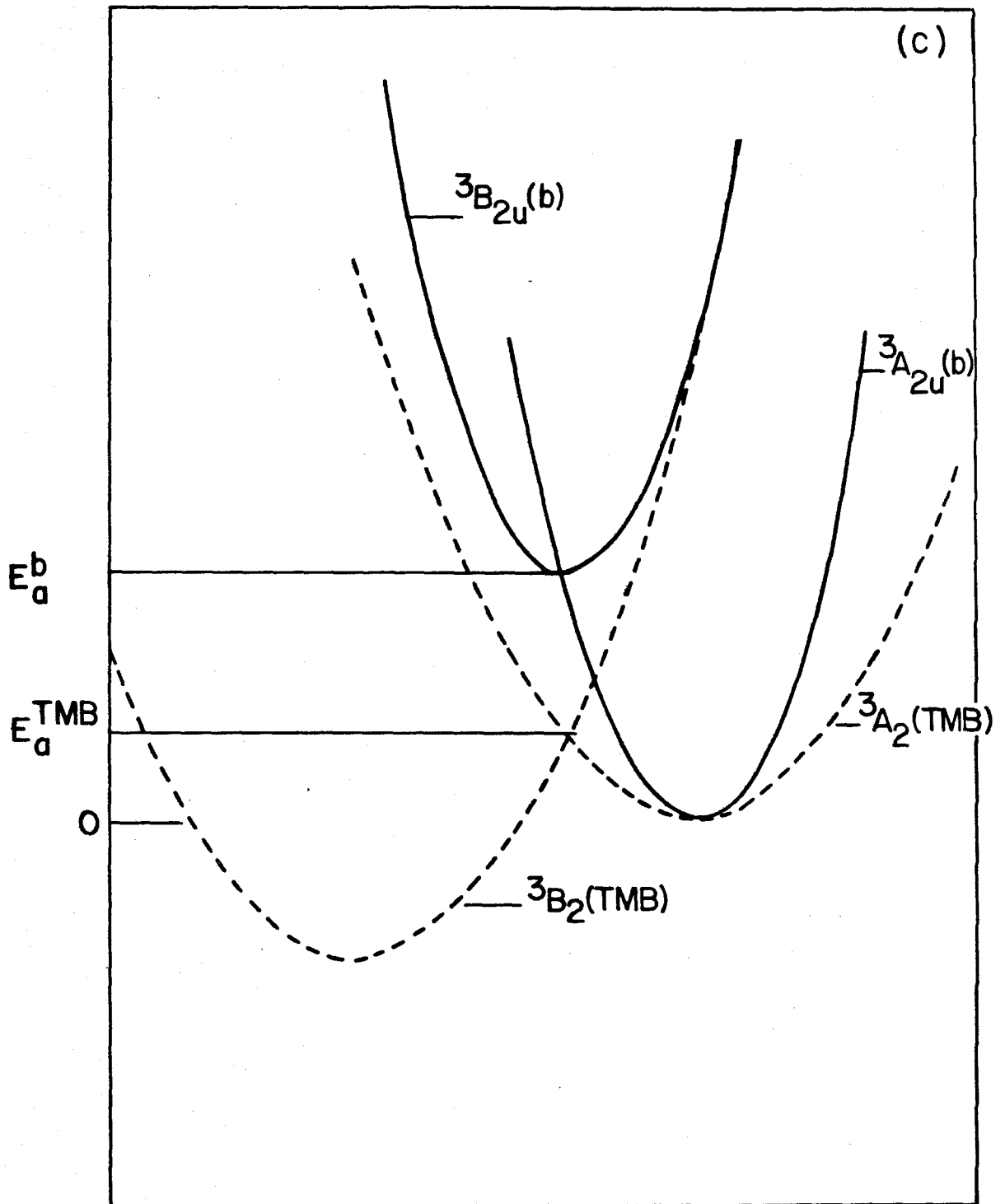
$$\frac{d \log k_{obs}}{d 1/T} = \frac{d \log k_{obs}}{d 1/T^*} \frac{d 1/T^*}{d 1/T} = \frac{-E_a}{k} \left( \frac{d 1/T^*}{d 1/T} \right)$$

ignoring the  $T^{-1/2}$  term in the preexponential coefficient. The slope of an Arrhenius plot in which  $d 1/T^* / d 1/T$  is not close to one produces an apparent  $E_a/k$  which can be significantly reduced from the true  $E_a/k$ . The frequency

Figure 21. Three ways of viewing the potential surfaces of the two states involved in the  ${}^3A_{2u}$  nonradiative decay for  $\text{Rh}_2(\text{b})_4^{2+}$  (solid line) and  $\text{Rh}_2(\text{TMB})_4^{2+}$  (dashed line). Figure 21a shows equivalent curvature for the two compounds with different  $E_a$ 's. Figure 21b shows equivalent  $E_a$ 's, but different curvature. Figure 21c shows a combination of these two effects.







observed for  $\text{Rh}_2(\text{DMB})_4^{2+}$  is sufficiently low to allow for the  $E_a$  calculated from the slope of the plot to be fairly accurate because  $d \ln 1/T^* / d \ln 1/T$  is close to unity at 300K.  $\text{Rh}_2(\text{TMB})_4^{2+}$  with an effective frequency of  $500 \text{ cm}^{-1}$  has

$$\frac{d \ln 1/T^*}{d \ln 1/T} = \left( \cosh^2 \frac{\hbar \langle \omega \rangle}{2kT} \right)^{-1} = .30 \text{ at } 300\text{K}.$$

Because  $\text{Rh}_2(\text{TMB})_4^{2+}$  and  $\text{Rh}(\text{DMB})_4^{2+}$  have different effective frequencies, their true  $E_a$ 's are not as similar as the Arrhenius plot suggests. As the ligand becomes more rigid through this series, the  $\hbar \langle \omega \rangle$ 's and the  $E_a$ 's increase significantly. This is shown in Table 7 with these new  $E_a$ 's written as  $E_a^*$ .

#### Section 4

The excitation spectra of the  ${}^3A_{2u}$  and  ${}^1A_{2u}$  emissions point out another photophysical characteristic of these complexes that is somewhat contrary to the wealth of experimental evidence accumulated in studies of organic compounds. The relative luminescent quantum yields for excitation into the  ${}^1A_{2u}$  and the  ${}^1, {}^3E_u$  system show certain orbital symmetry selection rules are more powerful than spin selection rules.

It is usually assumed that excitation into a high energy state of a given spin multiplicity will rapidly populate the lowest excited state of that spin multiplicity.<sup>52</sup>

TABLE 7

Sample	$E_a$ ( $\text{cm}^{-1}$ )	$E_a^*$ ( $\text{cm}^{-1}$ )	$\hbar\langle\omega\rangle$ ( $\text{cm}^{-1}$ )
$\text{Rh}_2(\text{b})_4(\text{Bph}_4)_2$	1040	12500	800
$\text{Rh}_2(\text{TMB})_4(\text{SO}_3\text{CF}_3)_2$	2630	10950	550
$\text{Rh}_2(\text{TMB})_4(\text{PF}_6)_2$	2980	9750	500
$\text{Rh}_2(\text{TMB})_4^{2+}$ in $\text{H}_2\text{O}$	2660	8700	500
$\text{Rh}_2(\text{TMB})_4^{2+}$ in PMMA	3420	7650	400
$\text{Rh}_2(\text{DMB})_4^{2+}$ in 2-Me THF/ $\text{CH}_3\text{CN}$	2610	3660	250
$[\text{Rh}(\text{cyclohexylNC})_4]_2(\text{BF}_4)_2$	2380	2970	200
$[\text{Rh}(\text{phNC})_4]_2(\text{Bph}_4)_2$	2220	3581	300

In this case  $^1E_u$  excitation should produce  $^1A_{2u}$  excitation in a matter of picoseconds and then intersystem cross over to the  $^3A_{2u}$  at a slower rate.  $^3E_u$  excitation should go directly to the  $^3A_{2u}$  excited state and result in only phosphorescence.

The excitation spectra of these compounds are inconsistent with this description. The excitation spectrum of the fluorescence band should be the same as the phosphorescence when comparing the relative intensities of the  $^1E_u$  and  $^1A_{2u}$  yields. The relative yield for excitation into the  $^1A_{2u}$  and  $^1E_u$  states,

$$\frac{I_{EX}^{1A_{2u}}}{I_{EX}^{1E_u}},$$

is different for fluorescence and phosphorescence in all the rhodium(I) dimers studied. The spectra in Figure 22 show that this value is not the same for fluorescence and phosphorescence in any of the three bridging diisocyanides. The assumption that internal conversion rates are much greater than intersystem crossing rates is not valid.

This behavior can be explained simply by realizing that the spin selection rule does not determine the nonradiative rates because of the large spin orbit coupling present in these transition metal complexes. The loss of the spin selection rule is not completely arbitrary, but is replaced by the spin orbit selection rules of the  $\bar{D}_4$  double group.

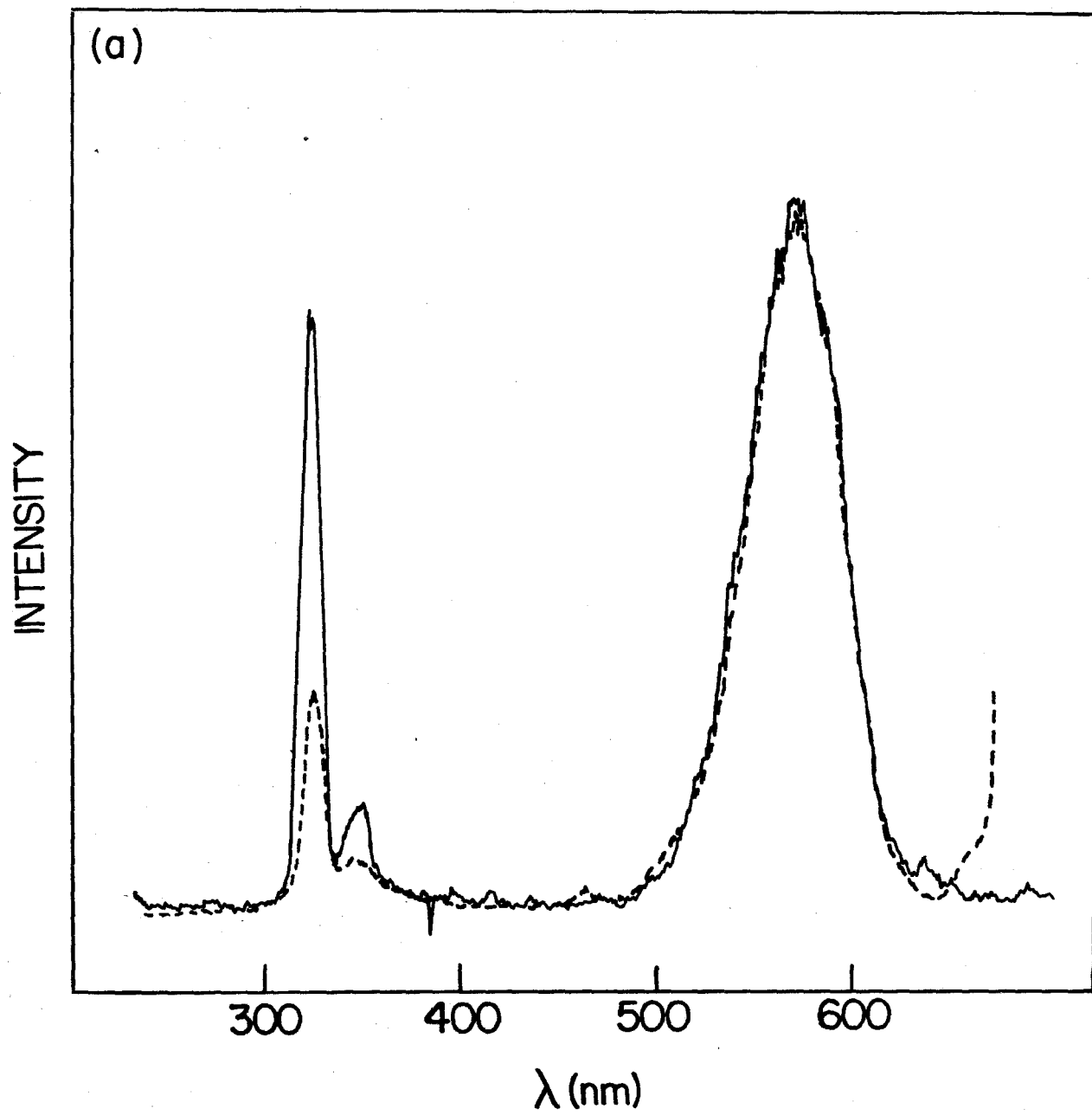
The excitation spectrum of the  ${}^3E_u$  region is different for fluorescence and phosphorescence in Figure 22 showing the maximum of excitation into the  ${}^3E_u$  in  $Rh_2(b)_4^{2+}$  to be at 345 nm for fluorescence and 350 nm for phosphorescence. The  ${}^3E_u(A_{2u})$  state is known to be about 7 nm to higher energy than the  ${}^3E_u(E_u)$  state from the single crystal absorption spectrum of  $Rh_2(TMB)_4(Bph_4)_2$ . Excitation into  ${}^3E_u(E_u)$  decays directly into the  ${}^3A_{2u}(E_u)$ . The excitation into  ${}^3E_u(A_{2u})$  is more likely to get to the  ${}^1A_{2u}(A_{2u})$  first, resulting in the biasing of excitation yield for the two triplet components. These data indicate that the "internal conversion" selection rules are still preserved but it may be more appropriate to interpret them as manifolds in spin orbit notation as  $A_{2u}$ ,  $E_u$ ,  $A_{1g}$ , etc., instead of spin singlets and triplets.

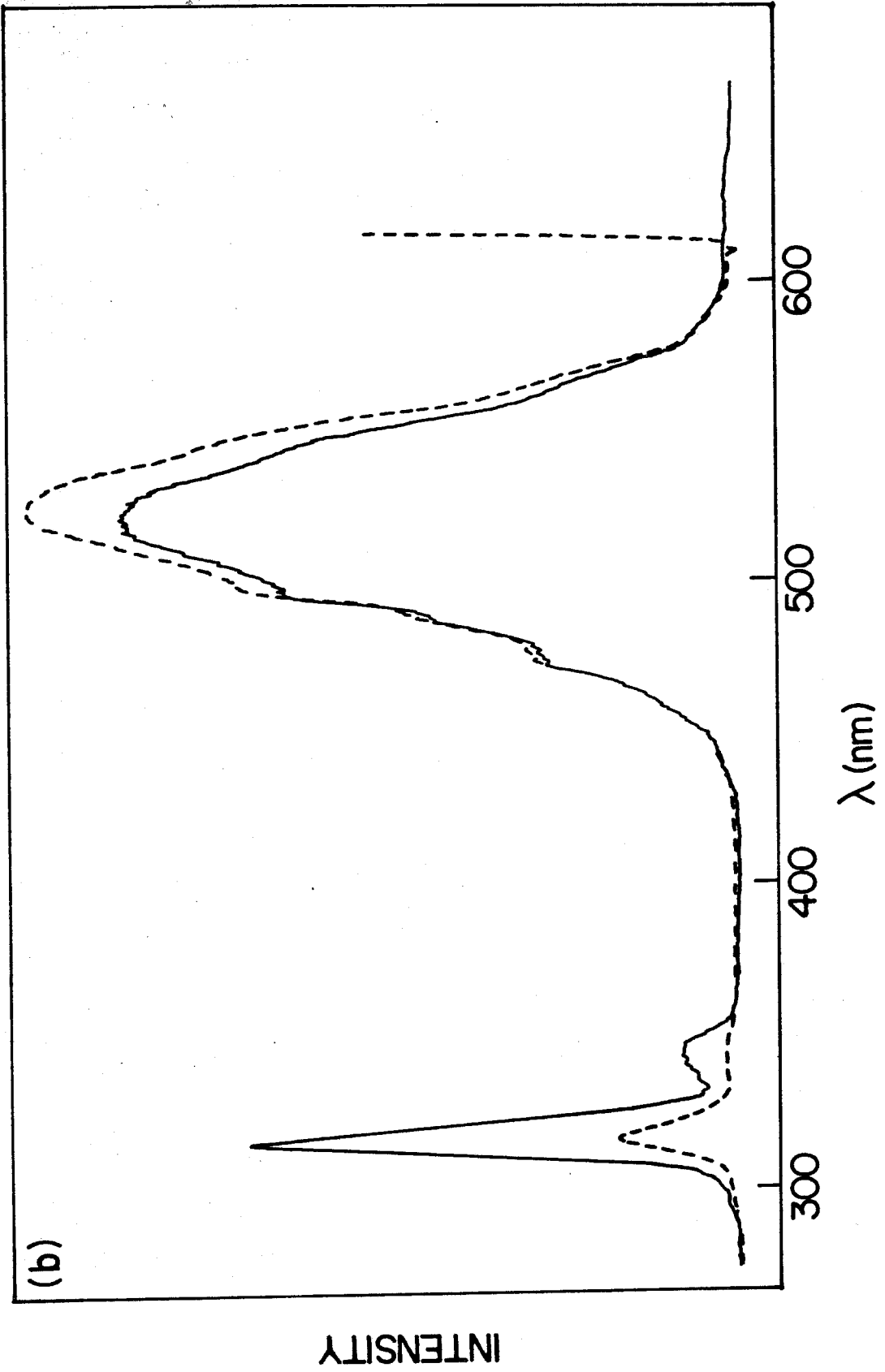
## Section 5

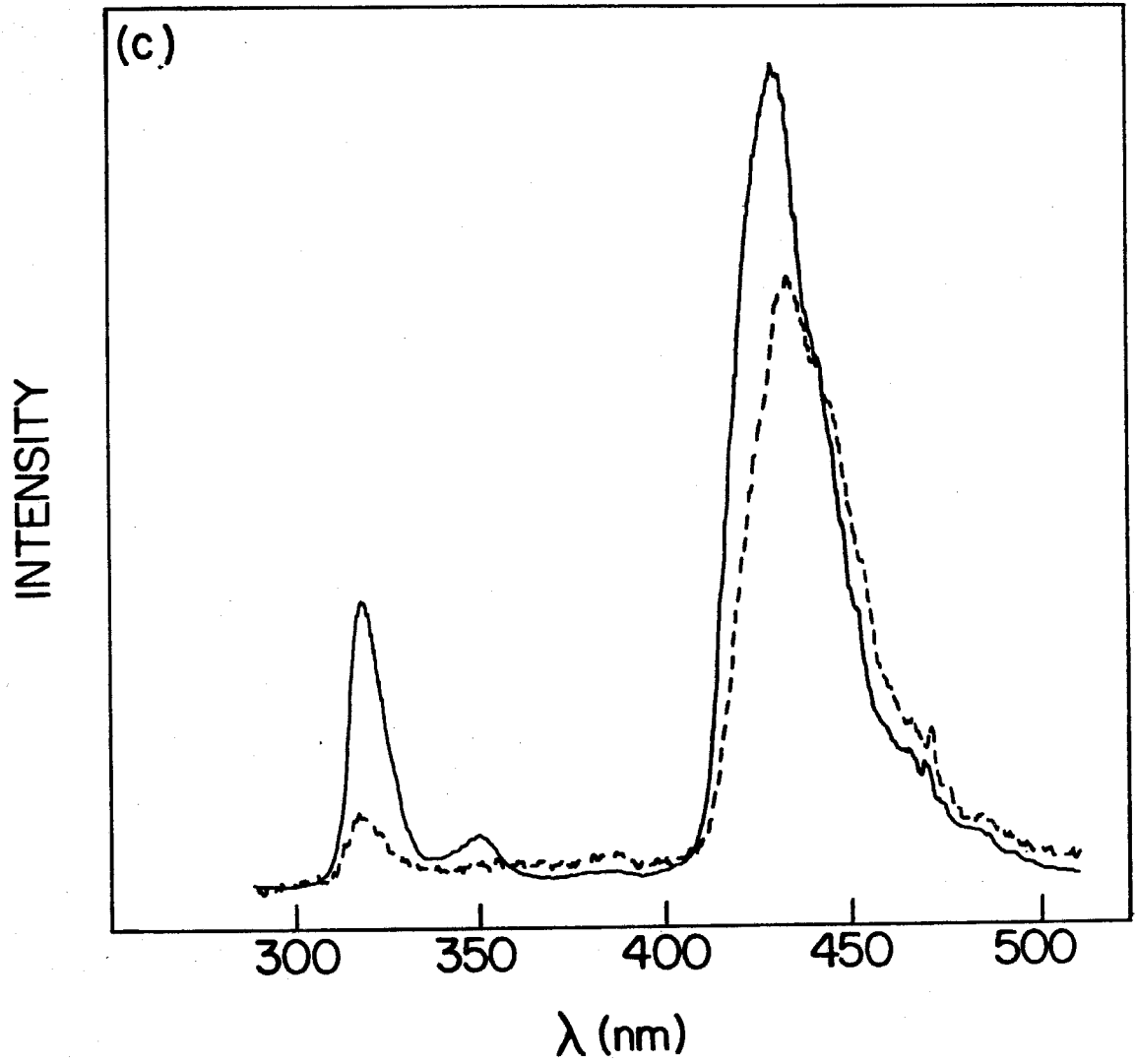
The results presented here raise some interesting questions regarding theory and experiments involving molecular photophysical processes. These studies indicate that inorganic complexes can display nonradiative properties very different from those of organic compounds.

It is clear that these molecules exhibit nonradiative transitions characteristic of the strong coupling limit. The interpretation indicates that the  ${}^3A_{2u}$  state is depopulated through a scheme that involves the presence of a second

Figure 22. Excitation spectra of: a)  $\text{Rh}_2(\text{b})_4^{2+}$ , b)  $\text{Rh}_2(\text{TMB})_4^{2+}$ , and c)  $\text{Rh}_2(\text{DMB})_4^{2+}$  in 2-Methyl THF/acetonitrile at 77K; phosphorescence (solid line), fluorescence (dashed line).







excited state possessing a geometry that allows for rapid decay of electronic excitation to the ground state. This description is strongly supported by the temperature dependence of the  ${}^3A_{2u}$  lifetime in the rhodium(I) dimers and the lack of temperature dependence exhibited by  $\text{Ir}_2(\text{TMB})_4^{2+}$ .

Internal conversion rates are also different in these systems than in organic systems previously studied. The large spin orbit coupling relaxes spin selection rules and replaces them with spin orbit selection rules afforded by the high effective symmetry of these complexes. These new rules allow for the preservation of some state selectivity in non-radiative decay from higher excited states.

The presence of long lived excited states has motivated many researchers to consider them as potential photochemical electron transfer reagents. The energy placed in an excited state through the absorption of a photon in principle can be used to facilitate formidably endothermic reactions.

This study points out the sensitivity of excited state lifetimes to subtle changes in ligands. Other excited states near in energy to a potentially photoactive state have been shown to significantly alter these lifetimes as well. The large effects afforded by small ligand changes show that the understanding of assignments and geometries of states observed in optical spectra can lead to better synthetic tuning of potential photocatalysts.

CHAPTER 4

Optical Spectra of  $\text{Pt}_2(\text{H}_2\text{P}_2\text{O}_5)_4^{4-}$

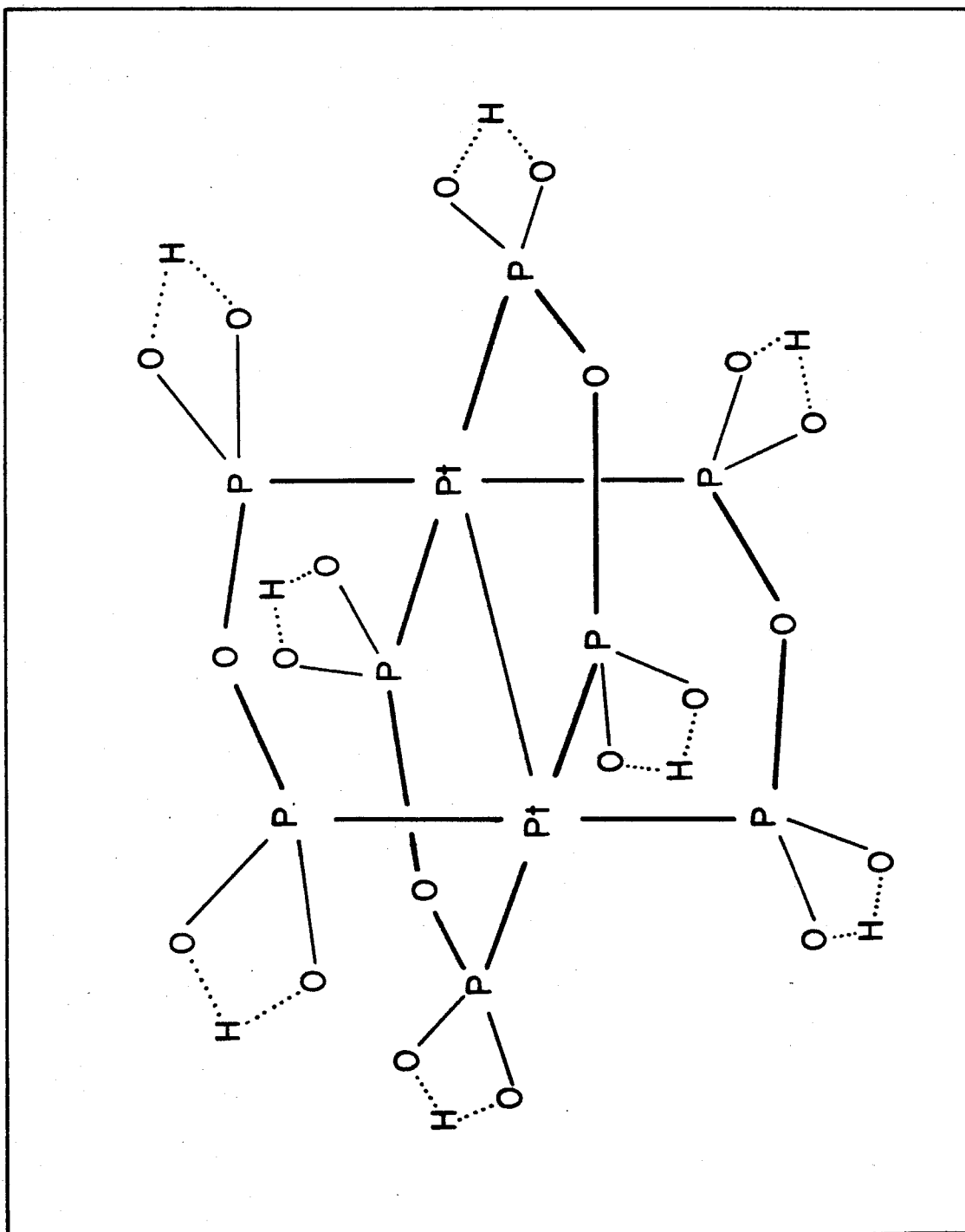
## Section 1

In 1977 Sperline *et al.*<sup>53</sup> reported the synthesis of a green product obtained from the pyrolysis of  $K_2PtCl_4$  and  $H_3PO_3$  that possessed pronounced luminescent properties. Sadler *et al.*<sup>54</sup> grew crystals from this compound and analyzed it by way of X-ray crystallography. These dark green crystals were identified as  $K_4[Pt_2(H_2P_2O_5)_4] \cdot 2H_2O$ . The structure consists of discrete dimers: square planar platinum(II) bridged by four  $H_2P_2O_5^{2-}$  ligands with a Pt-Pt distance of 2.92 Å. Figure 23 displays the structure of this molecule.

This dimer is isoelectronic with the rhodium and iridium diisocyanides allowing for a more direct extension of the dimeric interpretation to the understanding  $d^8-d^8$  infinite chain compounds of  $Pt(CN)_4^{2-}$ . C.M. Che<sup>55</sup> has shown that this ion undergoes facile oxidative addition and photoredox reactions similar to the rhodium and iridium systems. Motivated by the opportunity to perhaps tune the  $d^8-d^8$  photochemical potential into a region more amenable to catalysis, a study was initiated on the absorption and emission of  $Pt_2(H_2P_2O_5)_4^{4-}$  to determine its similarities to the isocyanide dimers.

Recently, Crosby *et al.*<sup>56</sup> have studied the low temperature luminescence lifetime and bandshape of the emission from a sample of  $K_4Pt_2(H_2P_2O_5)_4 \cdot 2H_2O$ . They observed a dramatic change in the emission lifetime of the luminescence

Figure 23. Structure of  $\text{Pt}_2(\text{H}_2\text{P}_2\text{O}_5)_4^{4-}$  based on the crystal structure of Ref. 54.



from the lowest energy absorption band upon cooling from 30K to 5K. They assigned this luminescence as phosphorescence from the  ${}^3A_{2u}$  analogous to the emissive  ${}^3A_{2u}$  in the rhodium isocyanides. They accounted for this behavior in terms of the zero field splitting in the  ${}^3A_{2u}$  excited state similar to their work on certain  $d^8$  monomers.<sup>57</sup>

Their Franck-Condon Analysis of the emission band was flawed due to their unwillingness to utilize the excited state vibrational frequency they observed in the solid state low temperature excitation spectrum. Through the use of high resolution absorption and emission spectroscopy, this investigation corrects and verifies different aspects of the results of Fordyce, Brummer, and Crosby.

## Section 2

$\underline{K_4Pt_2(H_2P_2O_5)_4 \cdot 2H_2O}$ . A crude green sample of  $K_4Pt_2P_8O_{20}H_8 \cdot 2H_2O$ <sup>54</sup> was prepared by the method of Sadler. It was precipitated from water by the addition of methanol to yield a yellow microcrystalline material.

$\underline{Ba_2Pt_2(H_2O_2O_5)_4}$ . 0.3 g of the potassium salt was dissolved in 10 ml of  $H_2O$ . 10 ml of an aqueous solution containing 1.0 g of  $Ba(ClO_4)_2$  was added to the solution of dimer. Large well formed yellow/green plates came out of solution over several hours.

Large (2mm x 2mm x 1mm) dark green crystals of  $K_4Pt_2(H_2P_2O_5)_4 \cdot 2H_2O$  were grown by slow diffusion of methanol into an aqueous solution of the dimer in a desiccator. Samples of these crystals were examined under the polarizing microscope exhibiting optical figures on both hk0 and 00l faces indicative of a tetragonal crystal system. A large crystal was polished to a thickness of 10  $\mu$  on an hk0 face. Visually, this crystal was pale yellow in one polarization and dark blue in the other polarization. The dark blue direction was determined to be along the c axis of the crystal, parallel to the metal-metal bond. The other direction (pale yellow) is exactly perpendicular to the internuclear axis.

The intense blue color in the one polarization was puzzling since the solution spectrum contains no band suggesting the solid should be anything but yellow. The crystal spectrum exhibited an exceedingly broad band in this blue polarization with a maximum at 550 nm. It was first suspected that this band could be due to solid state effects associated with the stacked nature of the crystal structure. However, it was determined that these crystals are reasonably air sensitive exhibiting a color change when crushed with a mortar and pestle. A powder obtained from grinding the dark green crystals is blue, not yellow.

The most probable cause for the blue color is oxidation of a small percentage of the platinum dimers producing an odd electron  $d^8-d^7$  dimer. Transitions associated with this chromophore are expected to be quite intense and at fairly low energy, particularly if the solid structure allows for a delocalization of this electron hole over several dimers.<sup>58</sup> These green crystals also exhibit a fairly large EPR signal strongly supporting this conclusion.<sup>59</sup> It appears as though the X-ray crystallography and all other work performed on this system where green crystals were used had the presence of an oxidized platinum impurity.

Pure yellow single crystals of  $K_4Pt_2(H_2P_2O_5)_4 \cdot 2H_2O$  were grown fairly easily. 1.5 g of freshly precipitated  $K_4Pt_2(H_2P_2O_5)_4$  was dried on a vacuum line and then dissolved in 40 ml of degassed  $H_2O$  added to the powder by bulb-to-bulb distillation. The water was then slowly distilled away from the compound over several days by connecting the sample flask to a flask immersed in salted ice at  $-2^\circ C$ . In this way crystals could be grown in the absence of oxygen.

This method would on occasion yield very large (5mm x 5mm x 1mm) bright yellow crystals with optical properties once again consistent with a tetragonal space group. X-ray photographs were taken of several of these samples. They displayed the same space group and unit cell dimensions as those obtained by Sadler *et al.*<sup>54</sup> The crystals

were typically square slabs exhibiting the 001 face with the 110,  $\bar{1}10$ ,  $1\bar{1}0$  and  $\bar{1}\bar{1}0$  faces as edges. Occasionally 2mm x 1mm x 1mm rectangular blocks were obtained with the 110 and 001 faces as the larger surfaces.

### Section 3

The room temperature absorption and emission spectrum of  $\text{Pt}_2(\text{H}_2\text{P}_2\text{O}_5)^{4-}$  is shown in Figure 24. The intense band at 360 nm and the weak band at 450 nm are not observed in other square planar platinum(II) complexes. Both absorption bands exhibit luminescence similar to the rhodium(I) isocyanides. Because of the short internuclear distance and the understanding of the trends adopted by various absorption bands in  $d^8$  dimers developed in the previous chapters, these two bands are assigned as  ${}^1A_{1g} \rightarrow {}^3A_{2u} (d_{z^2} \rightarrow p_z)$  and  ${}^1A_{1g} \rightarrow {}^1A_{2u} (d_{z^2} \rightarrow p_z)$ .

In spite of the problems encountered in obtaining an adequate sample of  $\text{K}_4\text{Pt}_2(\text{H}_2\text{P}_2\text{O}_5)_4$  the low temperature optical spectrum proved to contain a remarkable amount of information. The transition at 460 nm exhibited an extensive amount of sharp vibronic structure, the individual bands being even more resolved than in  $\text{Rh}_2(\text{b})_4(\text{Bph}_4)_2$ . However, early in these absorption studies it appeared as though there were still problems associated with the quality of the sample.

Figure 24. Absorption (solid line) and emission (dashed line) spectra of a degassed aqueous solution of  $\text{Pt}_2(\text{H}_2\text{P}_2\text{O}_5)_4^{4-}$ .

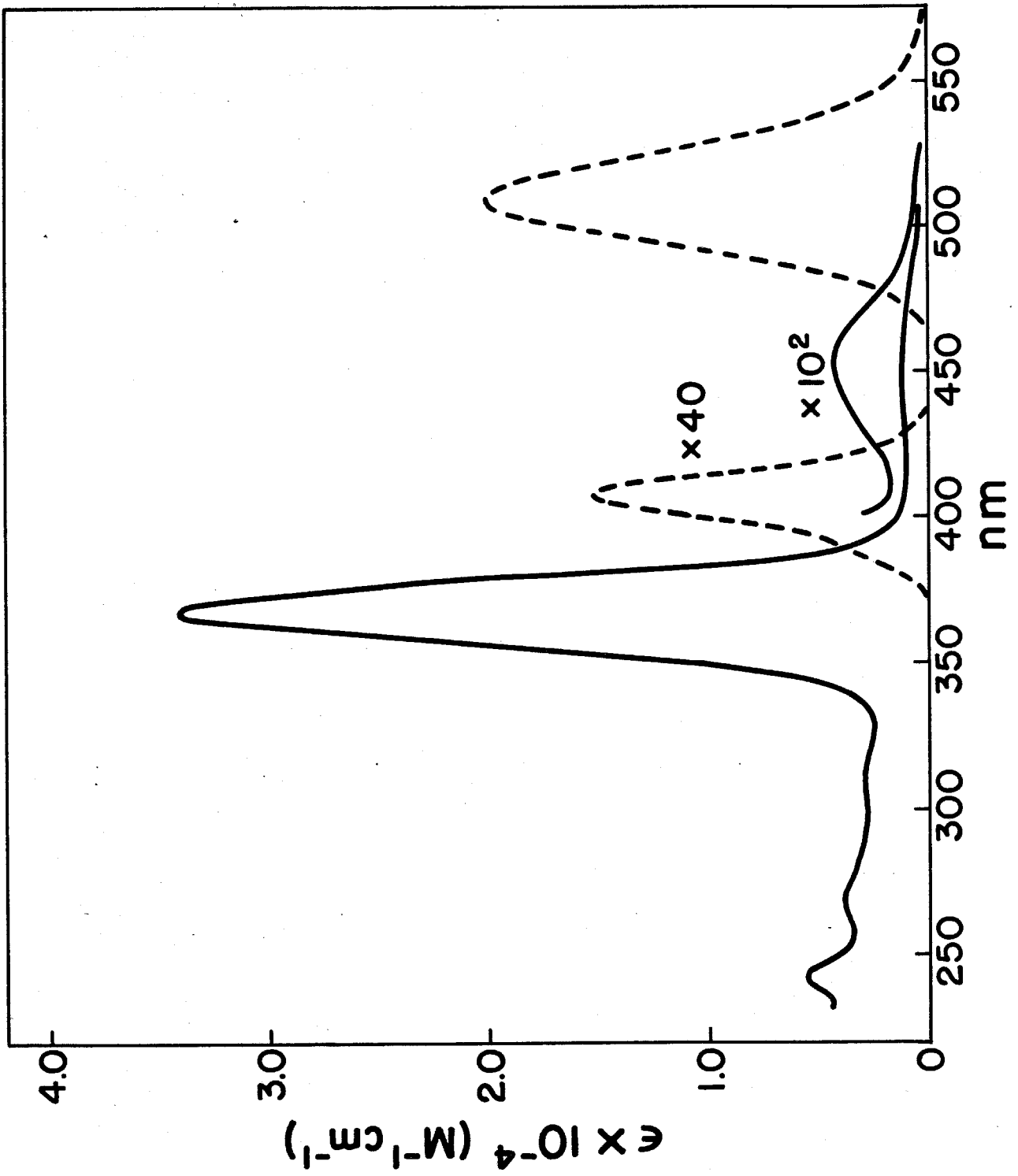


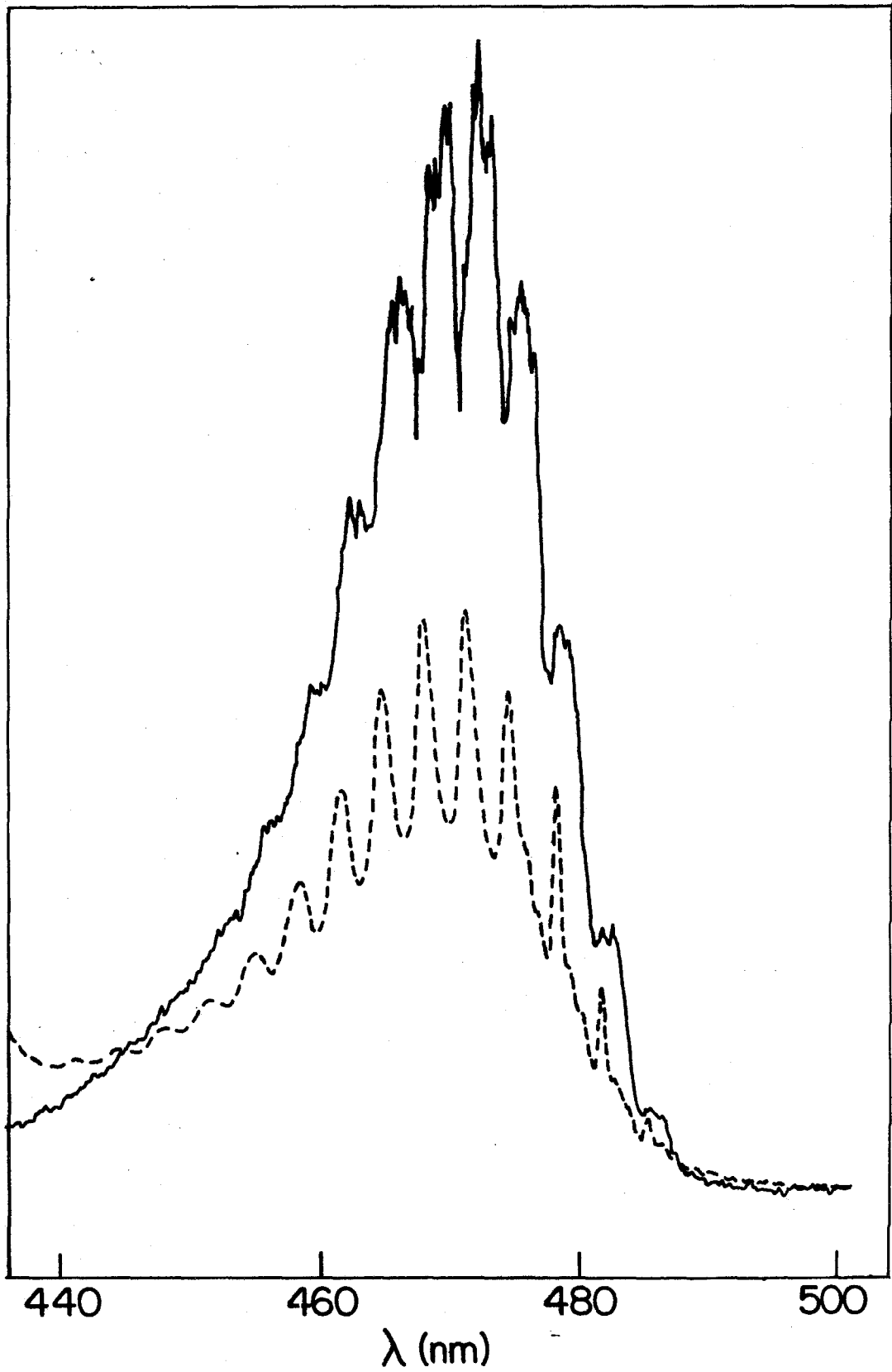
Figure 25 shows the two types of absorption spectra obtained from samples of different recrystallization batches. They are identified as Type A and Type B. Type A was the much more common of the two spectra; Type B only seemed to occur when the crystals were grown very slowly. Because of the overwhelming differences in these two spectra regarding the positions and relative intensities of the lines, it was important to determine what crystallographic properties could be affecting the optical spectrum of this dimeric anion.

Type A crystals appeared to tarnish after several days of exposure to air. The surface of the crystal would become brown/green and have a somewhat mottled appearance. Type B crystals did not tarnish. When placed under vacuum, Type A crystals lost their crystallinity by changing color to a reddish orange and developing numerous small cracks. Type B crystals were insensitive to vacuum. X-ray oscillation and Weissenberg photographs were taken of both types of crystals. Although the lattice dimensions in the two crystals were identical, many of the Type A reflections were smeared, whereas Type B crystals had well formed spots throughout the entire photograph.

These data indicate that Type A crystals are disordered to a serious extent, perhaps a result of the rapidity of crystal formation. The Type B crystals show no gross evidence of disorder but upon examination of the details of the spectra, several weaker lines were observed at the same

Figure 25. Absorption spectrum of: a) Type A (solid line) and b) Type B (dashed line) crystals of  $\text{K}_4 \text{Pt}_2(\text{H}_2\text{P}_2\text{O}_5)_4 \cdot 2\text{H}_2\text{O}$  in the  ${}^1\text{A}_{1g} \rightarrow {}^3\text{A}_{2u}$  region at 5K. Crystals are not of the same thickness.

ABSORBANCE



positions as lines in Type A. This indicates that these disorders may still exist in Type B crystals and are simply not present to such a large extent. Colson<sup>60</sup> has reported variable linewidths and band positions for very thin organic crystals ( $\sim 0.5 \mu$ ). If these crystals are simply cracked to varying degrees, transitions in molecules close to these cracks could be considered similar to surface molecules by occurring at these site defects. This could produce more lines than ordinarily would be present in a completely ordered crystal.

Faced with the prospect of trying to analyze the spectrum in terms of defect sites, it was decided to obtain another salt of  $\text{Pt}_2(\text{H}_2\text{P}_2\text{O}_5)_4^{4-}$ . The barium salt,  $\text{Ba}_2\text{Pt}(\text{H}_2\text{P}_2\text{O}_5)_4$ , had been prepared and large crystals could be obtained easily. These crystals were all thin plates exhibiting a two symmetry plane optical figure on the large face. The extinction directions on this face were both yellow, one being more intense than the other. The absorption spectrum at 5K of a thin single crystal is shown in Figure 26 for the two polarizations. The origin region on a much thicker sample is shown in Figure 27.

As in  $\text{Rh}_2(\text{b})_4(\text{Bph}_4)_2$ , we see a progression in a low frequency with the maximum of the band occurring about 10 quanta from the origin. Figure 27 shows the origin to be located at 475.9 nm. The  $0 \rightarrow 1$  vibrational spacing is  $155 \text{ cm}^{-1}$ . There is also a very low energy vibration of  $40 \text{ cm}^{-1}$  built

Figure 26. Absorption spectrum in the two extinction directions of a crystal of  $\text{Ba}_2\text{Pt}_2(\text{H}_2\text{P}_2\text{O}_5)_4$  at 5K.

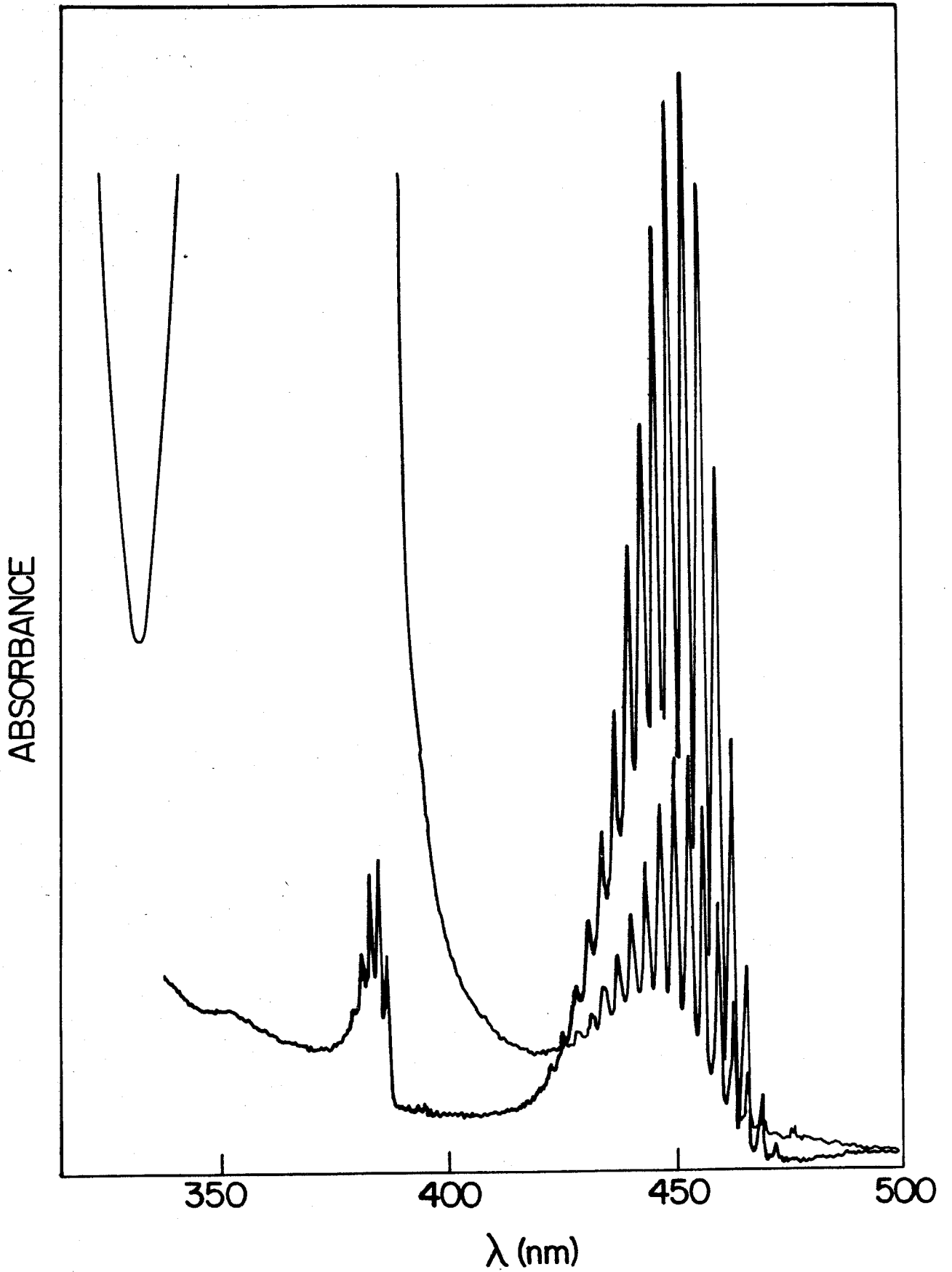
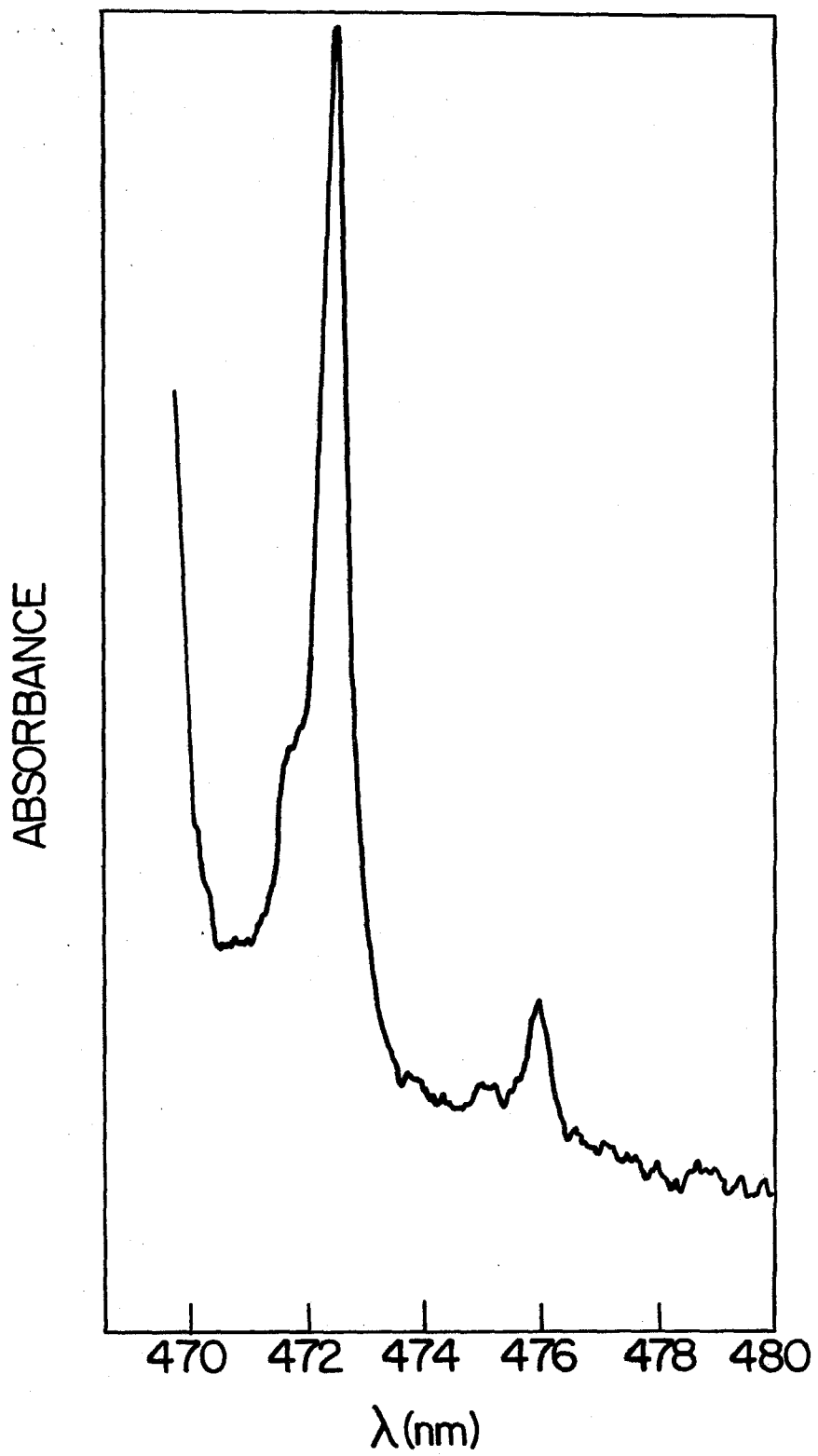


Figure 27. Absorption spectrum in the origin region of the  ${}^1A_{1g} \rightarrow {}^3A_{2u}$  band in a crystal of  $Ba_2Pt_2(H_2P_2O_5)_4$  at 5K.



on the origin similar to the  $60\text{ cm}^{-1}$  vibration in  $\text{Rh}_2(\text{b})_4(\text{Bph}_4)_2$ . The  $155\text{ cm}^{-1}$  mode is assigned as the metal-metal stretch in the  ${}^3\text{A}_{2\text{u}}$  excited state and the  $40\text{ cm}^{-1}$  mode is assigned as a ligand deformation. Table 8 has the list of positions for all the lines.

The overall polarization of this band in the potassium salt combined with X-ray photographs identifying it as x,y polarized support the assignment of this band as  ${}^1\text{A}_{1\text{g}} \rightarrow {}^3\text{A}_{2\text{u}}$ . The intense band which goes off scale in the parallel polarization is z polarized agreeing with the assignment of the 360 band as  ${}^1\text{A}_{1\text{g}} \rightarrow {}^1\text{A}_{2\text{u}}$ . Unlike the potassium salt, the barium salt has a fairly intense contribution to the  ${}^1\text{A}_{1\text{g}} \rightarrow {}^3\text{A}_{2\text{u}}$  absorption in both extinction directions. The orientation of the dimer is not known in this salt and it is therefore possible that one of the two directions presented by the crystal could be pure x,y polarized but the other not purely z polarized. The  ${}^1\text{A}_{1\text{g}} \rightarrow {}^3\text{A}_{2\text{u}}$  intensity along both these extinction directions could still be entirely molecular x,y with essentially no z intensity as is the case with  $\text{K}_4\text{Pt}_2(\text{H}_2\text{P}_2\text{O}_5)_4 \cdot 2\text{H}_2\text{O}$  and  $\text{Rh}_2(\text{b})_4(\text{Bph}_4)_2$ .

One more feature in the optical spectrum of this compound should be noted. The absorption spectra of both the barium and potassium salts exhibit a structured band at about 400 nm, depending on the salt. The band is essentially the same in both salts having a progression in about  $120\text{ cm}^{-1}$ ; once again presumed to be the metal-metal stretch. This

TABLE 8

$v^a$	$E_v$ ( $\text{cm}^{-1}$ )	$\Delta^b$	$E_v - E_{v-1}$
0	21008 21053	40	
1	21163 21199	36	155
2	21317 21346	29	154
3	21473 21500	27	156
4	21626 21651	25	153
5	21778 21805	27	152
6	21927		149
7	22081		154
8	22234		153
9	22389		155
10	22548		159
11	22706		158
12	22865		159
13	23023		158
14	23175		152
15	23324		149
16	23487		163
17	23631		144
18	23793		162
19	23952		159

<sup>a</sup>The assigned  $a_{1g}$  (Pt-Pt) vibrational quantum number.

<sup>b</sup>Spacings between the principal peaks in the progression and the secondary (ligand deformation) peaks.

vibration does not change significantly upon excitation from the ground state in this transition. There is a small distortion present because the maximum of the band is at  $v = 1$  or  $2$  instead of  $v = 0$ . This distortion is assumed to be a contraction because of the slight, although measurable increase in vibrational frequency.

The intensity of this transition was not entirely reproducible. Ordinarily this behavior would be indicative of an impurity absorption. However, the excitation spectrum of the  ${}^3A_{2u}$  emission shows the presence of this state, including the fine structure, displaying that this transition leads to luminescence from the  ${}^3A_{2u}$ . Provided energy transfer within the crystal is slower than this state's lifetime, the excitation spectrum is strong evidence for this state to be an intrinsic property of the  $Pt_2(H_2P_2O_5)_4^{4-}$  anion and not due to an impurity. The orientation of the ions, and therefore the transition dipole moments, are not known in the barium salt. If the transition has vibronic induced intensity, it is quite possible that the transition moment is not oriented along the same direction as  ${}^3A_{2u}$  transition moment. Furthermore, all the crystals examined may not have been oriented on the same face, resulting in variations in the ratio of intensities of this band to the  ${}^1A_{1g} \rightarrow {}^3A_{2u}$ .

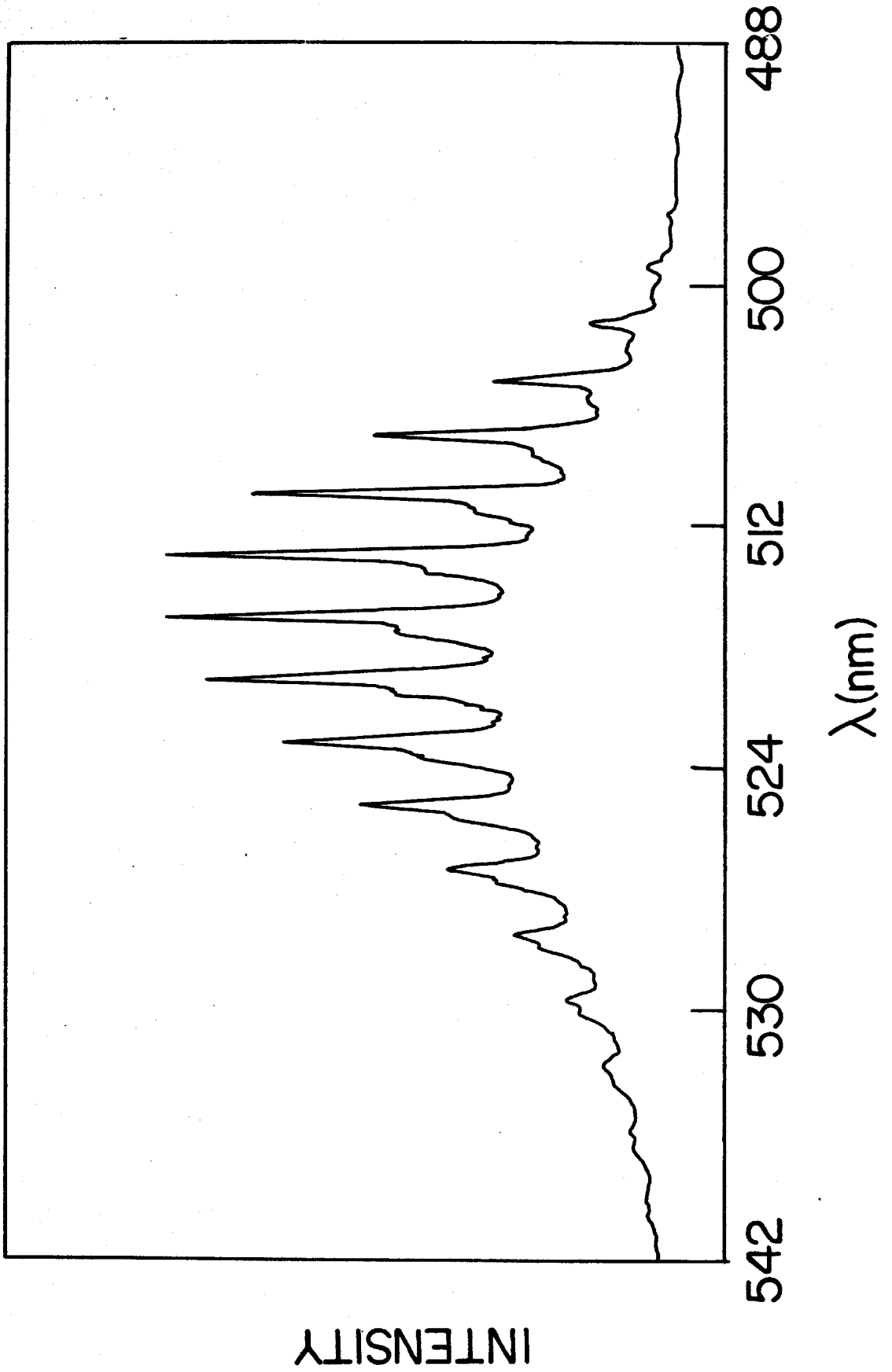
Whether this variation is explained by orientation discrepancies or defect induced intensity, the excitation

spectrum indicates that this band is due to the  $\text{Pt}_2(\text{H}_2\text{P}_2\text{O}_5)_4^{4-}$  chromophore. The logical assignment for this band, because of the small distortion and very small vibrational frequency change is  ${}^1A_{1g} \rightarrow {}^3A_{1g} (d_z^2\sigma \rightarrow p_z\sigma)$ .

The luminescence of the  $\text{Pt}_2(\text{H}_2\text{P}_2\text{O}_5)_4^{4-}$  anion is very intense. Figure 24 shows an emission spectrum of a degassed solution of the dimer with excitation at 360 nm. As in the rhodium(I) and iridium(I) diisocyanides, transitions corresponding to both  ${}^1A_{2u} \rightarrow {}^1A_{1g}$  and  ${}^3A_{2u} \rightarrow {}^1A_{1g}$  are observed.

The 10K single crystal emission spectrum of  $\text{K}_4\text{Pt}_2(\text{H}_2\text{P}_2\text{O}_5)_4 \cdot 2\text{H}_2\text{O}$  is shown in Figure 28. Crosby *et al.*<sup>56</sup> had identified the phosphorescence as having vibrational structure; however, the linewidths they observed for the potassium salt (green crystals) are much wider than in this spectrum. Although they report that spectral resolution was not instrument limited, it appears as though the impurities in their material have served to inhomogeneously broaden these lines. It was noticed that pure yellow samples of  $\text{K}_4\text{Pt}_2(\text{H}_2\text{P}_2\text{O}_5)_4$  had broader linewidth crushed into a powder. This supports the conclusions drawn regarding the site defects in Type A and Type B crystals. They used a microcrystalline material and as has been pointed out,<sup>61</sup> this could have an effect on linewidth. The emission spectrum of the potassium salt in Figure 28 showed irreproducible

Figure 28.  ${}^3A_{2u} \rightarrow {}^1A_{1g}$  phosphorescence of a Type A crystal  
of  $K_4 Pt_2 (H_2P_2O_5)_4 \cdot 2H_2O$ .



spectra between Type A and Type B crystals with Type B samples having a "cleaner" spectrum.

The emission spectrum of  $\text{Ba}_2\text{Pt}_2(\text{H}_2\text{P}_2\text{O}_5)_4$  at 10K is shown in Figures 29 and 30. The phosphorescence spectrum in Figure 29 is similar to that observed in the potassium salt. The most important feature that demonstrates the purity of the barium salt is the almost direct overlap of the 0-0 transition of the absorption and emission bands linking the  ${}^3\text{A}_{2u}$  and  ${}^1\text{A}_{1g}$  states. Neither Type A or Type B crystals of the potassium salt had this expected consistency.

The emission spectrum is similar to the absorption spectrum characterized by a progression in a vibration of  $110\text{ cm}^{-1}$  and  $40\text{ cm}^{-1}$ . The raman spectrum of  $\text{K}_4\text{Pt}_2(\text{H}_2\text{P}_2\text{O}_5)_4$  has a band at  $113\text{ cm}^{-1}$  and has been assigned to the metal metal stretch in the ground state.<sup>56</sup> This is the logical assignment based on arguments analogous to those used for  $\text{Rh}_2(\text{b})_4^{2+}$ . The  $40\text{ cm}^{-1}$  mode is assumed to be the same ligand deformation as is seen in the absorption spectrum. It may appear that the  $40\text{ cm}^{-1}$  vibration progresses in this spectrum. There are certainly some weak features that are at appropriate energies ( $80\text{ cm}^{-1}$ ,  $120\text{ cm}^{-1}$ ) supporting this. However, the line at  $80\text{ cm}^{-1}$  easily seen in the higher quanta of the metal-metal stretch is sharper than the  $40\text{ cm}^{-1}$  vibration, suggesting it is not the  $v = 2$  level of a  $40\text{ cm}^{-1}$  mode. In spite of the observation of this 60 and  $40\text{ cm}^{-1}$  mode in three different spectra of  $\text{Rh}_2(\text{b})_4^{2+}$

and  $\text{Pt}_2(\text{H}_2\text{P}_2\text{O}_5)_4^{4-}$ , its actual coordinate cannot be assigned with great certainty. Table 9 has the positions for all the lines observed.

The highly structured emission and absorption bands in this material offer a unique opportunity to examine the applicability of a Franck-Condon analysis. The FCA adjusts only one parameter,  $\Delta\xi$ , which should be able to fit both the emission and absorption bands relating a pair of states. Using the appropriate input parameters obtained from the origin region listed in Table 10, the absorption and emission bands can be fit independently. According to the theory, the same  $\Delta\xi$  should fit both bands. The calculated bands are shown in Figures 31 and 32.

The  $\Delta X$  for emission and absorption,  $.24 \text{ \AA}$  and  $.19 \text{ \AA}$ , does not turn out to be identical for the two transitions. However, they are quite close and within an acceptable error, using the diatomic approximation, they yield an average distortion of  $.21 \text{ \AA}$ . This distortion is once again a contraction because the ground state frequency is much lower than that of the excited state.

The fluorescence from this salt is seen to be structured as well, although without the same detail as the phosphorescence. It too progresses in the  $110 \text{ cm}^{-1}$  metal-metal stretch characteristic of the ground state with the maximum occurring at least six quanta removed from the origin. An accurate

Figure 29.  ${}^3A_{2u} \rightarrow {}^1A_{1g}$  phosphorescence spectrum of a sample of  $Ba_2Pt_2(H_2P_2O_5)_4$  at 10K.

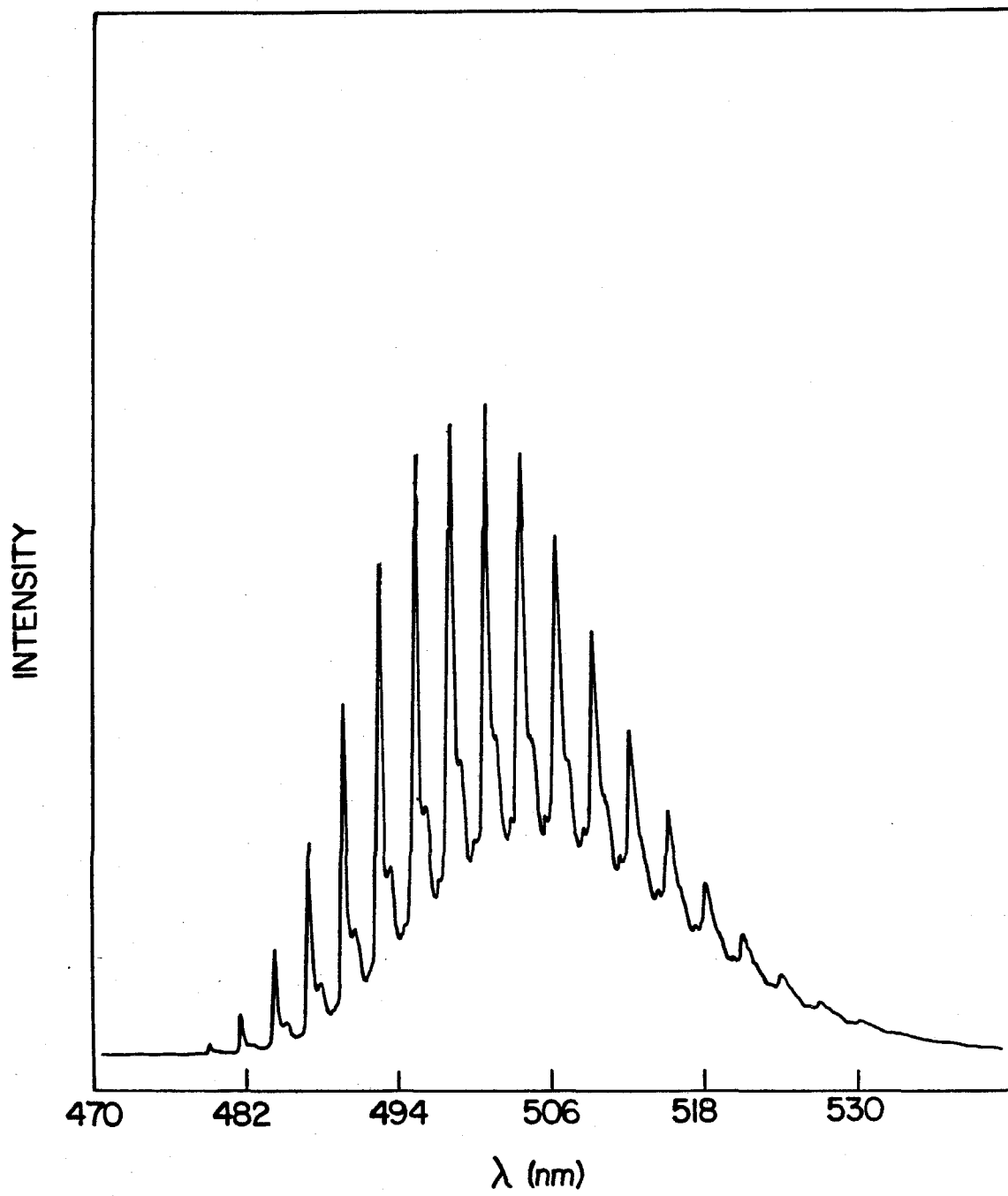


Figure 30.  ${}^1A_{2u} \rightarrow {}^1A_{1g}$  fluorescence spectrum of a  
sample of  $Ba_2Pt_2(H_2P_2O_5)_4$  at 14K.

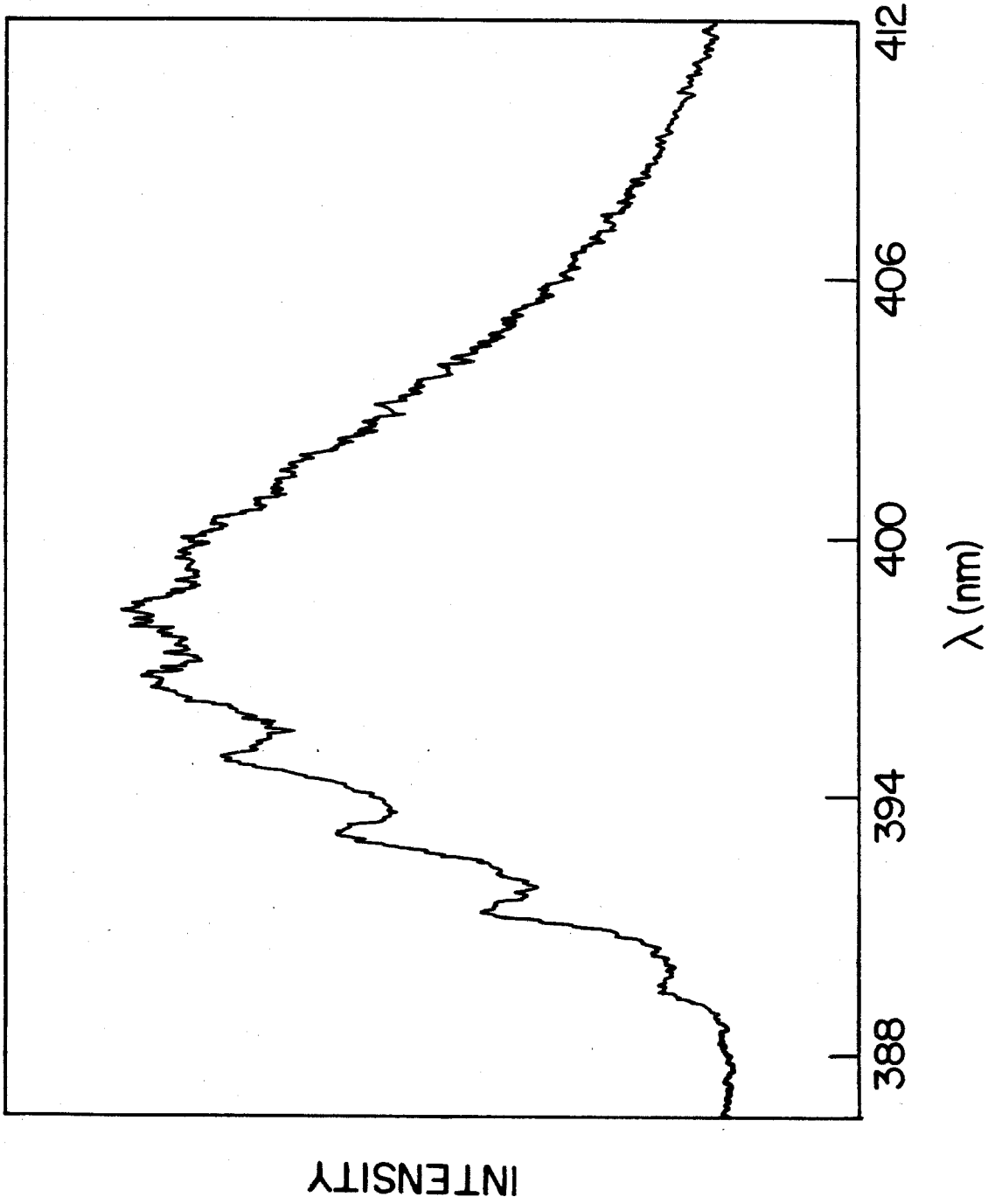


Figure 31. Comparison of the experimental (top) and calculated (bottom) spectrum of the  ${}^1A_{1g} \rightarrow {}^3A_{2u}$  transition in  $Ba_2Pt_2(2P_2O_5)_4$ .

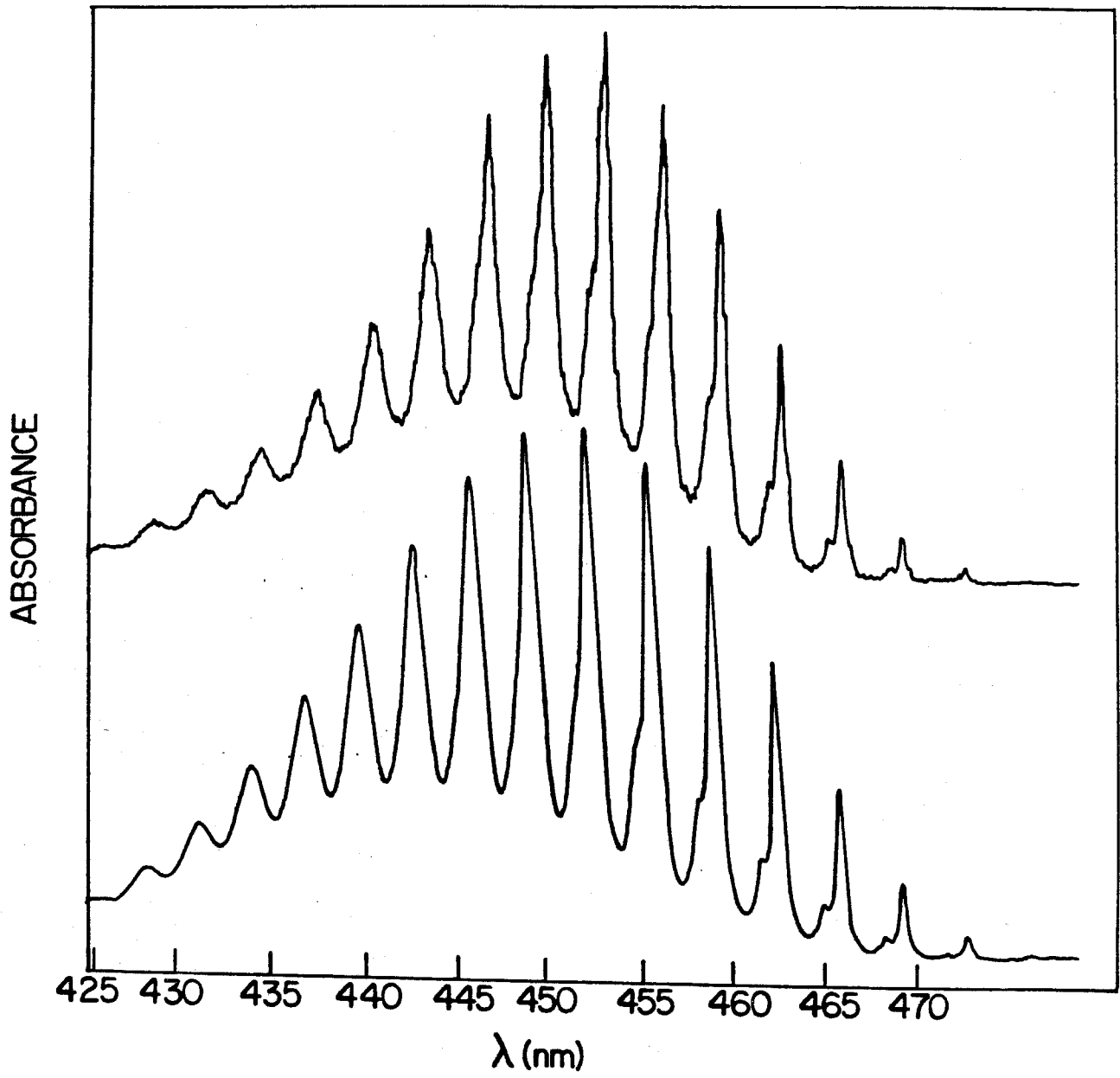


Figure 32. Comparison of the experimental (bottom) and the calculated (top) spectrum of the  ${}^3A_{2u} \rightarrow {}^1A_{1g}$  transition in  $Ba_2Pt_2(H_2P_2O_5)_4$ .

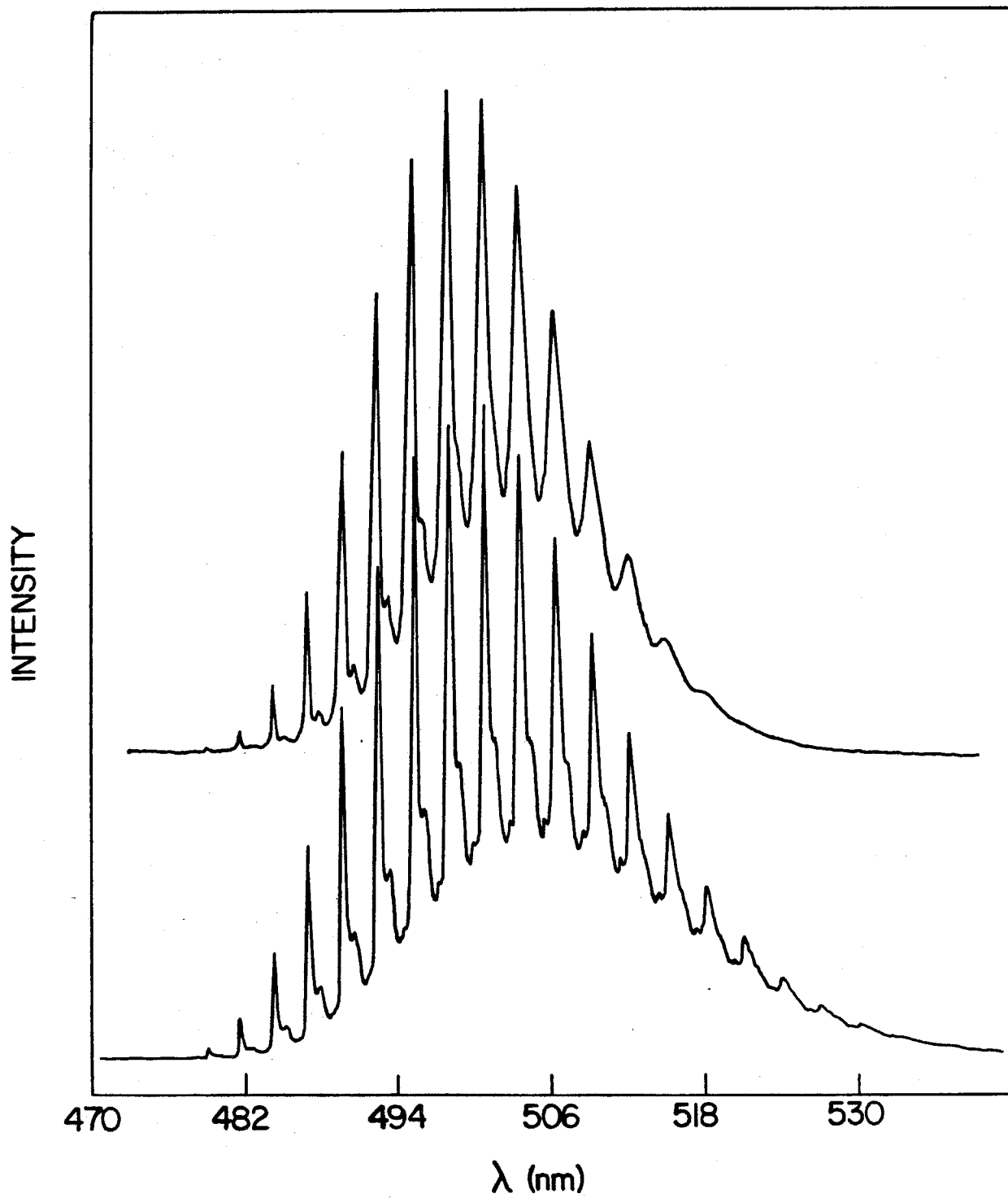


TABLE 9

$v^a$	$E_v$ ( $\text{cm}^{-1}$ )	$\Delta^b$	$\frac{E_v - E_{v-1}}$
0	20987 20947	40	
1	20877 20835	42	110
2	20766 20724	42	111
3	20654 20613	41	112
4	20542 20500 20456	42	112
5	20427 20385 20342	42	115
6	20312 20271 20228	41	115
7	20198 20158 20115	40	114
8	20088 20051 20006	37	110
9	19978 19940 19896	38	110
10	19868 19831 19786	37	110
11	19758 19716 19672	42	110
12	19644 19603 19561	41	114

(continued)

<sup>a</sup>The assigned  $a_{1g}$  (Pt-Pt) vibrational quantum number.

<sup>b</sup>Spacings between the principal peaks in the progression and the secondary (ligand deformation) peaks.

TABLE 9 (cont'd)

<u>V</u> <sup>a</sup>	<u>E<sub>v</sub></u> (cm <sup>-1</sup> )	<u>Δ</u> <sup>b</sup>	<u>E<sub>v</sub> - E<sub>v-1</sub></u>
13	19530		114
	19516		
	19489	41	
14	19447		113
	19417		
	19404		
	19375	42	
	19336		
15	19308		109
	19291		
	19266	42	
	19226		
16	19198		110
	19183		
	19157	41	
	19117		
17	19088		110
	19007		
18	19978		110
19	18864		114
20	18751		113
21	18639		112

TABLE 10

	Absorption	Emission
Primary Linewidth	20 $\text{cm}^{-1}$	7 $\text{cm}^{-1}$
Ground State Frequency	110 $\text{cm}^{-1}$	110 $\text{cm}^{-1}$
Excited State Frequency	156 $\text{cm}^{-1}$	156 $\text{cm}^{-1}$
Secondary Frequency	40 $\text{cm}^{-1}$	40 $\text{cm}^{-1}$
Energy of 0-0	21010 $\text{cm}^{-1}$	21010 $\text{cm}^{-1}$
Intensity of Secondary Line	.3	.4
Secondary Linewidth	30 $\text{cm}^{-1}$	24 $\text{cm}^{-1}$
Anharmonicity	0	0
Broadening Factor	.5	.38

measurement of the location of the origin was not possible due to experimental difficulties. Because the origin was not located in emission, a Franck-Condon Analysis of this structure will not be reliable.

The most interesting result Fordyce, Brummer, and Crosby<sup>56</sup> report is the change in  $^3A_{2u}$  lifetime upon cooling from 30K to 4.2K. This behavior is similar to that observed in rhodium(I) and iridium(I) diphosphines.<sup>57</sup> They account for this change with the following model.

The  $^3A_{2u}$  state is three-fold degenerate neglecting spin orbit coupling. In the double group it splits into  $E_u$  and  $A_{1u}$  components but the direction of the splitting cannot be determined by the current molecular orbital description. The  $E_u$  component is expected to possess a significant transition moment because in  $D_{4h}$  it can gain transition intensity directly from  $^1E_u$  excited states. The  $A_{1u}$  state must rely on lower symmetry effects to gain oscillator strength. The polarization of the  $^3A_{2u}$  absorption confirms this assumption.

Einstein derived a relationship between spontaneous emission rate and absorption oscillator strength. Strickler and Berg<sup>62</sup> have expanded on this relationship and applied it to broad molecular absorption and emission bands. The result is that the luminescent unimolecular rate constant, provided the quantum yield is near unity, is directly proportional to the absorption oscillator strength. A

transition with a weak absorption is associated with an excited state with a long radiative lifetime.

The 9K phosphorescent lifetime of  $K_4Pt_2(H_2P_2O_5)_4 \cdot 2H_2O$  is observed to be 640  $\mu\text{sec}$ .<sup>56</sup> This is compared with the 300K lifetime of 10.3  $\mu\text{sec}$ . Figure 33 depicts the model chosen. As the temperature is lowered to 4.2K, there is no longer an appreciable population in the higher  $E_u$  state to overwhelm the  $A_{lu}$  emission. The lifetime is then observed to be much longer than that of the  $E_u$  state with the much larger oscillator strength. The splitting between the two states is fitted to be  $49 \text{ cm}^{-1}$ .

The structure in the phosphorescence spectrum should show this splitting. As the temperature is lowered from 30K to 4.2K, the intensity of the apparent  $E_u$  origin should diminish and a band  $49 \text{ cm}^{-1}$  lower in energy should appear as the  $A_{lu}$ .

The temperature dependence of the origin region in  $Ba_2Pt_2(H_2P_2O_5)_4$  is shown in Figure 34. The 10K origin obviously loses intensity rapidly as the temperature is lowered. A band appears at 477.48 nm,  $40.8 \text{ cm}^{-1}$  below the 10K origin. It is difficult to determine whether this latter band is present at 10K due to the low energy vibration built on the 476.55 nm origin. The overall spectrum at 4.2K is shown in Figure 35. Table 11 displays the energies of all the lines observed in  $Ba_2Pt_2(H_2P_2O_5)_4$  at 4.2K. The majority of the lines observed at 10K or 4.2K are

Figure 33. Two state model of the  $A_{1u}$  and  $E_u$  components allowing for a temperature dependence in the lifetime of the  ${}^3A_{2u} \rightarrow {}^1A_{1g}$  phosphorescence.

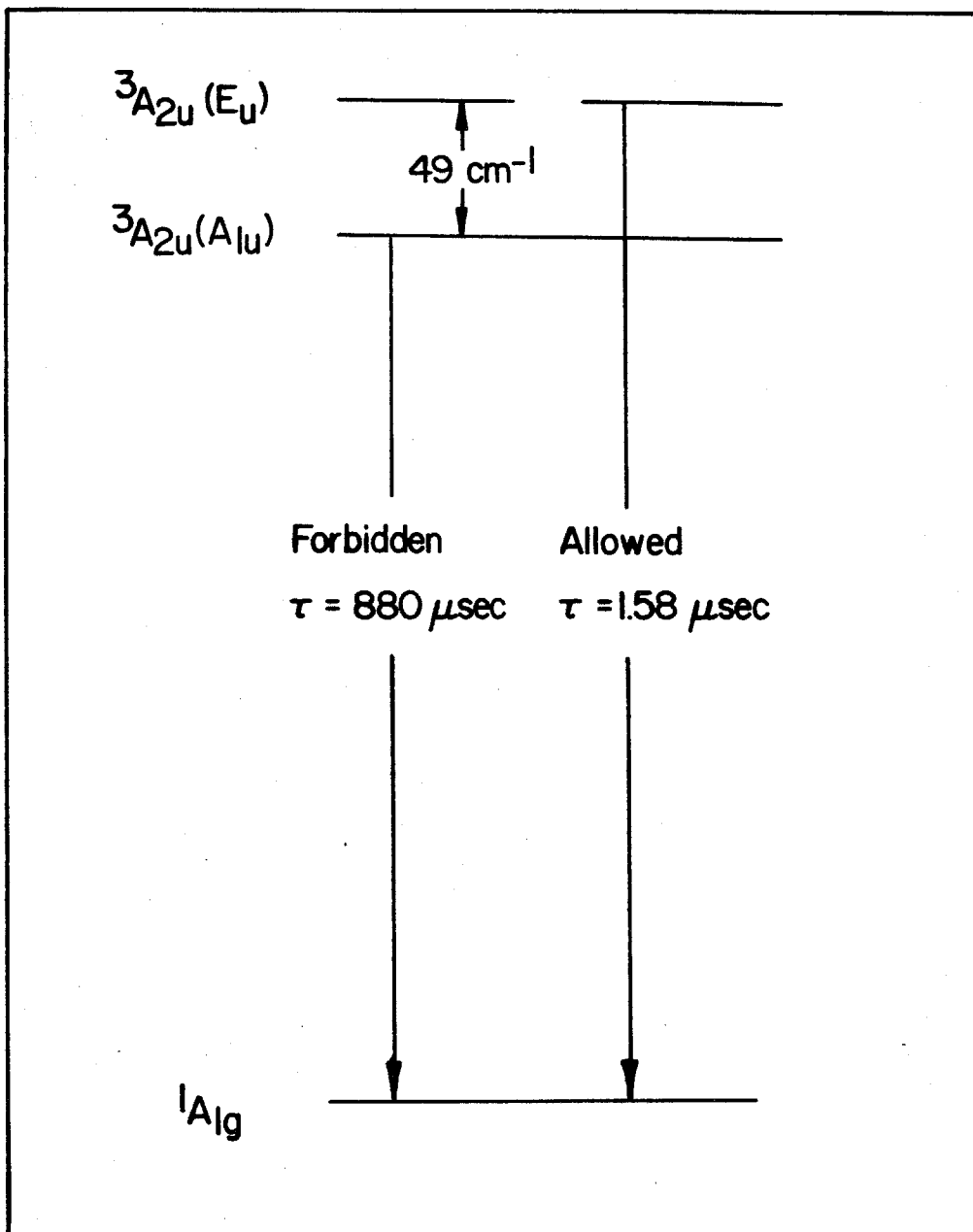


Figure 34. The temperature dependence in the origin region of the phosphorescence of  $\text{Ba}_4\text{Pt}_2(\text{H}_2\text{P}_2\text{O}_5)_4$  at the temperature from the top to bottom, 8K, 7.5K, 6.4K, 5.2K, and 4.2K.

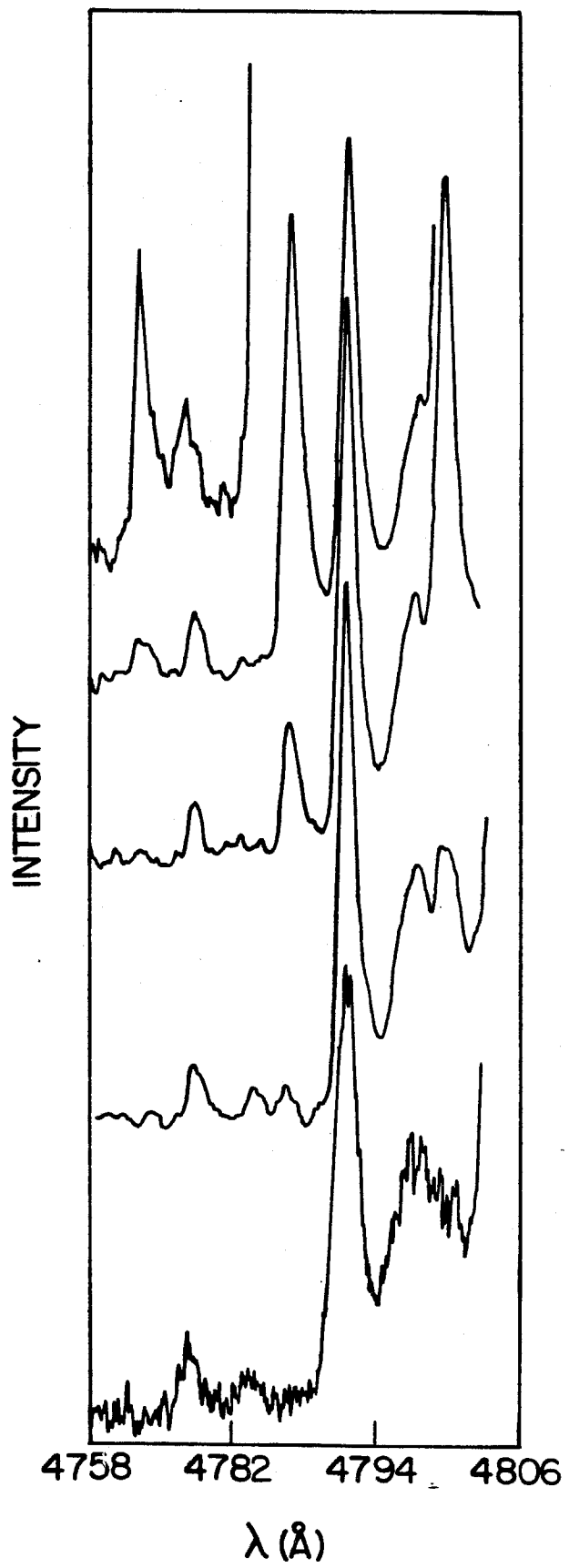


Figure 35. Phosphorescence spectrum of  $\text{Ba}_2\text{Pt}_2(\text{H}_2\text{P}_2\text{O}_5)_4$   
at 4.2K.

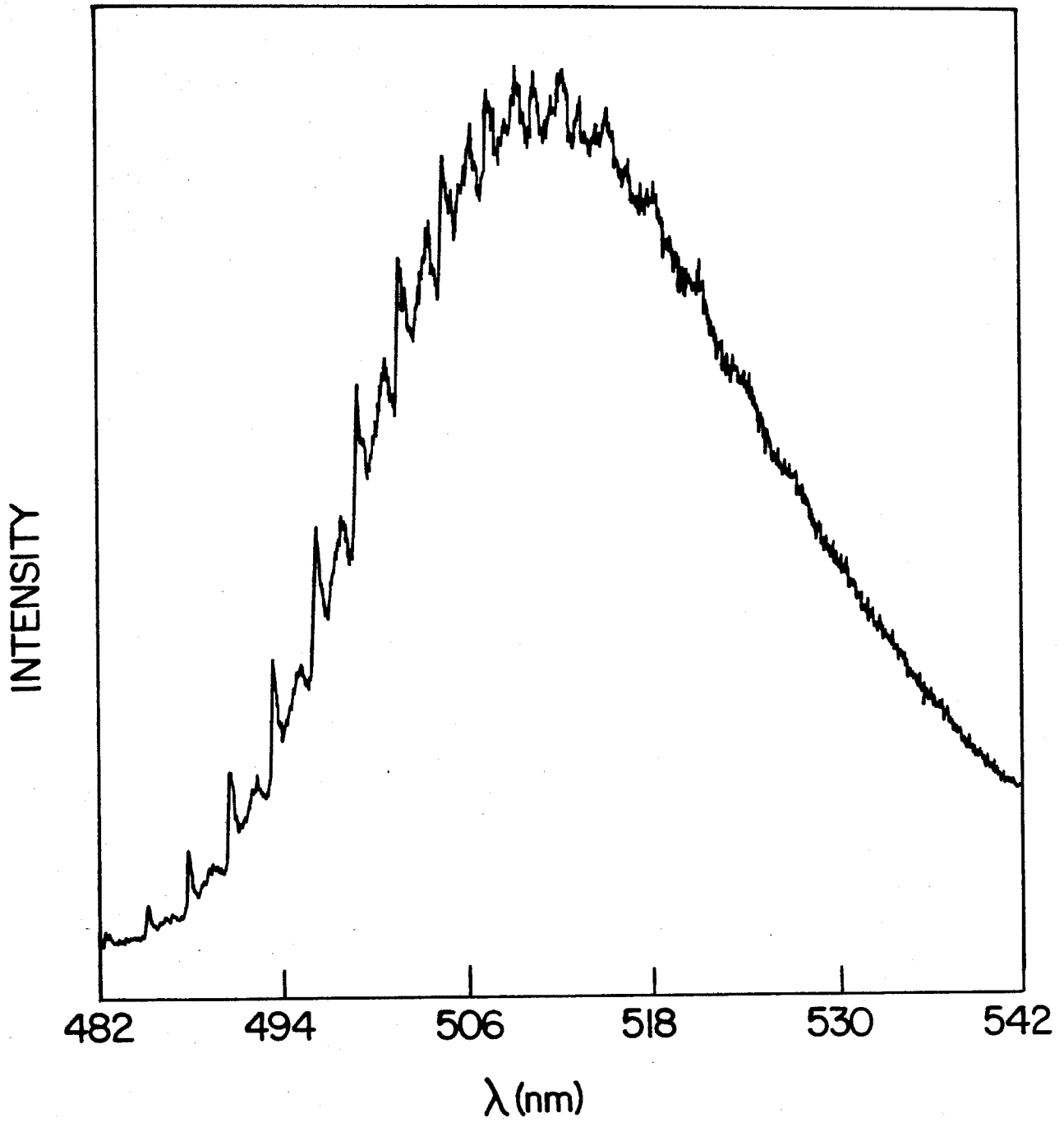


TABLE 11

$v^a$	$E_v$ ( $\text{cm}^{-1}$ )	$\Delta^b$	$E_v - E_{v-1}$
0	20943 20899	44	
1	20828 20781	47	115
2	20722 20672	50	106
3	20610 20560 20536	50	112
4	20496 20445 20429	51	114
5	20383 20329 20311	54	113
6	20269 20220 20200	49	114
7	20157 20106 20088	51	112
8	20045 20000 19978	45	112
9	19934 19890 19866	44	111
10	19825 19780 19757	45	109
11	19713 19667 19641	46	112

(continued)

<sup>a</sup>The assigned  $a_{lg}$  (Pt-Pt) vibrational quantum number

<sup>b</sup>Spacing between the principal peaks in the progression and the secondary (ligand deformation) peak

TABLE 11 (cont'd)

<u>v</u> <sup>a</sup>	<u>E<sub>v</sub></u> (cm <sup>-1</sup> )	<u>Δ</u> <sup>b</sup>	<u>E<sub>v</sub>-E<sub>v-1</sub></u>
12	19600		113
	19554	46	
	19529		
13	19489		111
	19440	49	
	19412		
14	19372		117
	19330	42	
	19305		
	19194		
	19084		
	18975		
	18868		

easily interpretable in terms of either the 476.55 nm origin or the 477.48 nm origin. These two origins progress in about  $110 \text{ cm}^{-1}$  and have a broadened  $40 \text{ cm}^{-1}$  vibration built upon them.

#### Section 4

The experimental results indicate a striking similarity between the electronic structure of  $\text{Pt}_2(\text{H}_2\text{P}_2\text{O}_5)_4^{4-}$  and  $\text{Rh}_2(\text{b})_4^{2+}$ . There are some interesting differences, however, regarding the ground state and excited state metal-metal frequencies. The changes in these frequencies upon electronic excitation yield valuable information regarding the bonding characteristics of the orbitals involved in the electronic transitions. The difference in the relative bonding and antibonding contribution of the  $\sigma$  manifold tests the validity of the generalizations in the description of the  $d^8$  dimer electronic structure initiated by the results obtained from  $\text{Rh}_2(\text{b})_4^{2+}$ .

$\text{Pt}(\text{CN})_4^{2-}$  is a reasonable choice for a model monomer spectrum with which to compare the dimer transition energies. The  ${}^1\text{A}_{1g} \rightarrow {}^3\text{A}_{2u}$  ( $d_{z^2} \rightarrow p_z, \pi^*$ ) in  $\text{Pt}(\text{CN})_4^{2-}$  is located at 281 nm. The  ${}^1\text{A}_{1g} \rightarrow {}^3\text{A}_{2u}$  transition in  $\text{Pt}_2(\text{H}_2\text{P}_2\text{O}_5)_4^{4-}$  is at distinctly lower energy than in this monomer. This is the characteristic dimer stabilization apparently present in all of these systems and can be explained by the same molecular orbital diagram developed for the rhodium systems.

Along with the stabilization of the  $d_{z^2} \rightarrow p_z$  transition, many other spectral properties are similar between  $\text{Rh}_2(\text{b})_4^{2+}$  and  $\text{Pt}_2(\text{H}_2\text{P}_2\text{O}_5)_4^{4-}$ . They both exhibit a long  ${}^3\text{A}_{2u}$  excited state lifetime. The monomer systems, in general, do not have room temperature solution lifetimes even within several orders of magnitude of the microsecond range. Both these dimers have structure on the  ${}^1\text{A}_{1g} \rightarrow {}^3\text{A}_{2u}$  absorption band, but  $d^8$  dimers such as the rhodium and iridium TMB and DMB complexes do not. It appears as though a bridging ligand containing only three members in the bridge enhances the rigidity of the molecule sufficiently to prevent the broadening of the vibronic lines to an overwhelming extent.

The main difference between these two compounds lies in the relative bonding contributions of the various orbitals in the  $\sigma$  manifold. The way in which these orbitals differ is indicative of the kind of changes to be expected between a second and third row metal in this bonding scheme.  $\text{Rh}_2(\text{b})_4^{2+}$  has a ground state metal-metal vibrational frequency of  $85 \text{ cm}^{-1}$ . The heavier platinum dimer has a stretching frequency of  $110 \text{ cm}^{-1}$ . The difference seems even greater when the force constants are considered in the diatomic approximation with values of .21 and .69 mdyne/ $\text{\AA}$ . The ground state metal-metal distances represent this discrepancy with bond lengths of  $3.24 \text{ \AA}$  and  $2.92 \text{ \AA}$ .

The two distances and frequencies can be rationalized in terms of the size of the  $p_z$  orbital doing most of the

bonding. The  $6p_z$  and  $5d_{z^2}$  orbitals in the platinum dimer are larger than the corresponding  $5p_z$  and  $4d_{z^2}$  in  $\text{Rh}_2(\text{b})_4^{2+}$ . The  $6p_z$  in the platinum dimer begins to have significant bonding overlap at a long distance;  $5d_{z^2}$  also interacts in both bonding and antibonding fashion at long range. At a distance of  $2.92 \text{ \AA}$  a great deal of  $6p_z \sigma$  is mixed with  $5d_{z^2} \sigma$ . This suggests that, as opposed to the case of  $\text{Rh}_2(\text{b})_4^{2+}$  where the  $5p_z \sigma$  is much more bonding than  $4d_{z^2} \sigma$ , the  $5d_{z^2} \sigma$  has as much bonding character as  $6p_z \sigma$ . This is represented by the very small change in metal-metal vibrational frequency in the  ${}^1A_{1g} \rightarrow {}^3A_{1g}$  transition and the large ground state force constant. The shorter ground state distance of  $2.92 \text{ \AA}$  is consistent with this enhanced  $d_{z^2}$  bonding character. The smaller distortion upon  $\sigma^* \rightarrow \sigma$  excitation of  $.21 \text{ \AA}$  is also another manifestation of the augmented bonding already present in the ground state of the platinum dimer. This orbital picture does not explain why  $\text{Pt}_2(\text{H}_2\text{P}_2\text{O}_5)_4^{4-}$  has a shorter bond distance than  $3.2 \text{ \AA}$ . It only accounts for the frequency and distortion changes as a result of this shorter distance. The subtleties of how these orbitals mix at various metal-metal distances are not yet clear.

There is a puzzling intensity distribution observed at 4.2K regarding the bands that appear to be built on the  $E_u$  origin. As the metal-metal quantum number increases, these lines begin to dominate the intensity of the band and appear to become more intense than the band built on the

$A_{1u}$  origin. In addition, the apparent maximum of this overall emission band occurs at  $v = 10$ , several quanta different from the maximum at 10K. This is indicative of a different distortion in the  $A_{1u}$  triplet component than in the  $E_u$  component.

The interpretation of the data as representing the two spin orbit components of the  ${}^3A_{2u}$  is not the only one which can account for the temperature dependence and splitting between two origins. In fact it does not account for the enhanced  $E_u$  intensity as a function of metal-metal quantum number at 4.2K. Other explanations, such as one including a double well potential along a coordinate other than the internuclear bond, can account for this behavior. So little is known about the details of inorganic excited state potential surfaces, it is unwise to speculate too profusely with so little information. It should be remembered, however, that when a particular explanation does not account for all the phenomena, other possible interpretations must be considered.

$Rh_2(b)_4^{2+}$  does not exhibit the loss of intensity as does  $Pt_2(H_2P_2O_5)_4^{4-}$  upon cooling to 4.2K. It probably does not have a change in radiative lifetime either, although this experiment is yet to be done. The  ${}^3A_{2u}$  excited states are different in this respect. Either the sign of the splitting is different (the  $A_{1u}$  is higher than the  $E_u$ ) or the splitting in  $Rh_2(b)_4^{2+}$  is simply too small to see an effect on the quantum

yield, even at 4.2K. The single crystal phosphorescence spectrum of  $\text{Rh}_2(\text{b})_4^{2+}$  has its maximum in the  $\perp$  and  $\parallel$  direction at different energies. The  $\parallel$  direction is about 30 nm lower in energy than the  $\perp$  direction although both bands have the same lifetime. This split emission may in some way be related to the two state description in the platinum dimer.

There were several major motivations leading to this spectroscopic study. The primary reason was to test the analogies and differences between  $\text{Rh}_2(\text{b})_4^{2+}$  and  $\text{Pt}_2(\text{H}_2\text{P}_2\text{O}_5)_4^{4-}$  in terms of the metal-metal bonding. Although the bond energies, transition energies, and vibrational frequencies are different, the same qualitative molecular orbital diagram describes the metal-metal interaction in both compounds.

The second reason was to examine more closely the results and conclusions of Crosby *et al.*<sup>56</sup> regarding the low temperature luminescence. The photophysical properties exhibited by  $d^8$  dimers is a fascinating problem and this thesis does not answer all of the questions. The experiments on  $\text{Pt}_2(\text{Pt}_2\text{P}_2\text{O}_5)_4^{4-}$  allow for the likely identification of the zero field splitting in the two components,  $A_{1u}$  and  $E_u$  with results from this study being consistent with the zero field splitting of Crosby *et al.* Their value of  $49 \text{ cm}^{-1}$  corresponds to the  $40.8 \text{ cm}^{-1}$  in the emission spectrum and

is actually quite accurate considering the fitting method they used. Aside from some of the confusing aspects of the intensity distribution, they appear to have an accurate representation of the low temperature luminescent behavior.

The last major question centered around the stabilities of an oxidized platinum(III) and rhodium(II) dimer relative to the reduced platinum(II) and rhodium(I) species. One goal in the study of the photochemistry of these dimers is to destabilize the oxidized  $d^7-d^7$  dimer sufficiently to keep a photochemical redox cycle from falling into a thermodynamic trap with a X-M-M-X electronic structure. Because the platinum(II) dimer has a much stronger bond in the ground state than the rhodium(I) dimer, the difference from  $d^8-d^8$  to  $d^7-d^7$  dimer may be much less in the platinum system in spite of the "full" metal-metal bond present in the oxidized state. A thermodynamic scheme using this system in the presence of an oxidant produces excellent possibilities for a catalytic photoredox cycle.

There are many experiments examining photophysical and bonding properties in these molecules and other  $d^8$  systems yet to be done. Large zero field splitting and effects of nearby excited states are shown here to be particularly important. Studies combining the techniques of time resolved luminescence and single crystal absorption and emission spectra will continue to open up the field of inorganic molecular photophysics.

## REFERENCES

1. G. Herzberg, *Molecular Spectra and Molecular Structure*, Vol. 3, Van Nostrand Reinhold, New York, 1966.
2. *Advances in Laser Chemistry*, A.H. Zewail, ed., Springer-Verlag, Berlin, Heidelberg, 1978.
3. a) C.J. Ballhausen, *Introduction to Ligand Field Theory*, McGraw-Hill, New York, 1962.  
b) B.N. Figgis, *Introduction to Ligand Fields*, Interscience, New York, 1966.  
c) S. Sugano, Y. Tanabe, and H. Kamimura, *Multiplets of Transition Metal Ions in Crystals*, Academic Press, New York, 1970.  
c) J.S. Griffith, *The Theory of Transition-Metal Ions*, Cambridge University Press, London, 1961.
4. F. Basolo and R. Pearson, *Mechanisms of Inorganic Reactions*, John Wiley and Sons, New York, 1967.
5. C.J. Ballhausen and H.B. Gray, *Molecular Orbital Theory*, Chapter 8, W.A. Benjamin, New York, 1965.
6. a) D.S. Martin, R.A. Newman, and P.E. Fanwick, *Inorg. Chem.*, 18, 2511, 1979.  
b) C.D. Cowman and H.B. Gray, *J. Amer. Chem. Soc.* 95, 8177, 1973.  
c) D.S. Martin, T.R. Webb, G.A. Robbin, and P.E. Fanwick, *Inorg. Chem.* 18, 475, 1979.

- d) S.F. Rice, R.B. Wilson and E.I. Solomon, *Inorg. Chem.* 19, 3425, 1980.
- e) W.C. Trogler, E.I. Solomon, I. Trajberg, C.J. Ballhausen, and H.B. Gray, *Inorg. Chem.* 16, 828, 1977.
7. N.J. Turro, *Modern Molecular Photochemistry*, Benjamin/Cumming, Menlo Park, 1978.
8. J. Jortner, S.A. Rice, and R.M. Hochstrasser, *Adv. Photochem.* 7, 149, 1969.
9. *Excited States*, E.C. Lim, ed., Vol. 1, Academic Press, New York, 1974.
10. K. Kawakami, M. Haga, and T. Tanaka, *J. Organomet. Chem.* 60, 363, 1973.
11. N.S. Lewis, K.R. Mann, J.G. Gordon II, and H.B. Gray, *J. Amer. Chem. Soc.* 98, 7461, 1976.
12. C.A. Tolman, *J. Amer. Chem. Soc.*, 92, 6777, 1970.
13. L. Vaska and J.W. DiLuzio, *J. Amer. Chem. Soc.*, 83, 2784, 1961.
14. D. Forster, *Adv. Organomet. Chem.*, 17, 255, 1979.
15. S. Milder, unpublished results.
16. a) L.J. Andrews, *Inorg. Chem.*, 17, 3180, 1978-  
b) L.J. Andrews, *J. Phys. Chem.*, 83, 3203, 1979.
17. G.L. Geoffroy, M.S. Wrighton, G.S. Hammond, and H.B. Gray, *J. Amer. Chem. Soc.*, 96, 3105, 1974.
18. K.R. Mann, J.G. Gordon II, and H.B. Gray, *J. Am. Chem. Soc.*, 97, 3553, 1975.

19. K.R. Mann, N.S. Lewis, R.M. Williams, H.B. Gray, and J.G. Gordon II, *Inorg. Chem.*, 17, 828, 1978.
20. J.S. Miller and A.J. Epstein, *Prog. Inorg. Chem.*, 20, 1, 1976.
21. L. Interrante in *Extended Interaction Between Metal Ions in Transition Metal Complexes*, L. Interrante, ed., American Chemical Society, Washington, D.C., 1974.
22. N.S. Lewis, M.S. Thesis, California Institute of Technology, 1977.
23. K.R. Mann and H.B. Gray, *Adv. Chem. Ser.*, 173, 225, 1979.
24. K.R. Mann, J.A. Thich, R.A. Bell, C.L. Coyle, and H.B. Gray, *Inorg. Chem.*, 19, 2462, 1980.
25. K.R. Mann, *Cryst. Struct. Commun.*, 10, 451-1981.
26. V.M. Miskowski, G.L. Nobinger, D.S. Kliger, G.S. Hammond, N.S. Lewis, K.R. Mann, and H.B. Gray, *J. Amer. Chem. Soc.*, 100, 485, 1978.
27. S.J. Milder, R.A. Goldbeck, D.S. Kliger, and H.B. Gray, *J. Amer. Chem. Soc.*, 102, 6761, 1980.
28. H.B. Gray and C.J. Ballhausen, *J. Amer. Chem. Soc.*, 85, 260, 1963.
29. a) C.D. Cowman and H.B. Gray, *Inorg. Chem.*, 15, 2823, 1976.  
b) C.D. Cowman, C.J. Ballhausen, and H.B. Gray, *J. Amer. Chem. Soc.*, 95, 7873, 1973.
30. H. Isci and W.R. Mason, *Inorg. Chem.*, 14, 913, 1975.
31. D.A. Robert, W.R. Mason, and G.L. Geoffroy, *Inorg. Chem.*, 20, 789, 1981.

32. W.P. Weber, G.W. Gobel, and I.K. Ugi, *Angew. Chem. Int. Ed. Engl.*, 11, 530, 1972.
33. C.J. Ballhausen, *Molecular Electronic Structures of Transition Metal Complexes*, McGraw-Hill, London, 1979, p. 96.
34. The crystallographic face was determined through X-ray oscillation and Weissenberg photographs.
35. T. Keil, *Phys. Rev.*, 140, A601, 1965.
36. a) V.M. Miskowski, R.A. Goldbeck, D.S. Kliger, and H.B. Gray, *Inorg. Chem.*, 18, 86, 1979.  
b) V.M. Miskowski, H.B. Gray, R.B. Wilson, and E.I. Solomon, *Inorg. Chem.*, 18, 1410, 1979.
37. a) H.Yersin, H. Otto, J.L. Zink, and G. Gliemann, *J. Amer. Chem. Soc.*, 102, 951, 1980.  
b) R.B. Wilson, Ph.D. Thesis, Massachusetts Institute of Technology, 1979.
38. a) J. Franck, *Trans. Faraday. Soc.*, 21, 536, 1925.  
b) E. Condon, *Phys. Rev.*, 32, 858, 1928.
39. C.J. Ballhausen, *Molecular Electronic Structures of Transition Metal Complexes*, McGraw-Hill, London, 1979, p. 112.
40. R.F. Dallinger, V.M. Miskowski, H.B. Gray, and W.H. Woodruff, *J. Amer. Chem. Soc.*, 103, 1595, 1981.
41. G. Herzberg, *Molecular Spectra and Molecular Structure*, Vol. 2, Van Nostrand Reinhold, New York, 1950, pp. 456-459.
42. R. Badger, *J. Chem. Phys.* 2, 128, 1934.

43. T.P. Smith, unpublished results.
44. M.F. Bailey and L.F. Dahl, *Inorg. Chem.*, 4, 1140, 1965.
45. K.R. Mann, R.A. Bell, and H.B. Gray, *Inorg. Chem.*, 18, 2671, 1979.
46. R. Levenson and H.B. Gray, *J. Amer. Chem. Soc.*, 97, 6042, 1975.
47. R.T. Birge and H. Sponer, *Phys. Rev.*, 28, 259, 1926.
48. W.C. Trogler, C.D. Cowman, H.B. Gray, and F.A. Cotton, *J. Amer. Chem. Soc.*, 99, 2993, 1977.
49. R. Englman and J. Jortner, *Mol. Phys.*, 18, 145, 1970.
50. C.J. Ballhausen, N. Bjerrum, R. Dingle, K. Eriks, and C.R. Hare, *Inorg. Chem.*, 4, 514, 1965.
51. T.P. Smith, unpublished results.
52. M. Kasha, *Disc. Faraday Soc.*, 9, 14, 1950.
53. R.P. Sperline, M.K. Dickson, and D.M. Roundhill, *J. Chem. Soc., Chem. Commun.*, 62, 1977.
54. M.A. Filomena Dos Remedios Pinto, P.J. Sadler, S. Neible, M.R. Sanderson, and A. Subbiah, *J. Chem. Soc. Chem. Commun.* 13, 1980.
55. C.-M. Che, L.G. Butler, and H.B. Gray, *J. Amer. Chem. Soc.*, 103, 7796, 1981
56. W.A. Fordyce, J.G. Brummer, and G.A. Crosby, *J. Amer. Chem. Soc.*, 103, 7061, 1981.
57. W.A. Fordyce, H. Fau, M.L. Stone, and G.A. Crosby, *Chem. Phys. Lett.*, 77, 405, 1981.

58. a) K.R. Mann, M.J. Dipierro, and T.P. Gill, *J. Amer. Chem. Soc.*, 102, 3965, 1980.
- b) I.S. Sigal, K.R. Mann, and H.B. Gray, *J. Amer. Chem. Soc.*, 102, 7252, 1980.
- c) I.S. Sigal and H.B. Gray, *J. Amer. Chem. Soc.*, 103, 220, 1981.
59. L.G. Butler, unpublished results.
60. S.D. Colson, *J. Chem. Phys.*, 45, 4746,
61. R.M. Rochstrasser and P.N. Prasad in *Excited States*, E.C. Lim, ed., Vol. 1, Academic Press, New York, 1974, pp. 102-104.
62. S.J. Strickler and R.A. Berg, *J. Chem. Phys.*, 37, 814, 1962.

## APPENDIX

The computer program used to calculate the band shapes of  $\text{Rh}_2(\text{b})_4^{2+} \ ^1\text{A}_{1g} \rightarrow \ ^1\text{A}_{2u}$ ,  $\text{Pt}_2(\text{H}_2\text{P}_2\text{O}_5)_4^{4-} \ ^1\text{A}_{1g} \rightarrow \ ^3\text{A}_{2u}$ , and  $\text{Pt}_2(\text{H}_2\text{P}_2\text{O}_5)_4^{4-} \ ^3\text{A}_{2u} \rightarrow \ ^1\text{A}_{1g}$  along with a description of its operation is presented here. It calculates the intensities of up to 25 quanta in a totally symmetric vibration with one or two origins of different intensities. The input parameters are defined as follows.

- DELTOQ - mass normalized distortion between the minima of the ground state and excited state potential surface.
- BUBS - linewidth of 0-0 transition in absorption (wavenumbers).
- BEMP - linewidth of 0-0 transition in emission (wavenumbers).
- HWGR - ground state vibrational frequency (wavenumbers).
- HWEX - excited state vibrational frequency (wavenumbers).
- HW2 - energy difference between first and second origin (wavenumbers).
- OONU - absolute energy of the first origin (wavenumbers).
- SCALE - intensity ratio of the first origin to the second origin.
- BUB2 - linewidth of the second origin in absorption (wavenumbers).
- BEMP2 - linewidth of the second origin in emission (wavenumbers).
- SPACE - size of increment for the overall bandshape (wavenumbers).

- CHIAB - anharmonicity of the absorption spectrum (wavenumbers/quantum).
- CHIEM - anharmonicity of the emission spectrum (wavenumbers/quantum).
- CHAN - change in linewidth per square of the vibrational quanta (wavenumber/quantum<sup>2</sup>).
- NUMV - number of quanta covering the overall band.
- IFLAG - 1 for absorption, 2 for emission, and 3 to calculate both absorption and emission.

The program reads in these values and then calls subroutine HERM which calculates the intensities for the individual lines using the ground and excited state vibrational frequencies and the distortion. It then starts 150 cm<sup>-1</sup> before the origin and increments the energy by the quantity SPACE. It calculates the contribution of each vibronic line at a given energy to the overall intensity by assuming a lorentzian lineshape scaled by intensities calculated in HERM. If there is a second origin, the next step adds this contribution scaled by the factor SCALE. This entire matrix is energy corrected by the relationship derived from Einstein's A and B coefficients and written in FORØ2Ø.DAT or FORØ21.DAT.

Because the linewidths are a function of the vibrational quantum number in these dimers, an additional step was added before the intensity *vs.* energy matrix was calculated. This step assumes that the linewidth has the functional form

width =  $a + cv^2$ . This change in linewidth can affect the shape of the overall band calculated from the Franck-Condon factors. In the case of  $\text{Rh}_2(\text{b})_4^{2+}$ , no broadening factor, CHAN, was used, resulting in the higher energy lines preserving the initial doublet structure. The absorption and phosphorescence spectrum of  $\text{Pt}_2(\text{H}_2\text{P}_2\text{O}_5)_4^{4-}$  have a significantly greater line-broadening progressing throughout the band. The inconsistencies between the calculated and observed bandshape for these two spectra is probably the result of an incorrect lineshape function. Several polynomial functions were tried having only two adjustable parameters; none of which could improve upon this simple quadratic form. If each linewidth was measured and applied toward the calculation, a better fit to the bandshapes could probably be obtained, but the addition of over a dozen more parameters in a calculation such as this seemed inappropriate.

The location of the maximum of the bands shifted only about one or two quanta upon changing the form of this linebroadening. This corresponds to a change in the distortion in  $\text{Pt}_2(\text{H}_2\text{P}_2\text{O}_5)_4^{4-}$  of only about  $.02 \text{ \AA}$ . This demonstrates that if the maximum of the Franck-Condon Overlaps occur as high as  $v = 8$  and the calculated maximum is within several quanta of the true maximum, the mass normalized distortion obtained will be close to the correct value.

```

100      FUNCTION FACT(P)
200      FACT=1.
300      K=NINT(P)
400      DO 10 I=2,K
500      FACT=FACT*I
600      10 CONTINUE
700      RETURN
800      END
900      SUBROUTINE HERM(A,P,C,K,Z1)
1000     IMPLICIT COMPLEX (C,Z)
1100     REAL Z1(C:24)
1200     DIMENSION C(C:24)
1300     REAL I1
1400     C=(A/(A+B))*SQRT(ABS(B*(A+B)/(A-B)))#D
1500     IF (A.LT.P) THEN
1600         Z=CMPLX(C.,C)
1700         ZDIFRT=CMPLX(C.,SQRT(ABS((A-B)/(A+B))))
1800     ELSE
1900         Z=CMPLX(C,0.)
2000         ZDIFRT=CMPLX(SQRT((A-B)/(A+B)),0.)
2100     END IF
2200     C(1)=(2.*Z#.707#ZDIFRT)**2
2300     CLAS=2.*Z
2400     CLAS2=CMPLX(1.,0.)
2500     Z1(C)=1.
2600     Z1(1)=REAL(C(1))
2700     QHERM=(0.,C.)
2800     DO 10, I=2,K
2900         I1=REAL(I)
3000         ZD=SQRT(1./((2.**I1)*FACT(I1)))
3100         ZF=ZDIFRT**I1
3200         ZC=ZD#ZF
3300         QHERM=2.*Z#CLAS-2.*(I1-1)#CLAS2
3400         C(I)=(QHERM#ZC)**2
3500         CLAS2=CLAS
3600         CLAS=QHERM
3700         Z1(I)=REAL(C(I))
3800     10 CONTINUE
3900     RETURN
4000     END

100      FUNCTION SHALO(A,P,E)
200      C=(P/2)/((E-A)**2+(P/2)**2)
300      SHALO=C
400      RETURN
500      END
600      FUNCTION GAUSS(A,P,E)
700      C=((E-A)/P)**2
800      IF (C.GT.5.) THEN
900          GAUSS=0.
1000         RETURN
1100     ELSE
1200         CONTINUE
1300     END IF
1400     GAUSS=EXP(-2.77259*C)
1500     RETURN
1600     END
1700     PROGRAM BANDS
1800     INTEGER PTPAND
1900     REAL IV
2000     DIMENSION IV(0:24),FMV(0:24),ABSNU(0:24),FMNU(0:24)
2100     DIMENSION ABAPRT(POC),FMAPRT(BCO)

```

```

2200 READ(10,200) DELTC,RURS,REMP,HWGR,HWEY,HW2,OCNU,SCALE,
2300 1RUR2,REMP2,SPACE,CHIAP,CHIEM,CHAN,NUMV,IFLAG
2400 NUMPT=NINT(NUMV*HWEY/SPACE)
2500 IF (IFLAG.EC.2) GO TO 110
2600 ARSNU(0)=OCNU
2700 ARS=ARSNU(0)
2800 DO 5 I=1,NUMV-1
2900 ARSNU(I)=ARS+HWEY-CHIAR*(I-1)
3000 ARS=ARSNU(I)
3100 5 CONTINUE
3200 CALL HERM (HWGR, HWEY, DELTC, NUMV, IV)
3300 WRITE(40,210)IV
3400 DO 100 I=1,NUMPT
3500 APPARI(I)=C.
3600 E=OCNU-150.+(I-1)*SPACE)
3700 DO 90 J=C, NUMV-1
3800 RARS=RURS+(REAL(J)**2*CHAN)
3900 RAP2=RUR2+(REAL(J)**2*CHAN)
4000 APPARI(I)=IV(J)*SHALO(ARSNU(J),RARS,E)+APPARI(I)
4100 APPARI(I)=IV(J)*SCALE*SHALO(ARSNU(J)+HW2,RAP2,E)+APPARI(I)
4200 90 CONTINUE
4300 APPARI(I)=APPARI(I)*E/OCNU
4400 100 CONTINUE
4500 WRITE(20,210)APPARI,SPACE
4600 110 IF (IFLAG.EC.1) GO TO 400
4700 EMNU(0)=OCNU
4800 EM=EMNU(0)
4900 DO 130 I=1,NUMV-1
5000 EMNU(I)=EM-HWGR+CHIEM*(I-1)
5100 EM=EMNU(I)
5200 130 CONTINUE
5300 CALL HERM (HWEY,HWGR,DELTG,NUMV,EMV)
5400 DO 150 I=1,NUMPT
5500 EMPARI(I)=C.
5600 E=OCNU+150.-(I-1)*SPACE)
5700 DO 140 J=0,NUMV-1
5800 REM=REMP+(REAL(J)**2*CHAN)
5900 REP2=REMP2+(REAL(J)**2*CHAN)
6000 EMPARI(I)=EMV(J)*SHALO(EMNU(J),REM,E)+EMPARI(I)
6100 EMPARI(I)=EMV(J)*SCALE*SHALO(EMNU(J)-HW2,REP2,E)+EMPARI(I)
6200 140 CONTINUE
6300 EMPARI(I)=EMPARI(I)*(E/OCNU)**4
6400 150 CONTINUE
6500 WRITE(21,210)EMPARI,SPACE
6600 200 FORMAT(14(F10.4/),2(I3/))
6700 210 FORMAT(1X,5F10.4)
6800 400 END

```